SOLUTION PROCESSING VIA BLENDING APPROACHES TO CONTROL SELF-ASSEMBLY OF CONJUGATED POLYMERS

A Dissertation
Presented to
The Academic Faculty

by

Michael Anthony McBride

In Partial Fulfillment
of the Requirements for the Degree
Doctor of Philosophy in the
School of Chemical and Biomolecular Engineering

Georgia Institute of Technology
May 2019

SOLUTION PROCESSING VIA BLENDING APPROACHES TO CONTROL SELF-ASSEMBLY OF CONJUGATED POLYMERS

Approved by:

Dr. Martha Grover, Advisor
School of Chemical and Biomolecular Engineering
Georgia Institute of Technology

Dr. David Collard
School of Chemistry
Georgia Institute of Technology

Dr. Elsa Reichmanis, Advisor
School of Chemical and Biomolecular Engineering
Georgia Institute of Technology

Dr. Carson Meredith
School of Chemical and Biomolecular Engineering
Georgia Institute of Technology

Dr. Michael Filler
School of Chemical and Biomolecular Engineering
Georgia Institute of Technology

Date Approved: March 11th, 2019

To my family near and far,

this journey would not have been possible

without your unwavering love, support, and guidance.

ACKNOWLEDGEMENTS

Completion of my PhD would not be possible without the constant encouragement and support of my co-advisors Professor Martha Grover and Professor Elsa Reichmanis. My journey started with fresh excitement to solve the world's greatest problems that end with me chasing my tail in a million different circles. I extend my deepest gratitude for your trust in me to explore the unknown and your gentle nudges to push me back when I swayed too far.

To Nils Persson, thank you a million times over. From thought provoking discussions on the future of neuromorphic computing to endless hours mining literature for process-structure-properties relationship, I have learnt so much under watch. A thank you to the one individual that has helped shaped my thought process on research the most.

To my officemates Xun Tang, Ping-Hsun Chu, Bailey Risteen, Audrey Scholtz, and Brian Khau thank you for the laughs on the rough days and the constant support on the good days. The PhD experience would not have been the same without you.

To all the members of the Grover and Reichmanis group, thank you for always expanding my knowledge on protein self-assembly, ampicillin processing, polymer synthesis, battery electrodes, cellulose, and hydrophobins. Thank you for the support, comments, feedback, and suggestions along this journey.

To Danny, Guillermo, Carlex, and Aarti, the A team. Thank you for the countless hours in the glovebox characterizing devices and AFM room hoping for defect-free images. I am deeply touched by the dedication and help you all provided.

To my committee, Dr. Filler, Dr. Collard, and Dr. Meredith, thank you for the advice as this project has transformed from a figment of imagination to actual results.

Most importantly, to my family, thank you. Thank you to my parents and siblings for guiding me in life to this point and thank you in advance for guiding me in the future. To my amazing wife Rebecca McBride, thank you for trusting me that during my graduate studies that I would be the same man at the end of the day as I was at the beginning. Thank you for keeping our lives chugging along when I was distracted with late night experiments and thank you for listening to my rambles on P3HT. Rebecca, thank you for sharing your wonderful family with me and thank you to them for all their support. This journey would not have been possible without all the words of advice and encouragement of all family, near and far. Thank you.

TABLE OF CONTENTS

LIST OF TABLES

LIST OF FIGURES

LIST OF SYMBOLS AND ABBREVIATIONS

a	Distance between molecules
C_{ox}	Capacitance of the gate dielectric material
D	Einstein diffusion coefficient
d	Number of points in the box
D	Total observations in the database
e	Electron charge
F	Electric field
Fr	Fraction of data in reduced space
$HOMO$	Highest occupied molecular orbital
I_D	Drain current
k	Growth rate constant
k_B	Boltzmann constant
k_{ET}	Electron hopping rate
L	Channel length
l	Span of variable i that contains "high" points
L	Span of variable i that contains all points
$LCAO$	Linear Combinations of Atomic Orbitals
$LUMO$	Lowest unoccupied molecular orbital
MW	Molecular weight
n	Avrami exponent
N_f	Density of states
$OFET$	Organic field-effect transistor

$\boldsymbol{OLED}$	Organic light emitting diode
$\boldsymbol{OPV}$	Organic photovoltaic
$\boldsymbol{P3HT}$	Poly(3-hexylthiophene)
$\boldsymbol{RFID}$	Radio frequency identification
$\boldsymbol{R_{ij}}$	Spatial distance between occupied site, i, and unoccupied site, j
$\boldsymbol{rs}$	Reduced space
$\boldsymbol{S_{full}}$	Degree of orientational order
$\boldsymbol{T}$	Temperature
$\boldsymbol{t_{trans}}$	Transfer integral
$\boldsymbol{v}$	Velocity of a charge carrier
$\boldsymbol{V_D}$	Drain-source bias
$\boldsymbol{V_G}$	Gate voltage
$\boldsymbol{V_G}$	Gate bias
$\boldsymbol{v_o}$	Attempt-to-jump frequency
$\boldsymbol{VRH}$	Variable range hopping model
$\boldsymbol{V_T}$	Threshold voltage
$\boldsymbol{W}$	Channel width
$\boldsymbol{W}$	Exciton bandwidth
$\boldsymbol{\alpha^{-1}}$	Effective overlap parameter
$\boldsymbol{\alpha_D}$	Size of the localized state
$\boldsymbol{\Delta E}$	Energy difference between states
$\boldsymbol{\lambda_{reorg}}$	Reorganization energy
$\boldsymbol{\mu}$	Charge mobility
$\boldsymbol{\rho_{FL}}$	Fiber length density
$\boldsymbol{\hbar}$	Planck's constant

θ Crystallinity, aggregate fraction

SUMMARY

Thematically, this work focuses on developing solution blending processes that result in the formation of interconnected polymer networks for enhanced electronic properties. Robust and industrially relevant solution processing methods that precisely control the self-assembly process are essential to achieve optimal and repeatable electronic device performance in semi-crystalline conjugated polymers. This research follows a bottom-up approach to develop process-structure-property relationships using the "fruit fly" of conjugated polymers, poly(3-hexylthiophene) (P3HT).

Herein, we demonstrate facile solution processing methods that focus on blending multiple components to target the formation of interconnected assemblies. P3HT is the canonical semicrystalline conjugated polymer, and here was used to investigate the mechanism of self-assembly in solution. The polymer molecular weight distribution, solute-solvent interactions, and quantity of seed nuclei are shown to be tunable parameters impacting the degree of interconnectivity. These approaches were investigated using a wide array of strategies to induce nucleation, including exposure to low dose UV, microfluidic flow processing, and poor solvent addition. A particularly promising approach involves the selective mixing of a nucleated polymer solution with a non-nucleated sample via seed nucleation. These processing approaches have improved the charge carrier mobility from a base of ~10^{-3} cm^2/V-s to values exceeding $2x10^{-1}$ cm^2/V-s. Process-structure-property relationships were developed to quantitatively describe the tradeoffs between polymer network formation and grain boundaries on charge transport. All

examined cases suggest an optimal processing window for long range interconnectivity, in which a moderate level of crystallinity is associated with the highest mobility.

Finally, materials informatics approaches were leveraged to develop process-property relationships to help guide the next level of experimental efforts. A database of 218 data points from 19 publications on P3HT was created with mobility values ranging from 1.0×10^{-6} to 2.8×10^{-1} $cm^2/V\text{-}s$. A classification technique in which devices were sorted into high performing and low performing was applied. A reduced design space containing all high performing points, as well as some having poor performance, is identified for the purpose of focusing future experiments.

CHAPTER 1. INTRODUCTION

1.1 Conjugated Semiconducting Polymer Electronics

1.1.1 History and Background

Organic polymeric electronics can trace its origins back to the research of Alan J. Heeger, Alan MacDiarmid, and Hideki Shirakawa in 1977 when they discovered the ability of polymers to conduct electricity.[1] Their Nobel Prize winning work demonstrated that polyacetylene, when doped via oxidation with chlorine, bromide, or iodine vapor, exhibited a 10^9 increase in electronic conductivity compared to its undoped counterpart. The presence of conjugated double bonds, or alternating single and double bonds, along the polymer backbone enables delocalization of electrons from the weak π bond.[2] Upon injection of a charge carrier (doping), either an electron or a hole, with the presence of an electric field, charges can hop along the backbone enabling unique optical and electronic properties.[3-4]

Traditionally, inorganic electronics have dominated the electronics industry. Their ability to form near-perfect crystals in thin films leading to uninterrupted electrical pathways combined with the ease of doping to increase the concentration of charge carriers results in enhanced conductivity and semiconducting properties. In contrast, molecular doping in conjugated polymers results in morphological changes along the chain backbone, increasing grain boundaries and charge traps that suppress electronic properties.[5-6] Despite reduced electrical properties, polymeric electronics promises a new array of technologies that leverage the stretchability, flexibility, biocompatibility and tunability of polymers. Moreover, inclusion of solubilizing side chains to polymer conjugated backbones enables

solution processability allowing for low-cost, roll-to-roll printing of large area devices[3]. As many applications based require flexible, non-rigid form factors, and less computational power than their inorganic counterparts on organic electronics are currently in the research and development phases (**Figure 1**). These include organic field-effect transistors (OFETs),[7-8] organic photovoltaics (OPVs),[9-10] organic light emitting diodes (OLEDs),[11-12] and radio frequency identification (RFID)[13-14] tags with use as sensors,[15] electronic skins,[16] and wearable devices.[17]

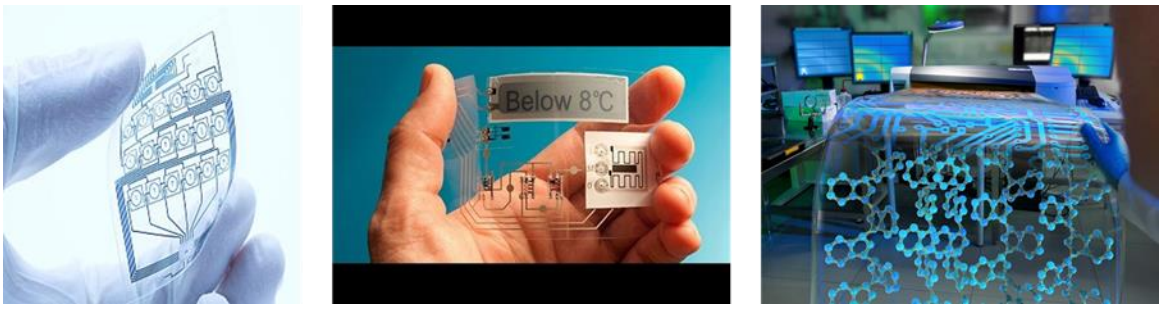

Figure 1: Flexible roll-to-roll processed organic electronics. Images adapted from Ars Technica, Flexible Packaging Magazine, and the Technical University Munich.

Despite the recent advances in solution processed organic electronics, their inclusion in marketable devices is limited by device performance. Charge mobility, an important property that describes the velocity of electrons given an applied electric field, has steadily progressed towards ~1 cm^2/V-s with a target of ~10 cm^2/V-s for advanced applications in solution processed polymeric electronic devices **(Figure 2)**.[18] Compared to mobility values exceeding 100 cm^2/V-s observed for inorganic electronics, significant progress is still required to develop commercially available organic electronic devices.[19]

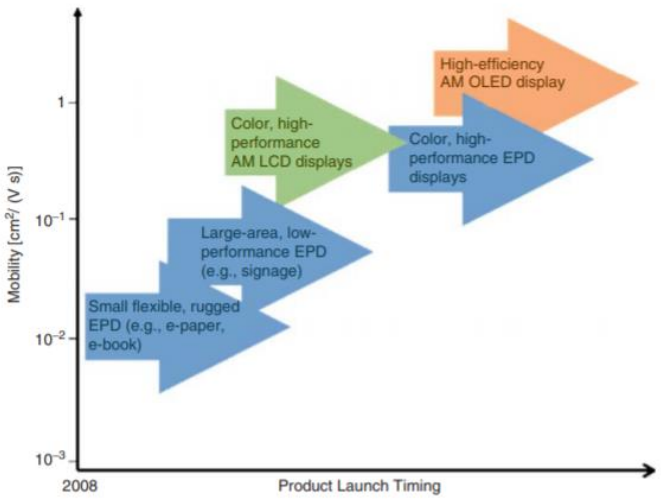

Figure 2: Required charge carrier mobility values to enable expected organic electronic technologies. Adapted with permission from Ref. 18. Copyright Materials Research Society 2008.

1.1.2 Electrical Properties of Conjugated Polymers: From Bonds to Bands

Polyalkenes represent one of the simplest and most common polymer families. Formed from the addition reaction of alkenes, the polyalkenes are saturated, long chain hydrocarbons that are chemically inert. Like most other commercially available polymers, they are insulators due to their chemical structure. Each carbon atom in the polyalkenes is sp^3 hybridized and directly bonded to four adjacent atoms via sigma (σ) bonds. In sigma bonds, the electron density is strongly concentrated between two neighbouring nuclei. When an electric field is applied, the stability of the bond does not allow movement of electrons, resulting in insulating properties. In contrast, polyacetylene is the simplest conjugated polymer, with alternating single and double bonds. Carbon-carbon bonds along the backbone are sp^2 hybridized, forming both σ and π bonds. The electron density of π bonds is concentrated above and below the plane of the nucleus, enabling delocalization along the polymer chain backbone.

The Huckel molecular orbital theory has provided a simple approximation to determine the bond energies of molecular orbitals of π-electrons via Linear Combinations of Atomic Orbitals (LCAO). The constructive and deconstructive mixing of atomic orbitals results in an energy difference between the bonding (π) and antibonding (π*) molecular orbitals. As the length of conjugation increases, the polymers can be considered as repeated sub-units, enabling positive and negative combinations of π and π* levels to form new accessible energy levels. As the conjugation length tends towards infinite length, these energy levels can be viewed in terms of band theory with the π energy levels forming the highest occupied molecular orbital (HOMO, valence band) and the π* forming the lowest unoccupied molecular orbital (LUMO, conductive band)**(Figure 3**).

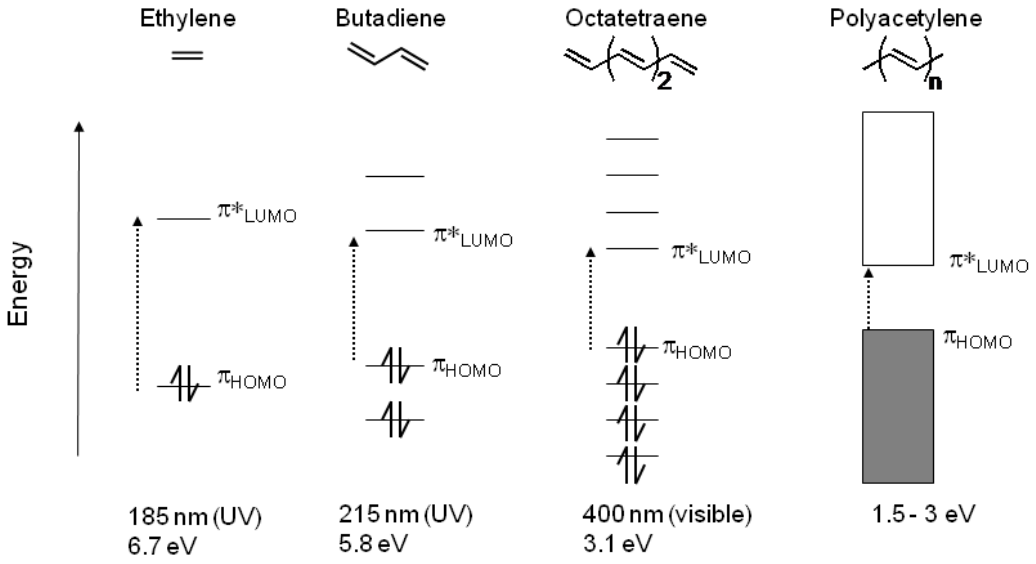

Figure 3: Progression of the HOMO and LUMO energy levels as a function of conjugation length in the polyene series. Image adopted form the Clean Energy Wiki.

The difference in energy levels forms the band gap and governs the electrical properties of the material. Electrons must possess enough energy to move from the valance

band to the conduction band to enable the flow of electricity. In conductors, the valence and conduction bands overlap so no additional thermal energy is required to simulate electron mobility. Semiconductors possess a small bandgap, so energy is required to promote electrons from the valence band to the conduction band. OFETs, OLEDs, and OPVs all rely on precise tuning of the band gap to enable their most basic functionality. In OLEDs, the colour of emitted light is determined by the bandgap of the material and *vice versa* in OPV applications.

The field-effect transistor operates as an electric switch and amplifier of electronic signals. This is achieved via variations in the applied voltages through the three electrical connections (**Figure 4**). A gate electrode is separated from the active layer by an insulating dielectric layer. Varying the voltage to the gate alters the conductivity of the active layer between the source and drain electrodes. An applied voltage difference between the source and drain electrodes then enables the flow of electrons or holes through the device. The properties of interest, charge mobility and threshold voltage, can be extracted from the relationship between the drain current, I_D, and the applied gate voltage, V_G.[20] In the saturation regime of operation, this relationship is modelled by the following equation:

$$I_D = \frac{WC_{ox}}{2L}\mu(V_G - V_T)^2 \quad (1)$$

where W and L are the channel width and length of the transistor channel, C_{ox} is the capacitance of the gate dielectric material, μ is the charge mobility, and V_T is the threshold voltage. Both μ and V_T are fitted parameters but can be extracted from the slope and intercept by linearizing **Equation 1** above, as shown in **Figure 4b**.

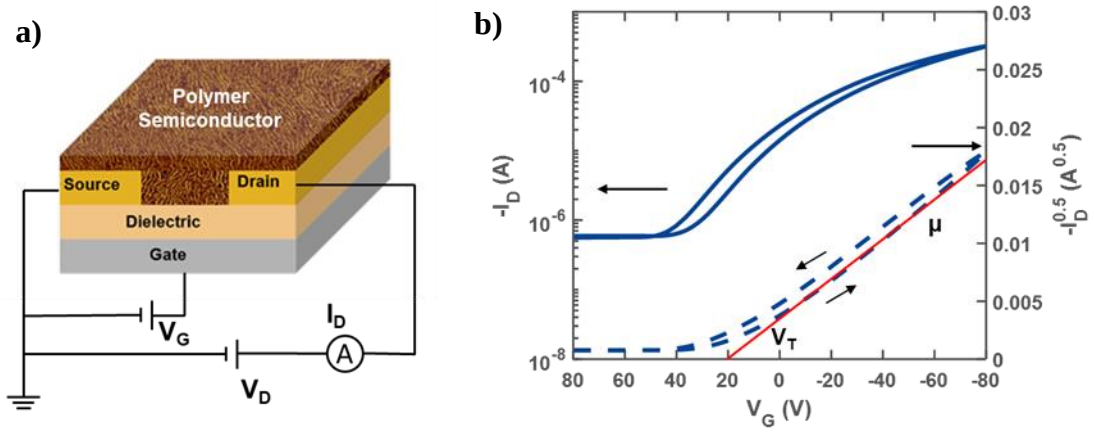

Figure 4: a) Schematic of a general bottom-gate, bottom-contact OFET, b) Typical OFET transfer curve from the saturation regime depicting extraction of μ and V_T.

The operating principles of OFETs can be illustrated using simplified electronic energy level diagrams as shown in **Figure 5**.[21] When the gate bias to the device is zero (V_G=0), the device is at equilibrium with the active layer HOMO residing below the Fermi level of the source and drain electrode and the LUMO residing above. A drain-source bias (V_D) would not result in conduction as the semiconductor lacks mobile charge carriers. However, when a gate bias is applied an electric field is generated at the active layer/insulator interface. For a n-type semiconductor, which is more efficient at moving electrons than holes, application of a positive gate voltage (V_G>0) lowers the HOMO and LUMO energy levels. If the bias is sufficiently large enough, the LUMO will become resonant with the Fermi level of the source/drain electrodes, proving mobile electrons at the semiconductor/insulator. Application of a positive drain-source base (V_{DS}>0) provides a driving force for electrons to flow through the semiconducting layer between the contacts. A similar but opposite process occurs for a p-type semiconductor in which a negative gate bias (V_G>0) causes the energy levels of the semiconductor to shift up, forming mobile charge carrier (holes) at the interface.

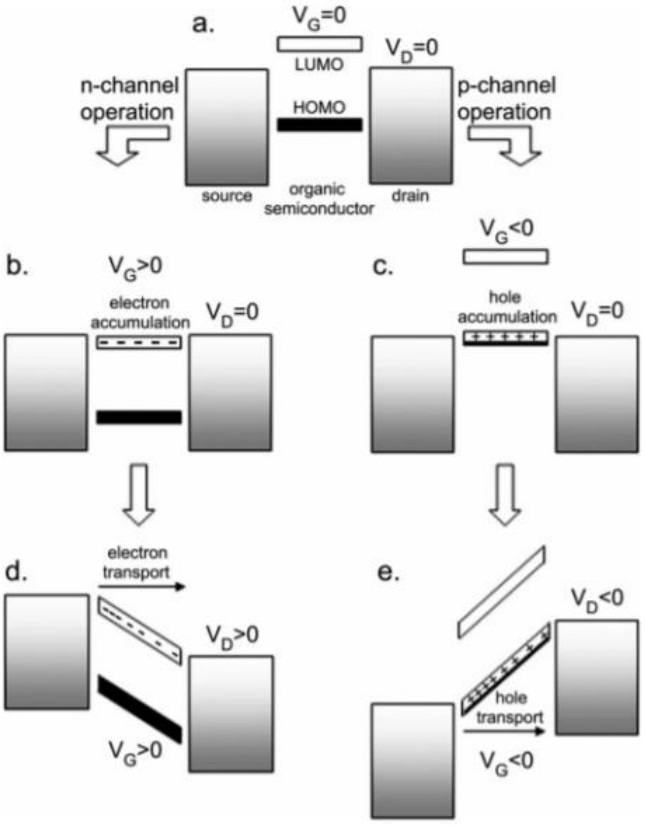

Figure 5: Ideal energy diagram of n-channel and p-channel OFET transistor during operation. a) At V_G=0 and V_D=0, the semiconductor HOMO is below the Fermi level of the source and drain. b-c) An applied V_G shifts the HOMO/LUMO levels of the semiconductor providing a pathway for holes/electrons. d-e) An applied V_D allows holes/electrons to flow through the device. Adapted with permission from Ref. 21. Copyright American Chemical Society 2004.

1.1.3 Charge Transport Models in Disordered Orgnic Electronic Systems

The primary use of a field-effect transistor as a research tool is to characterize the charge mobility of the active material.[22] Charge mobility, μ, is defined as the rate of movement of a charge carrier, v, given an applied electric field, F, as shown in **Equation 2**.

$$\mu = \frac{v}{F} \tag{2}$$

Alternatively, charge mobility can be expressed in terms of the Einstein-Smoluchowski equation (**Equation 3**):

$$\mu = \frac{eD}{k_B T} \tag{3}$$

where e is the electron charge, D is the diffusion coefficient, k_B is the Boltzmann constant and T is the temperature. In either formulation, supporting equations must be applied to describe the movement of charges at the atomic level.[23]

Understanding the fundamental mechanism of charge transport in organic semiconductors can aid identification of optimal morphologies. The well-defined crystalline lattice formed in inorganic molecules allows charge carriers to be delocalized across the entire system, enabling so-called band transport. In contrast, organic molecules are subjected to the polarization effect resulting in Columbic interactions between electron and hole pairs.[24] This results in a localization of the charges. As a result, charge transport in organic systems generally exhibit charge hopping between neighbouring molecules via polaron formation.[25-26]

Rudolph Marcus formulated this theory of charge transport by describing electron transfer from a molecule in the charged state to a molecule in the neutral state.[27] When the charge is transferred from one molecule to the other, both must reorganize to optimize their geometry to account for the presence or absence of the charged electron. This process is termed intramolecular relaxation. The charge transport process also results in intermolecular relaxation as the electron density, and thus size of the molecules, has changed. This causes a reorganization of the spatial location of molecules that can interrupt

charge transport through the introduction of vibrational movement. The electron hopping rate (k_{ET}) describing these processes can be expressed as:

$$k_{ET} = \frac{2\pi}{\hbar}\frac{t^2}{\sqrt{4\pi\lambda_{reorg}k_BT}}\exp\left[-\frac{\left(\lambda_{reorg}+\Delta E\right)^2}{4\lambda_{reorg}k_BT}\right] \quad (4)$$

where *t* is the transfer integral, ħ is Planck's constant, k_B is the Boltzmann constant, T is the temperature, ΔE is the energy difference between the charged and neutral state, and λ_{reorg} is the reorganization energy. A one-dimensional (1D) diffusion coefficient that can relate the electron hopping rate to charge mobility can be expressed as:

$$D = a^2 k_{ET} \quad (5)$$

where *a* is the distance between molecules. An expression for charge carrier mobility can be obtained by combining **Equations 3**, **4** and **5**:

$$\mu = \frac{ea^2}{k_BT}\frac{2\pi}{\hbar}\frac{t^2}{\sqrt{4\pi\lambda_{reorg}k_BT}}\exp\left[-\frac{\left(\lambda_{reorg}+\Delta E\right)^2}{4\lambda_{reorg}k_BT}\right] \quad (6)$$

Charge mobility can be maximized by maximizing the transfer integral and minimizing the reorganization energy of the system.[27-28] However, this transport model assumes a highly disordered system and does not capture the role of aggregation on extending charge transport pathways.

To account for the semicrystalline nature of many semiconducting polymer morphologies, a variety of transport models have been developed based on

phenomenological observations that capture the role of chemical and physical defects (**Figure 6**). Many of these models have been developed based on the seminal work by Miller and Abrahams[4] that suggested that the hopping rate depends on the spatial distance, R_{ij}, between sites (occupied site i and unoccupied site, j), and the energetic difference between the two sites, $\Delta E=E_i-E_j$. Their proposed hopping rate can be expressed as:

$$W_{ij} = v_o \exp(-2\alpha R_{ij}) \begin{cases} \exp\left(-\frac{\Delta E}{k_B T}\right) & if\ \Delta E > 0 \\ 1 & if\ \Delta E \leq 0 \end{cases} \quad (7)$$

where v_o is the attempt-to-jump frequency and α^{-1} is the effective overlap parameter. The addition of thermal energy is only required if the destination site is of higher energy.

The variable range hopping (VRH) model developed by Sir Nevill Mott has been used to describe charge transport when the semiconductor is highly disordered in both energy (contains traps from a non-uniform density of states) and spatial locations (not periodically spaced.[4] They considered the case in which it may be more energetically favourable to hop over a longer distance with a lower energy difference between sites compared to a shorter hop with a higher energy difference. The simplest formulation of the VRH model can be expressed as:

$$\mu \propto \exp\left[-\frac{9k_B N_f}{128\pi\alpha^3 T}\right]^{\frac{1}{4}} \quad (8)$$

where N_f is the density of states at the Fermi Edge and α is the size of the localized state.

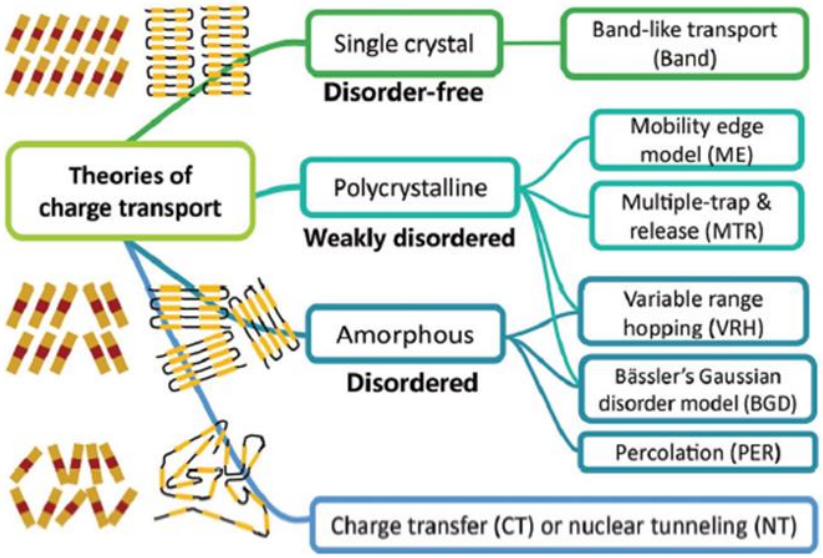

Figure 6: General charge transport theories as a function of disorder. Adapted with permission from Ref. 29. Copyright Royal Society of Chemistry 2017.

Despite the different assumptions of each model, there are several commonalities that can guide structure-property relationships. All models exhibit enhanced hopping rates with decreased distance between states. This is described by the transfer integral, t, in Marcus Theory and the spatial distance, R_{ij}, in Miller and Abraham's model and the VRH model. Furthermore, all models indicate improved transport properties with improved conjugation length, captured by the reorganization energy in Marcus Theory and the size of the localized state in the spatial hopping models. Therefore, it has been suggested that the ideal morphological structure contains numerous large crystalline domains with enhanced molecular packing to reduce the spatial distance between lower energy states.[29] More broadly speaking, control of both intra- and intermolecular structure is essential to obtaining robust and reliable charge transport properties.

1.1.4 Poly(3-hexylthiophene): A work-horse polymer

Polythiophenes have received a remarkable degree of attention as semiconducting polymers since their first use in the late 1980's.[30-31] The ease of synthesis of polythiophenes compared to new, more complex polymeric structures has turned these polymers into a key workhorse system to study fundamental process-structure-property relationships. As a new paradigm in electronics device manufacturing develops to enable low cost, large area, flexible electronic devices, the ideal conjugated polymer must be either solution or melt processable to enable printed roll-to-roll processing.[3] As polythiophenes are known to thermally degrade when exposed to high temperatures, the solution processability route is often leveraged to deposit polythiophene based thin films. Thus, polymer solubility plays an important role in the ink formulation process. While polythiophene itself is insoluble, the addition of long, flexible hydrocarbon chains enhances the solubility and thus processability of this class of conjugated polymers.[32-33]

A wide variety of side chain motifs have been suggested to improve the solubility of thiophene, from bulky branched chains to leverage liquid crystal properties to carboxylic salts for improved solubility in water.[34-35] The addition of side chains adds steric hindrance along the chain backbone leading to changes in the conjugated backbone flexibility, increases in the π-π stacking distance and modifications to the orbital overlap.[36] These properties can be optimized by ensuring planarization of thiophene chains and therefore long-range delocalization of electrons. However, the relative position of the side chain on adjacent thiophene monomers has a profound impact on the favorable configurations. Both head-to-head (HH) and tail-to-tail (TT) coupling adds additional steric interactions and disrupts the planarization of the backbone.[37-38] Instead, a high degree of head-to-tail

couplings (HT), described by the regioregularity of the polymer is desired for chain planarization and improved electron delocalization. Moreover, a planar structure of thiophene ring faces can be formed with individual monomers adopting either the trans or cis configuration.[39] In the context of the planarization of poly(3-alkylthiophene) (P3AT) chains, the desired structure is a polymer chain with all monomers in the trans configuration.

At a synthetic level, significant progress has been made to control the regiochemistry and yield during synthesis of P3ATs. This has enabled widespread commercial availability of P3ATs allowing for detailed physical characterization of both solutions and films. Coincidently, poly(3-hexylthiophene) (P3HT) has arisen, not just as a model polythiophene polymer, but as the 'fruit fly' of conjugated polymers. The chemical structure of this polymer is shown in **Figure 7a**. The vast amount of accumulated knowledge on the P3HT provides an unparalleled opportunity to elucidate informative process-structure-property relationships relevant to the behavior of conjugated polymers in general. Process-structure-property relationships have been thoroughly examined and reviewed on multiple occasions[40-43] and continue to develop. Already, a remarkably diverse array of structures has been identified from the solution processing of P3HT in solution. Examples of unique structural motifs include single crystals,[44] nanowhiskers,[45] isotropically aligned nanofibers,[46] shish-kebab fibers,[47] and interconnected fibral domains.[48-49] The latter three structures have received a significant amount of attention due to their ability to form the long-range charge transport properties required of solution processing for large area devices.

In P3HT, the delocalization of π-electrons leads to the formation of co-facially stacked chains held together via physical π-π bonds **(Figure 7b)**. This phenomenon gives rise both to nanofibril-like structures and/or interconnected fibril networks depending on the degree of overlap between neighboring chains as shown in **Figure 7c and d**. Regardless of the structure, the π-π stacking distance between cofacially aligned chains is ca. 0.38 nm. The length of fibrils formed from π-π stacking of a few chains to thousands of chains can grow to several microns in length. Chains can also stack edge-to-edge in the alkyl direction, generally at a stacking distance of 1.6 nm. As the hexyl side chains are insulating, the development of structure in this stacking distance is irrelevant to charge transport. Instead transport along the conjugated backbone and through π-stacks govern the bulk electrical properties of the films. Charge transport along the conjugated backbone, termed intramolecular charge transport (~1 cm^2/V-s), has been both theoretically and experimentally shown to be faster than intermolecular charge transport (~10^{-2} cm^2/V-s) through π-stacks.[50-51] The differences in obtained charge mobilities are largely governed by the differing modes of transport in the material, as described in the electron transport theories presented in **Section 1.1.3**.

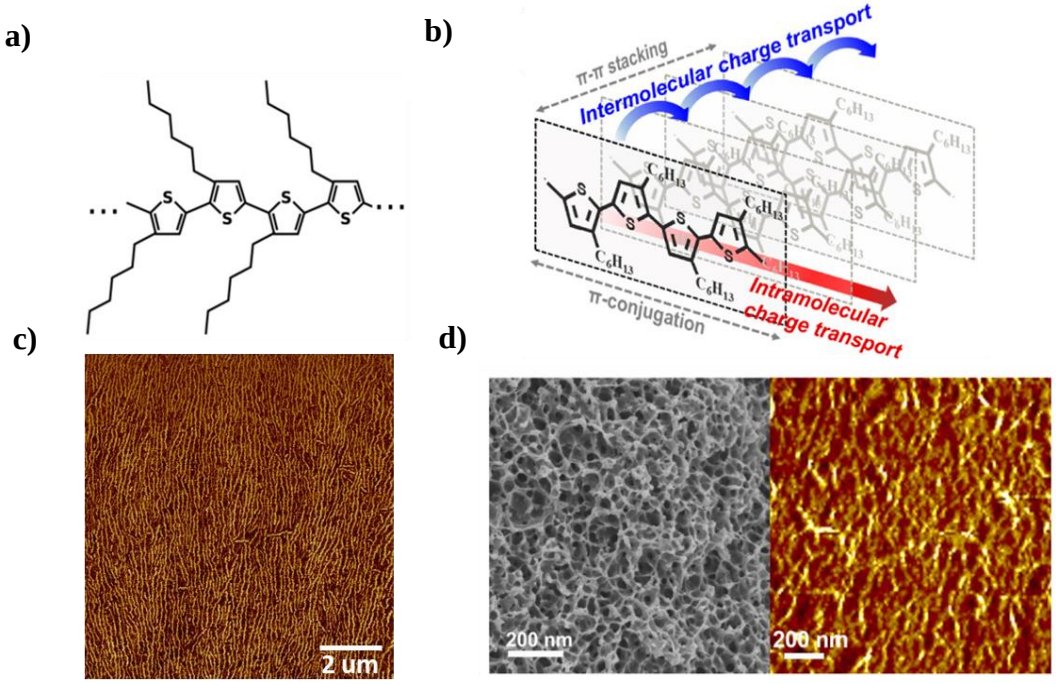

Figure 7: a) Chemical structure of P3HT. b) illustration of π-π stacking of P3HT into lamellar stacks. Adapted with permission form Ref. 50. Copyright American Chemical Society 2016. c) AFM image of aggregated nanofibers deposited via blade coating. d) TEM (left) and AFM (right) of interconnected P3HT network. Adapted with permission from Ref. 49. Copyright American Chemical Society 2017.

As a result, the development of processing methods to preferentially manipulate and control the alignment and ordering of conjugated polymer thin films has been a key focus area in the field (**Figure 7c and d**). Early investigations relating charge transport properties to polymer molecular weight, polydispersity, solvent choice and processing history has greatly advanced the community's understanding of solution processable organic electronics. One of the earliest proposed process-structure-property relationships was the influence of the molecular weight based on work by Zhang *et al.*[52] and Kline *et al.*[53] An increase in charge mobility was observed with an increase in the molecular weight from 10^{-4} cm^2/V-s using a Mn of 3 kDa to 10^{-2} cm^2/V-s with a Mn of 30 kDa. Notably, a decrease in the observed ordering of P3HT chains was observed using AFM as shown in

Figure 8. It was theorized that charge transport is enhanced in higher molecular weight polymer systems, as longer chains can form more inter-grain connections, enabling percolative charge transport pathways. Since then, a variety of processing methods to control the formation of tie chains that connect crystalline domains have been proposed.

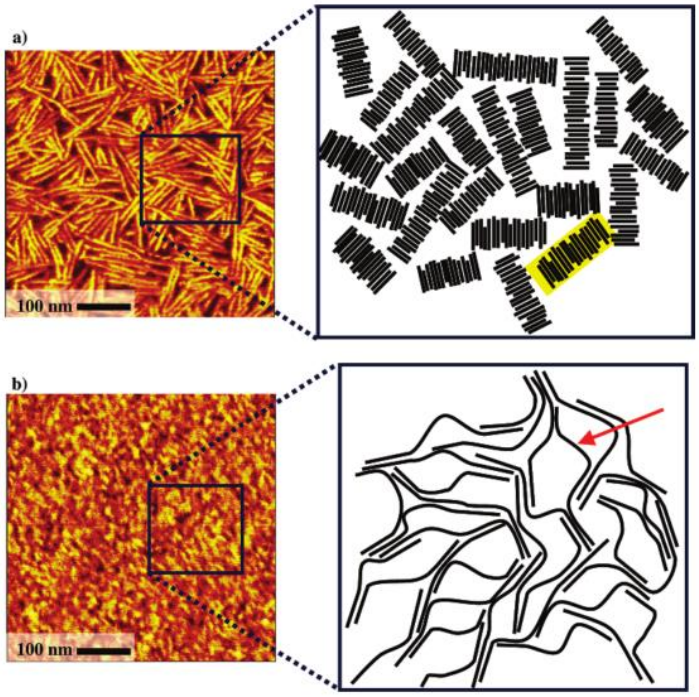

Figure 8: Observed structure of P3HT thin films fabricated for 3 kDa (top) and 30 kDa (bottom) P3HT. Adapted with permission from Ref. 52. Copyright American Chemical Society 2005.

1.2 Processing of Polymer Electronics

In polymer electronic devices, macroscopic charge transport properties are governed by the assortment of interconnected pathways between highly conductive crystalline domains and less conductive amorphous regions. Precise control of the crystallization process to manipulate the distribution of crystalline states and morphologies in the solid state remains crucial to increasing charge mobility. A myriad of studies has revealed microstructural features that influence charge transport including i) electron

delocalization arising from ordered crystalline domains, ii) the formation of percolative charge transport pathways between crystalline domains, and iii) alignment of the crystallographic direction relative to the active channel.

Processing strategies to control the morphology can be separated into three main categories: 1) solution-state preprocessing 2) controlled deposition methods, and 3) solid state post processing. Solution state preprocessing involves disrupting the local solvent environment to planarize polymer chains or induce nucleation and growth of crystalline domains.[54-55] Controlled deposition methods involve manipulation of shear-aligning techniques and solvent evaporation rates to obtain ordered microstructures.[50, 56] Solid-state post processing involves thermal annealing or mechanical manipulation techniques.[57] Solution state preprocessing methods have received significant attention due to their industrial applicability.

A wide range of processing methods have been proposed to promote self-assembly of nanofibers. These techniques include solvent solubility tuning,[46, 58-61] ultrasonication (Son),[54, 62-64] UV irradiation,[65-68] solution aging, [50, 69] and microfluidics,[55] each with their own unique proposed mechanism of self-assembly and accessible nanofibril structures. Stark contrasts in the fibril morphology can be easily visualized using AFM images analyzed *via* advanced image processing techniques. Persson *et al.* compiled 100 AFM images from 9 unique solution preprocessing techniques produced in the same laboratory setting.[70] These images were analyzed using open source software to quantify the fiber length density (ρ_{FL}), degree of orientational order (S_{full}), and mean fiber length.

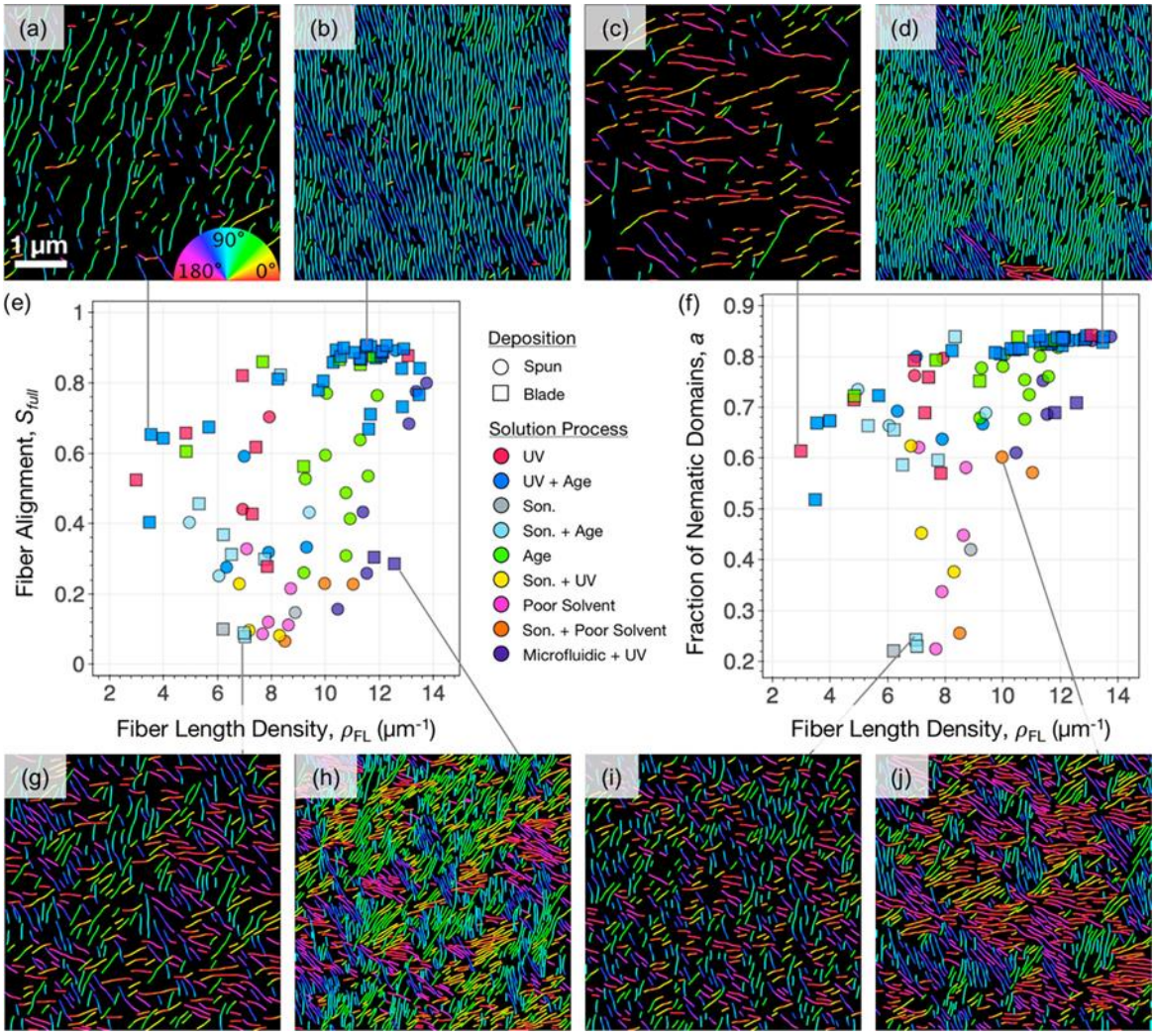

Figure 9: A vast array of structural motifs can be obtained through solution processing of P3HT solutions. The degree of alignment and fiber length density are two structural metrics that can help elucidate the process-dependent mechanism of self-assembly. Adapted with permission from Ref. 70. Copyright American Chemical Society 2017.

Similar processing methods appear to cluster around unique values of the structural descriptors as illustrated in **Figure 9.** Son + poor solvent thin films display a medium packing density and low alignment with minimal tunability as a function of processing. In comparison, Son + Age thin films exhibit both a medium degree of alignment and packing density. Microfluidic + UV processed fibers generally display a high fiber length density, with the degree of processing controlling the fiber alignment.

Analysis conducted in this manner can be used to support hypothesized self-assembly mechanisms. Persson *et al.* analyzed the alignment and packing density results of the three mentioned techniques and summarized differing bundle formations elucidated in the original publications.[70] In the case of poor co-solvent addition with sonication, the presence of the unfavorable solvent environment and cavitation from sonication will induce nucleation of P3HT nanofibers. However, the presence of the poor cosolvent results in few tie chains between fibers as the fringe chains coil up to decrease their interaction with the solvent. Upon thin film deposition, each fiber will be exposed to a unique shear force leading to an isotropic film. In the case of sonication and aging, the cavitation effect will once again provide the nucleation step. The aging time allows fibers to diffuse through the solution and for tie chains to extend and form interconnections. These interconnections keep the network together during deposition leading to enhanced local alignment. An extreme case of tie chain interconnectivity is hypothesized to arise from microfluidic processing *via* the formation of shish-kebabs. In terms of charge carrier mobility, $\mu_{microfluidic} > \mu_{Son+Age} > \mu_{Son+Poor\ Solvent}$, indicating the importance of tie chains for enhanced global charge transport. Expanding this analysis for a more inclusive array of solution preprocessing techniques shows a general correlation between S_{full} and charge carrier mobility. This has been attributed to tie chains that lead to a network, which further enables orientational alignment during deposition and a percolative pathway for enhanced charge transport. **Figure 10** depicts hypothesized structural motifs that fringe chains at the end of fibers can exhibit.

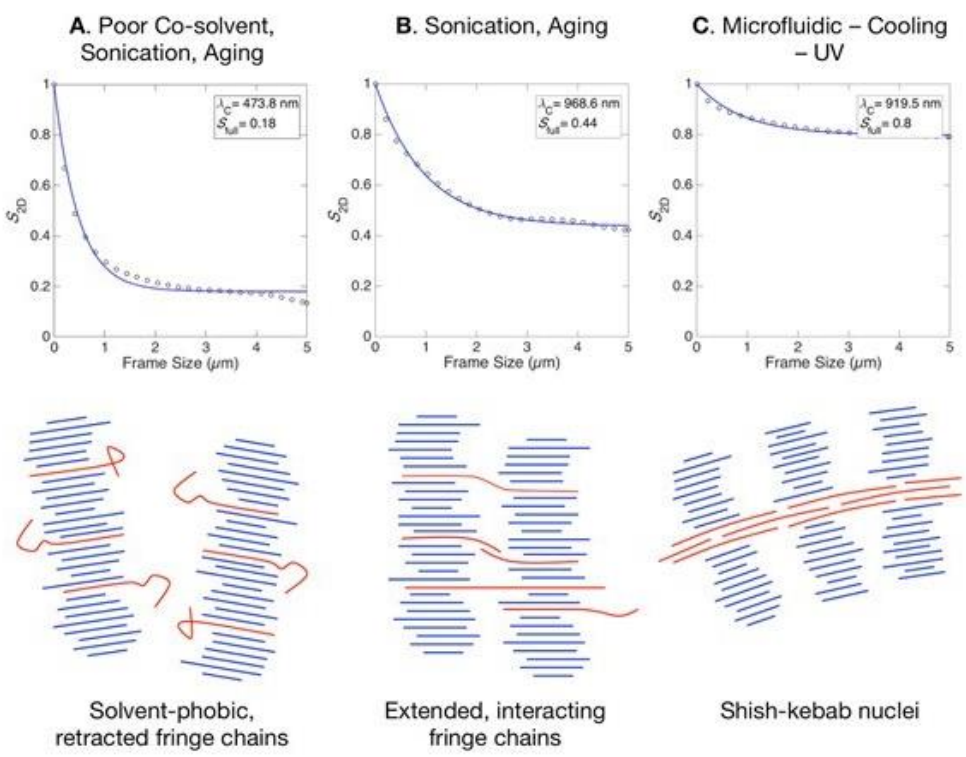

Figure 10: Proposed mechanisms of process-dependent self-assembly based on image processing of AFM images. Adapted with permission from Ref. 71. Copyright American Chemical Society 2017.

While AFM analysis presents a generalizable structure-property relationship that is applicable across a wide range of solution preprocessing techniques, it provides little insight on the role of processing to obtain these structures. It is more desirable to seek complete process-structure-property relationships to be able to apply knowledge on an industrial scale, or to transfer knowledge to another polymer system. However, developing global process-structure-property relationships, even under highly controlled processing conditions, is a challenging task.

1.3 Motivation and Outline of Thesis

Thematically, this work focuses on developing solution blending processes that result in the formation of interconnected polymer networks for enhanced electronic properties. **Chapter 2** introduces the array of processing methodologies and characterization techniques used throughout this thesis to probe for process-structure-property relationships.

Chapter 3 introduces an approach where blends of differing molecular weight are nucleated to investigate the role of chain length on network interconnectivity.

Chapter 4 proposes a processing approach that blends pre-nucleated P3HT and amorphous P3HT to form interconnected nanofibrillar structures. The impact of the sample molecular weight of both seeds and amorphous chains was explored. The results found in traditional batch studies were then applied to a continuous flow processing system.

Chapter 5 discusses blending time-dependent self-assembly with poor solvent driven assembly. Results are generalized to demonstrate that this approach is applicable beyond P3HT to PBTTT.

Chapter 6 applies material informatics approaches to identify promising processing variables for future experiments. Literature databases of both P3HT and polypropylene-talc composites were developed.

Chapter 7 summarizes the main findings in this work and provides guidance on future work.

CHAPTER 2. MATERIALS AND EXPERIMENTAL METHODS

In this chapter, the materials, methods and data-processing techniques used across all studies are presented. Specific techniques used only for a single study will be presented in the corresponding chapter.

2.1 Materials

Regioregular P3HT (PTL 15-12, PTL 16-08, BS23-48) was purchased from Rieke Metals Inc. Anhydrous chloroform with amylenes as stabilizers, dichlorobenzene, and 2-methylpentane (2-MP) were purchased from Sigma-Aldrich. All materials were used without purification. The molecular weights and polydispersity of all P3HT samples were provided by Rieke Metals Inc. and determined using a GPC relative to polystyrene standards with 1,2,4-trichlorobenzene as the eluent as shown in **Table 1**.

Table 1: Molecular weight, polydispersity index and regioregularity of the P3HT samples studied.

	Rieke Metals Inc.			Internal	
Sample Name	M_w (kDa)	PDI	Regioregularity (%)	M_w (kDa)	PDI
P3HT-L	37	2.0	96	41	2.0
P3HT-M	58	2.1	96	66	2.0
P3HT-B	-	-	-	74	2.6
P3HT-H	95	2.3	97	104	2.2

2.2 Experimental Methods

2.2.1 Solution Processing of Poly(3-hexylthiophene)

All solution processing was conducted in 20 mL borosilicate glass scintillation vials. For each experiment 10 mg of P3HT was dissolved in 2 mL of chloroform at 55 °C for 20 min. After complete dissolution, the solutions were cooled in ambient air to room temperature for 15 min. The vial was then exposed to UV irradiation by use of a hand-held UV lamp (Entela UVGL-15, 5 $mW \cdot cm^{-2}$, 254 nm) for 8 min. During UV exposure, the vial was placed on a magnetic stirrer and subjected to a 300 rpm stir. During UV exposure, a notable color change from bright orange to dark purple was observed, indicating P3HT aggregation in solution. A dark ring of solid P3HT was also formed at the glass−UV lamp interface, associated with precipitation of aggregates. The preaggregated solutions were then stored in the dark under ambient conditions for the specified amount of solution aging time.

2.2.2 Organic Field Effect Transistors

The OFET transistor substrates were purchased from Rogue Valley Microdevices with heavily n-doped silicon wafers and 300 nm thick layer of thermally grown SiO_2. The n-doped silicon served as the gate electrode, while the SiO_2 layer served as the gate dielectric in a bottom-gate bottom-contact configuration. Source and drain electrodes, consisting of 3 nm of Cr as an adhesion layer and 50 nm of Au, were deposited via standard photolithography lift-off techniques, followed by E-beam evaporation of the metals onto the SiO_2 surface. After electrode deposition, the wafers were cleaned using an ultrasonic bath before being sequentially rinsed with acetone, methanol and IPA. The final transistors

were then cleaned with UV-ozone (Novascan PSD-UV) to remove organic contaminants including residual photoresist. The semiconducting layer was deposited on the transistors via blade coating using a homemade vacuum chuck equipped with a motorized linear stage (A-LSQ150A-E01, Zaber) at a blade speed of 2.0 mm s^{-1} and blade height of 10 μm. The coated transistors were then moved from the ambient environment to a vacuum oven set at 55°C overnight to remove any residual solvent.

Field effect transistor properties were measured in a nitrogen glovebox using an Agilent 4155c semiconductor parameter analyzer. The charge carrier mobility and threshold voltage were calculated in the saturation regime (V_{GS} = -80 V with V_{DS} swept from 80 to -80 V) by fitting the following equation to the transfer plots of the drain current (I_{DS}) versus the gate voltage (V_{GS}):

$$I_{DS} = \frac{WC_{ox}}{2L}\mu(V_{GS} - V_t)^2 \quad (1)$$

where W is the channel width (2 mm), L is the channel length (50 um), C_{ox} is the capacitance per unit area of the SiO_2 dielectric layer (1.15 x 10^{-8} F cm^{-2}). The on/off ratio was calculated as the maximum drain current measured when a negative bias is applied divided by the minimum drain current measured when a positive bias is applied.

2.2.3 UV-Vis Absorption Spectroscopy

Solution and thin film UV-Vis absorption spectra were recorded using an Agilent HP 8510 UV-Vis spectrophotometer. Solutions measurements were obtained by depositing 30 μL of solution between two glass coverslips secured with a clip. Corresponding thin films were blade coated onto precleaned glass slides using the same procedure as the OFET

devices. Polarized UV-Vis measurements were also obtained using this spectrophotometer by polarizing the incident light.

2.2.3.1 Aggregate Fraction Calculation

The relative degree of polymer aggregation in solution was estimated by deconvoluting the spectra into amorphous and aggregated contributions through Frank-Condon fits.[71-73] The aggregate absorption (A) of P3HT was modeled according to

$$A(E) \propto \sum_{m=0} \left(\frac{S^m}{m!}\right) \times \left(1 - \frac{We^{-S}}{2E_p} \sum_{n \neq m} \frac{S^n n!}{n!\, n-(m)}\right)^2 \times \exp\left(\frac{\left(E - E_{0-0} - mE_p - \frac{1}{2}WS^{me^{-s}}\right)^2}{2\sigma^2}\right) \quad (9)$$

where $E_{0\text{-}0}$ is the 0-0 transition energy of the aggregate, E_p is the frequency of the vibrionic transition (0.179 eV), σ is the width of the Gaussian line shape, S is the Huang-Rhys factor (1), m (4) and n (4) represent the number of vibrational excitations, and W is the exciton bandwidth.[74-75] The values of W, σ, and a proportionality constant are the fitting parameters for this fit. As a single vibrational progression was not able to accurately model the aggregate absorption, the approach by Kohler *et al.* with two distinct and equally space vibrionic progressions was utilized.[73] The fraction of aggregates was obtained by dividing the area under the aggregate fit curve from the total area under the absorption curve. This process is illustrated in **Figure 11.**

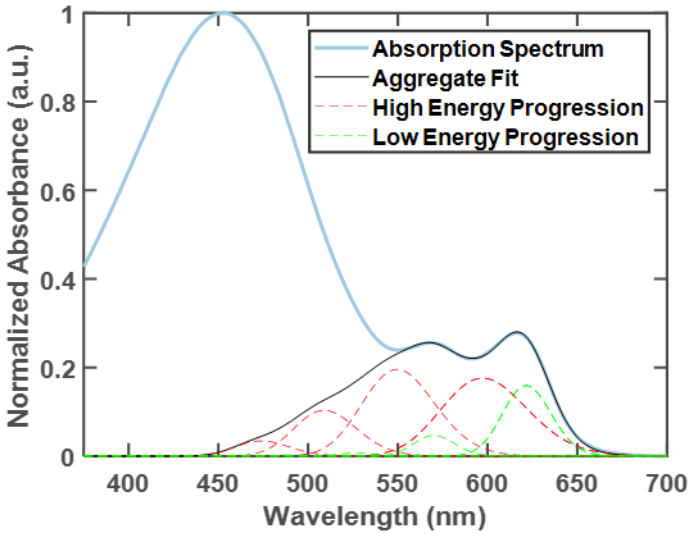

Figure 11: Example Frank-Condon fits to determine the aggregate fraction from linear UV-vis absorption spectra of P3HT.

2.2.3.2 Exciton Bandwidth Calculation

A weakly interacting H-aggregate model was developed by Spano *et al.* to extract polymer conjugation length from the absorption spectra of conjugated polymer thin films and has been applied extensively to P3HT. [72, 76-78] In this approach, the ratio of the (0-0) and (0-1) intensities is related to the Coulombic coupling between neighboring thiophene units through the exciton bandwidth, *W*, of the aggregates. The exciton bandwidth describes the conjugation length and thus intrachain order; a decrease in *W* is associated with an increase in conjugation length and thus a more ordered aggregate. The values of *W* can be estimated as:

$$\frac{I_{0-0}}{I_{0-1}} = \left(\frac{1 - \frac{0.24W}{E_p}}{1 + \frac{0.073W}{E_p}} \right)^2 \quad (10)$$

where $I_{0\text{-}0}$ and $I_{0\text{-}1}$ are the intensities of the (0-0) and (0-1) transitions, respectively, and E_p is the vibrational energy of the symmetric vinyl stretch (taken as 0.18 eV).[71]

2.2.3.3 Dichroic Ratio Calculation

The dichroic ratio, $R=A_{\perp}/A_{\parallel}$, was utilized to quantify the anisotropy of polymer chain backbones. The ratio is defined as the absorption of the (0-0) peak perpendicular to the blade coating direction over the absorption in the parallel direction. A value of 1 will indicates an isotropic structure, while larger values indicate enhanced alignment.

2.2.4 Polarized Optical Microscopy

Polarized Optimal Microscopy (POM) images of the thin films were taken using a Leica DMRX optical microscope equipped with rotatable polarizer and analyzer and a Nikon D300 digital SLR camera. The extinction and reemergence of light as the sample is rotated from 0 to 45° is driven by the formation of highly aligned crystalline domains with long range order.

2.2.5 Atomic Force Microscopy

AFM images were obtained from the same OFET devices used for electrical characterization, using a Bruker Dimension Icon atomic force microscopy system in tapping mode with n-type silicon tips (HQ:NSC14, MikroMasch).

2.2.6 Grazing Incidence X-ray Scattering

GIWAXS measurements were carried out on beamline 11-3 at the Stanford synchrotron radiation light source (SSRL). The beam was kept at an energy of 12.7 keV and critical angle of 0.13°. A LaB6 standard sample was used for calibration and the software WxDiff was utilized to reduce the 2D scattering maps into 1D intensity versus q-spacing plots. Small angle X-ray scattering (SAXS) and wide-angle X-ray scattering (WAX) measurements were conducted at the Pohang Accelerator Laboratory using sucrose as the calibration standard.

CHAPTER 3. A POLYMER BLEND APPROACH FOR CREATION OF EFFECTIVE CONJUGATED POLYMER CHARGE TRANSPORT PATHWAYS

3.1 Introduction

While semicrystalline semiconducting polymers can exhibit macroscopic charge-transport through amorphous domains, electrical properties can be improved through increased molecular ordering.[29, 79-80] In the case of the workhorse polymer, poly(3-hexylthophene) (P3HT), π-π stacking between individual chains can lead to fibrillar networks embedded in an amorphous matrix. These fibers enable charge transport in directions along an individual polymer backbone and through the fiber in the π-π stacking direction.[42] Therefore, controlling the processing conditions to repeatedly target optimized structures in polymeric semiconductors is paramount for the large-scale adoption of these technologies for electronic devices.

Theoretical and experimental efforts have focused on understanding relationships between self-assembly at the molecular level and its role in charge transport.[41, 81-83] Fundamental studies conducted by Kline *et al.* and Zen *et al.* demonstrated tunability of charge mobility over several orders of magnitude by changing the P3HT molecular weight (MW).[53, 57, 84-85] Conventional transport theories suggest that more ordered and crystalline low molecular weight P3HT should exhibit higher transport characteristics over more disordered high molecular weight samples.[86] However, the observed trend of increasing mobility with increased chain length suggests that mesoscale ordering and the formation

of a percolative network, rather than local crystallinity, is more influential for high charge transport. For instance, Noriega *et al.* compared field effect mobility, paracrystalline disorder, and activation energies of trap states of both semicrystalline and amorphous conjugated semiconductors from the literature to relate local disorder and aggregation to charge transport.[29] They concluded that transport in polymer systems is limited by interchain disorder, setting the requirement for high local crystallinity and the presence of "tie-chains" to promote long range charge delocalization. These findings were corroborated by recent studies related to P3HT process-structure-property relationships.[55, 63, 87-88]

Combined, the investigations suggest two microstructural features that are important for enhanced charge transport: 1) electron delocalization arising from highly ordered crystalline domains and 2) interconnectivity between crystalline domains on the meso- to macroscale to form a percolative charge transport network that spans the amorphous polymer matrix.

Manipulation of the polymer molecular weight distribution has been suggested as an approach to satisfy both microstructural requirements for enhanced charge transport[86]. In practice, controlling polymerization to target a desired molecular weight distribution is difficult.[89] Alternatively, targeted molecular weight distributions can be obtained by blending conjugated polymer samples with known weight-average molecular weights (M_w) and polydispersity indices (PDI). Aiming to balance the degree of local crystallinity with aggregate interconnectivity, Ma *et al.* applied this approach to fabricate organic photovoltaics using low and high molecular weight P3HT.[90] Enhanced power conversion efficiencies were observed with the blend, but limited characterization provided few mechanistic insights. Koppe *et al.* blended high (M_w = 153 kDa) and low MW (M_w = 26

kDa) P3HT and observed that the enhanced solubility of low molecular weight chains reduced the propensity of the system to undergo gelation.[91] The improved processability of the blended solution with balanced low and high molecular weight chains coincided with improved photovoltaic efficiency, compared to only using high MW chains. Himmelberger *et al.* studied blends of 8 kDa P3HT with higher molecular weight samples (29, 42, and 61 kDa), and observed a decrease in mobility as the relative amount of low molecular weight polymer was increased.[92] Analysis of UV-vis absorption spectra indicated that the presence of small chains impacted neither intrachain disorder nor the ability of chains to aggregate. Rather, the decrease in mobility was attributed to a decrease in the number of long polymer chains that bridge regions of high crystallinity (referred to as tie chains), probed *via* a reduction in paracrystallinity (X-ray diffraction) and interchain order (UV-vis). However, the absolute value of charge carrier mobility in this study was relatively low; recent advances in the processing and deposition of aligned P3HT nanofibers have yielded mobilities at least an order of magnitude higher. The aligned structure of such resultant thin films provides an opportunity to study the impact of molecular weight blends at the higher end of performance.[66, 69] Furthermore, detailed characterization of the polymer solution state and deposition process in a more controlled setting can help bridge the gap between lab scale studies and the manufacturing environment.

Herein, we investigate the impact of blending distinctly different molecular weight samples of P3HT on the self-assembly of polymer chains into interconnected polymer structures. The polymer solutions were preprocessed with low-dose ultraviolet (UV) irradiation and solution aging, which was previously demonstrated to influence both aggregation and mobility.[50, 66] UV irradiation was used to initiate polymer self-assembly

into nanofibrillar structures, while further aggregation was driven by time-dependent self-assembly (solution aging). The impact of the as-formed P3HT network on charge transport was characterized by fabrication of organic field-effect transistor (OFET) devices. Analysis of the UV-vis solution and thin-film absorption spectra, grazing incidence wide angle X-ray scattering (GIWAXS), atomic force microscopy (AFM), and polarized optical microscopy images (POM) informed mechanistic understanding of the relationships between molecular weight, the resulting distribution of molecular weights, and charge transport. Overall, blending of different molecular weight polymers was demonstrated to be a viable approach to achieve enhanced long-term solution stability, an essential characteristic for the development of stable semiconductor inks.

3.2 Results and Discussion

3.2.1 OFET Device Performance

Four P3HT samples having a range of molecular weights and polydispersity index values (**Table 1**; reported values include those provided by Rieke Metals and those measured in-house) were evaluated to investigate how the *distribution* of polymer chain lengths impacts process-structure-property relationships. Sample selection was guided by prior reports demonstrating a plateau in charge carrier mobility for P3HT having a molecular weight between about 35-40 kDa and about 100 kDa, despite significant differences in thin-film morphology. [86] Samples of 37 kDa (P3HT-L, low MW) and 95 kDa (P3HT-H, high MW) P3HT were blended in a 1:1 mass ratio to generate the P3HT-B (blend) sample. A 58 kDa (P3HT-M, medium MW) sample having similar M_w to the blend

but smaller PDI was selected as the control. The GPC results showing the distribution of molecular weights prior to mixing are shown in **Figure 12.**

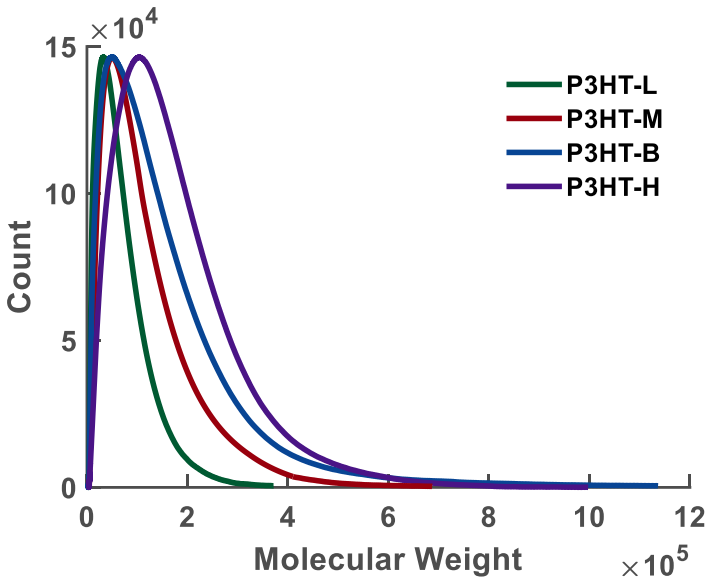

Figure 12: Molecular weight distributions measured by GPC for all four P3HT samples.

P3HT charge transport characteristics were characterized by evaluation of charge carrier mobility (μ) using an OFET device architecture. **Figure 13a** illustrates the process to produce blade-coated films from solutions treated with 8 minutes of UV irradiation followed by solution aging. This method has been shown to deposit uniaxially aligned nanofibers that are perpendicular to the direction of the source and drain.[50, 66] These studies investigated charge transport anisotropy in P3HT and uncovered strong correlations between backbone alignment (AFM, dichroic ratio) and charge transport. It has been suggested that anisotropic alignment leverages enhanced transport properties along the conjugated backbones compared to charge transport in the π-π stacking direction. The average mobility at Day 0 (immediately after UV exposure) increased with average molecular weight, as shown in **Figure 13b**. Upon aging, P3HT-H demonstrated a nearly

linear decrease in μ, from 0.14 cm^2/V-s on Day 0 to 0.05 cm^2/V-s on Day 6. In contrast, P3HT-B displayed the highest mobility on Day 2, namely, 0.15 cm^2/V-s, a value that was similar to the control, P3HT-M (0.14 cm^2/V-s). Notably, these samples retained their mobility above 0.1 cm^2/V-s over the course of solution aging for 6 d. The highest observed μ for P3HT-L was 0.11 cm^2/V-s on Day 2, after which μ significantly decreased to 0.07 cm^2/V-s on Day 6.

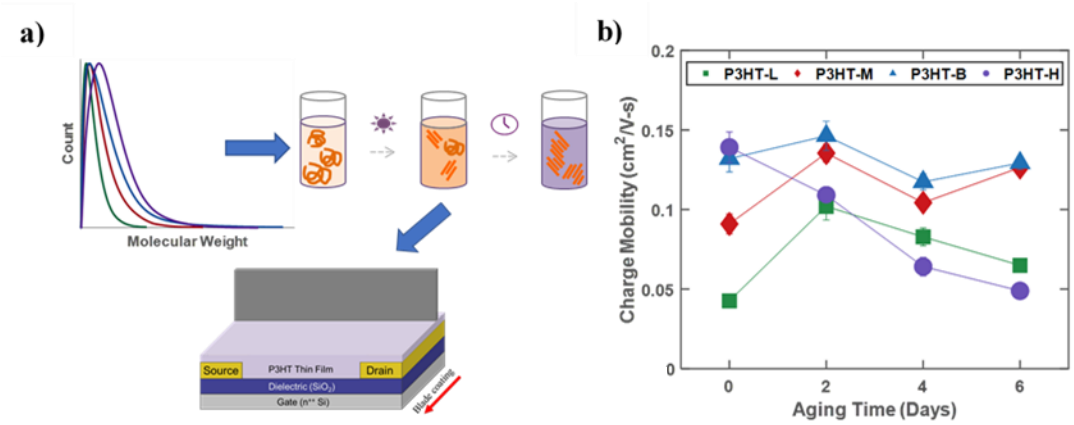

Figure 13: a) Overview of device processing method including molecular weight distribution, UV irradiation, solution aging and blade coating deposition onto transistors. b) Average charge carrier mobilities obtained with OFETs as a function of molecular weight and days aging. Error bars represent standard error.

Figure 14 displays the transfer curves obtained for all samples, which are typical of p-channel OFETs operating in the accumulation mode.[20] High threshold voltages (V_T) and off currents (I_{off}) present in all samples can be attributed to residual doping or charge traps at the P3HT-oxide dielectric interface.[93-94] Tabulated values of V_T and on/off ratios for all samples are provided in **Table 2** and **Table 3**, respectively. P3HT-L and P3HT-B exhibited consistent V_T between ca. 15 and 40 V across all days aging; while P3HT-M and P3HT-H displayed a significantly larger range. It is hypothesized that the presence of a larger distribution of low M_w chains in the P3HT-L and P3HT-B samples enabled improved

packing at the dielectric interface, reducing the development of shallow traps from aggregates.[95] Moreover, the relatively high I_{off} values for all aged samples (I_{off} ~10^{-5}-10^{-6} amps) compared to the Day 0 samples (I_{off} ~10^{-7} amps) suggests the presence of O_2 dopants from processing under atmospheric conditions.[96-97] No apparent correlations between molecular weight and on/off ratios were observed, suggesting that all samples likely exhibited similar levels of O_2 doping. The development of processing methods to remove these dopants remains an active research area to enable low cost manufacturing in ambient environments.[98-100]

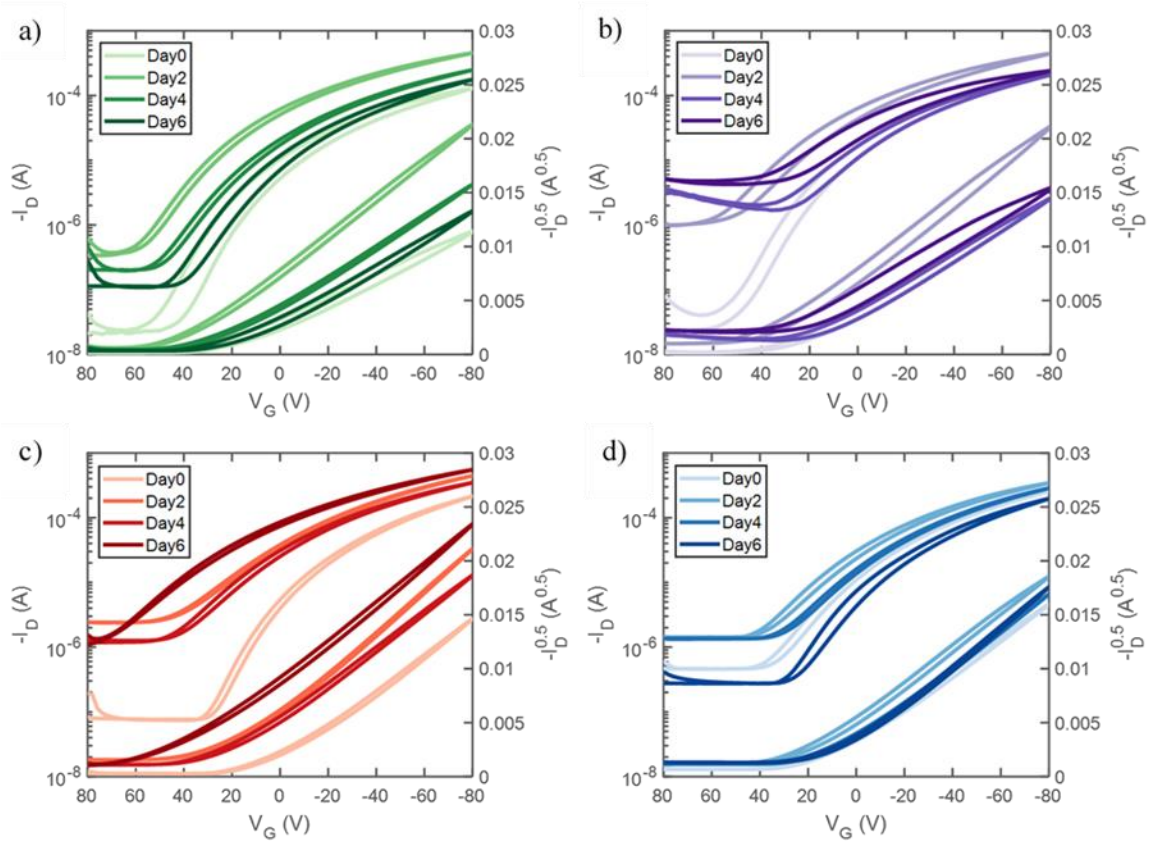

Figure 14: Representative transfer curves for a) P3HT-L, b) P3HT-H, c) P3HT-M, and d) P3HT-B samples bladed coated onto bottom-gate, bottom-contact transistors in the saturation regime (V_{ds} = -80 volts).

Table 2: Average and standard errors of threshold voltages extracted from transfer curve analysis.

	Day 0	Day 2	Day 4	Day 6
P3HT-L	31.50 ± 0.14	39.08 ± 5.18	24.49 ± 1.58	27.39 ± 4.98
P3HT-M	7.91 ± 1.40	24.60 ± 1.73	27.09 ± 1.52	54.06 ± 1.74
P3HT-B	27.04 ± 2.46	34.09 ± 2.52	22.70 ± 2.24	17.86 ± 2.19
P3HT-H	28.68 ± 2.33	49.20 ± 2.21	31.59 ± 4.75	69.80 ± 3.10

*units: Volts (V)

Table 3: Average and standard errors of on/off ratios extracted from transfer curve analysis.

	Day 0	Day 2	Day 4	Day 6
P3HT-L	4.11 ± (1.28) $x10^3$	8.09 ± (1.38) $x10^2$	8.41 ± (1.75) $x10^2$	1.69 ± (0.51) $x10^3$
P3HT-M	1.70 ± (0.37) $x10^3$	4.41 ± (1.71) $x10^2$	1.87 ± (0.34) $x10^2$	2.24 ± (0.39) $x10^2$
P3HT-B	7.72 ± (4.95) $x10^3$	1.56 ± (0.27) $x10^2$	3.49 ± (0.98) $x10^2$	1.22 ± (0.63) $x10^3$
P3HT-H	6.57 ± (3.05) $x10^3$	3.94 ± (0.67) $x10^2$	2.27 ± (1.28) $x10^3$	7.01 ± (2.89) $x10^2$

Longer-term aging of the P3HT-B and P3HT-M solutions (up to 14 days) was also investigated to evaluate its impact on charge transport performance and importantly, semiconducting ink shelf-life. At Days 10 and 14, P3HT-B retained mobilities in the range of 0.10 cm^2/V-s (0.10 cm^2/V-s and 0.11 cm^2/V-s respectively), while P3HT-M displayed values of 0.19 cm^2/V-s and 0.16 cm^2/V-s. Note, however, that the increase in mobility observed for P3HT-M was accompanied by large increases in V_T (**Figure 15**). Thus, the

use of lower polydispersity, medium MW semiconducting polymers in low power applications may be less stable over long aging time.[101-102]

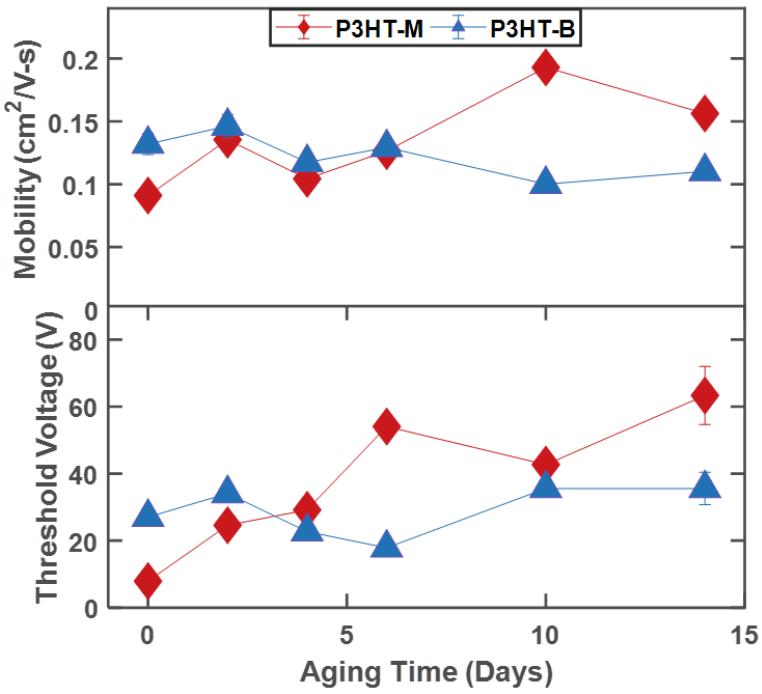

Figure 15: Average mobility and threshold voltages of P3HT-M and P3HT-B samples with aging up to 14 days. Error bars represent standard error of multiple runs.

3.2.2 UV-Vis Characterization

UV-vis absorption spectroscopy was used to quantify nanofiber formation in the P3HT solutions. The solution absorption spectra are presented in **Figure 16.** The broad absorption peak centered at ca. 455 nm accounts for a wide distribution of isotropic amorphous chains in a coiled state.[103] Additionally, peaks at ca. 615 nm and 570 nm correspond to the (0-0) and (0-1) vibronic bands, which are attributed to the relative intra- and interchain coupling of delocalized excitons, arising from P3HT self-assembly into aggregates.[77, 104]

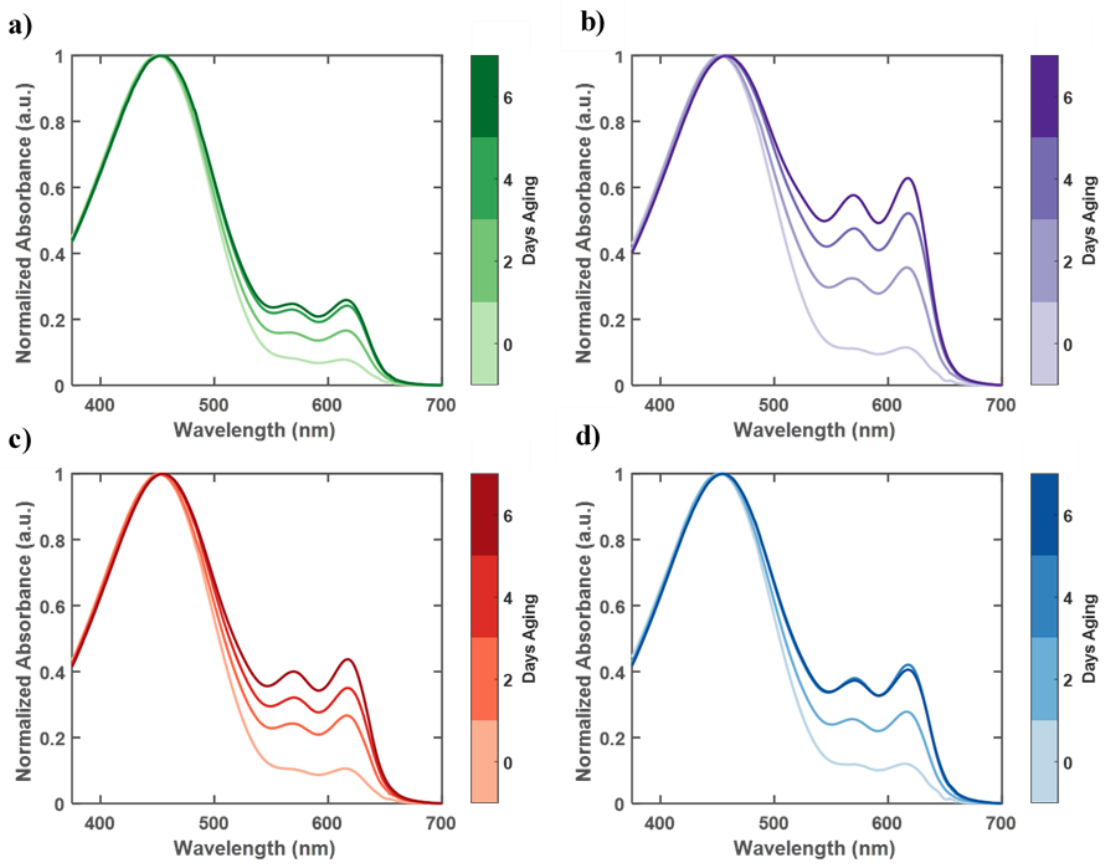

Figure 16: Normalized solution UV-vis absorption spectra of a) P3HT-L, b) P3HT-H, c) P3HT-M, and d) P3HT-B samples after UV-irradiation. The color map corresponds to days aging for each sample with the lightest color representing Day 0 and the darkest Day 6.

The relative degree of polymer aggregation in solution was estimated by deconvoluting the spectra into amorphous and aggregated contributions through Frank-Condon fits.[73, 75] These aggregate fractions are a structural metric describing the degree of chain self-assembly into nanofibers (**Figure 17**), but do not provide insight into the size or absolute quantity of aggregates. Consistent with a nucleation and growth assembly mechanism, all P3HT samples displayed an increase in the aggregate fraction with solution aging after UV exposure.[82] Furthermore, the increase in aggregate fraction was generally higher for samples with larger M_W, and P3HT-B and P3HT-M exhibited similar aggregation behavior. A solubility-dependent driving force provides a straightforward

explanation for the influence of the distribution of molecular weights on the degree of self-assembly probed by solution UV-vis spectroscopy. The longer P3HT-H chains are inherently less soluble than their short chain counterparts due to a reduction in the cohesive energy density and increase in entanglements.

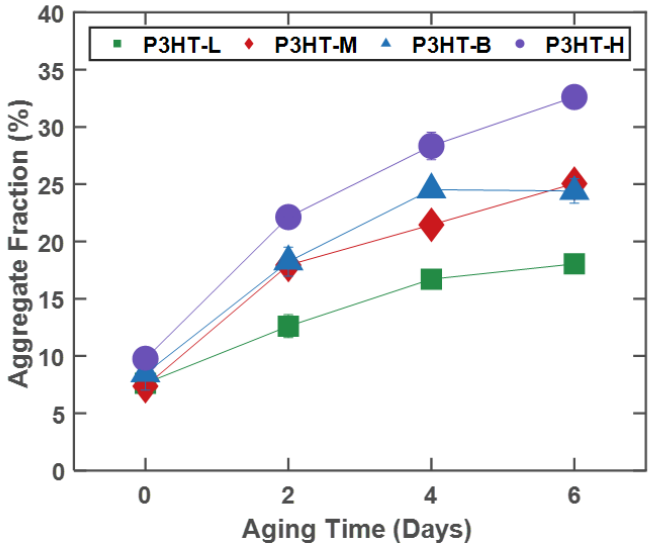

Figure 17: Aggregate fraction as a function of molecular weight distribution and solution aging time.

A weakly interacting H-aggregate model was developed by Spano *et al.* to extract polymer conjugation length from the absorption spectra of conjugated polymer thin films and has been applied extensively to P3HT.[72, 76-78] In this approach, the ratio of the (0-0) and (0-1) intensities is related to the Coulombic coupling between neighboring thiophene units through the exciton bandwidth, *W*, of the aggregates. The exciton bandwidth describes the conjugation length and thus intrachain order; a decrease in *W* is associated with an increase in conjugation length and thus a more ordered aggregate. The values of *W* can be estimated according to:

$$\frac{I_{0-0}}{I_{0-1}} = \left(\frac{1 - \frac{0.24W}{E_p}}{1 + \frac{0.073W}{E_p}} \right)^2 \quad (10)$$

where $I_{0\text{-}0}$ and $I_{0\text{-}1}$ are the intensities of the (0-0) and (0-1) transitions, respectively, and E_p is the vibrational energy of the symmetric vinyl stretch (taken as 0.18 eV).[71]

The thin film absorption spectra of all samples analyzed are shown in **Figure 18**. A general decrease in *W* was observed for all molecular weights as the solution aging time progressed (**Figure 19**). Furthermore, the exciton bandwidth is inversely correlated with molecular weight. This correlation was previously studied by Paquin *et al.*[103] : P3HT with M_w<50 kDa exhibited a *W* of ca. 81 meV while an abrupt transition to *W* ~21 meV was recorded for M_W >50 kDa. The transition was attributed to a microstructural change from a highly crystalline, chain extended phase present in low M_w polymer, to a two-phase morphology composed of an interconnected network of crystalline and amorphous regions.[40, 84, 86] While the solution aggregation results presented herein suggest increased crystallinity for higher M_w samples, it is conceivable that for samples with M_w >50 kDa, extended chains provide for interconnected aggregates (as per Paquin *et al.)* leading to the observed electrical results. P3HT-L is likely too low to form a large interconnected network, and thus charge carrier mobility is limited. In contrast, the longer chain samples are better able to planarize into longer segments that maintain conjugation thereby facilitating higher μ. The lower values of *W* observed for high molecular weight P3HT suggest that long chains can be sufficiently planarized, thereby serving as tie chains.

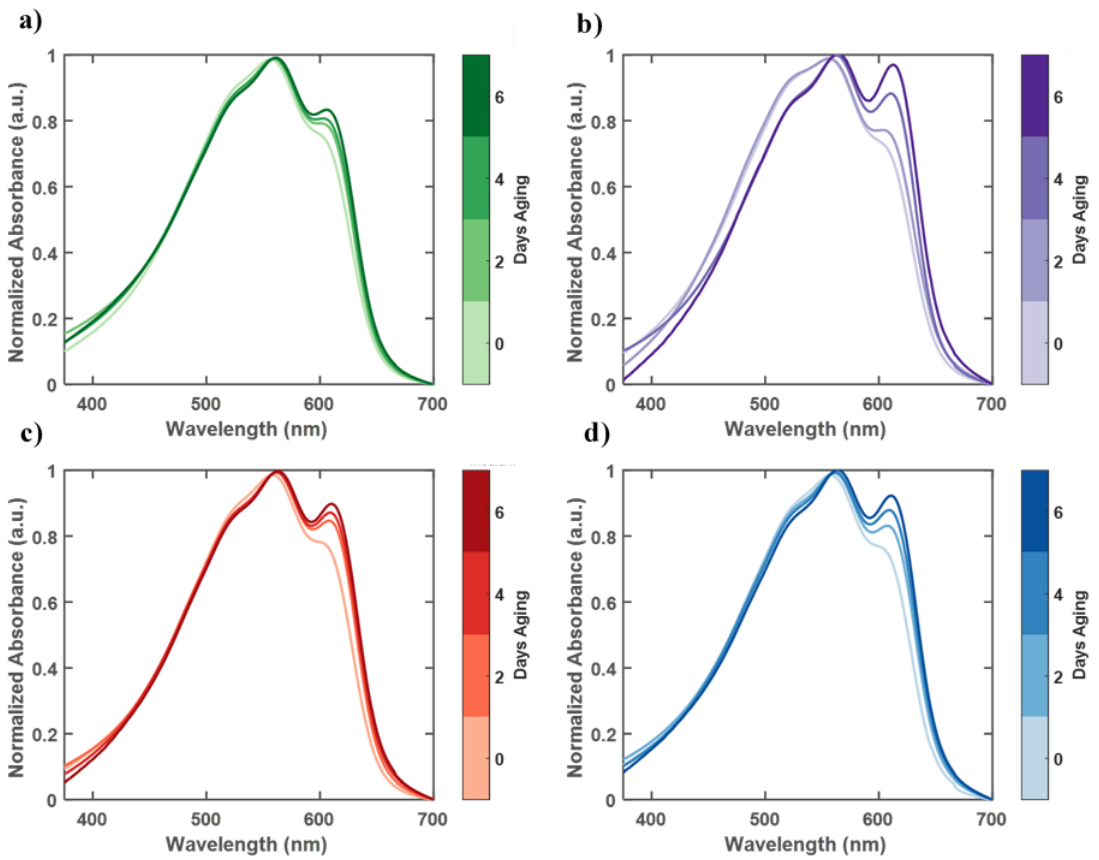

Figure 18: Normalized thin film UV-vis absorption spectra of a) P3HT-L, b) P3HT-H, c) P3HT-M, and d) P3HT-B samples after UV-irradiation. The color map corresponds to days aging for each sample with the lightest color representing Day 0 and the darkest Day 6.

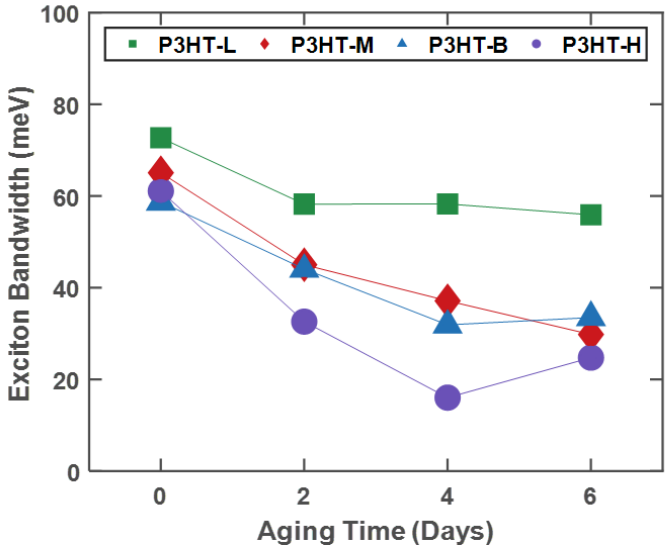

Figure 19: Exciton bandwidth as a function of molecular weight distribution and solution aging time.

Though a decrease in exciton bandwidth with concomitantly larger percolative network is expected to lead to improved electrical performance, enhanced μ was only observed for P3HT-B and P3HT-M. Note that P3HT-H exhibited a linear decrease in μ as *W* decreased from 61 meV to 16 meV upon solution aging from Day 0 to Day 4, followed by a slight increase to 25 meV on Day 6. All samples, regardless of molecular weight or aging time, had similar thin-film aggregate fractions (**Table 4)** so it is unlikely that bulk differences in the overall proportion of crystalline material impacted the electrical properties. More likely, the performance was reduced due to the differences in structural organization mechanisms during drying when starting from solutions with different levels of aggregation. The reduced solubility of long chains led to higher solution aggregate fractions in P3HT-H (>25% after Day 4). As the solution aging time progressed, visible variations in film thickness from inhomogeneous drying became more prominent, accompanied by the deterioration of electrical performance attributes for this sample. This

suggests that an excess of solution aggregation ultimately hinders inter-grain connectivity, possibly because there is less free material to participate in tie-chain formation between aggregates as they come together during drying.

Table 4: Average and standard errors of aggregate fractions extracted by fitting Frank-Condon progressions.

	Day 0	Day 2	Day 4	Day 6
P3HT-L	76.76 ± 0.74	73.12 ± 0.56	74.94 ± 0.30	74.18 ± 0.66
P3HT-M	76.90 ± 0.79	74.72 ± 0.52	76.24 ± 1.31	76.37 ± 1.02
P3HT-B	73.70 ± 1.48	73.45 ± 0.24	74.94 ± 0.86	75.05 ± 1.37
P3HT-H	74.80 ± 0.16	73.13 ± 0.76	75.08 ± 2.78	78.22 ± 1.02

*units: %

GIWAXS patterns were also collected to examine changes in the crystalline texture of the thin films. Lamellar and π-π stacking distances were quantified from the (100) and (010) peaks, respectively, as shown in **Figure 20**. In generally, P3HT-B exhibits lower lamellar stacking distances, suggesting tighter packing compared to P3HT-L and P3HT-H, resulting in improved electrical performance. A constant π-π stacking distance of 3.8 Å for all samples is observed after Day 2. The (100) peaks from the out-of-plane profiles were used to quantify the crystal coherence length and Herman's orientation factor. Plots of these structural metrics as a function of solution aging time exhibit an initial increase followed by a decrease as time progressed from Day 4 to Day 6 for P3HT-H and P3HT-B (**Figure 20d and e**).[5, 65] The sudden decrease suggests that paracrystalline disorder increases at these later aging times. This would be expected to reduce charge carrier mobility; however, mobility was only reduced for P3HT-H.

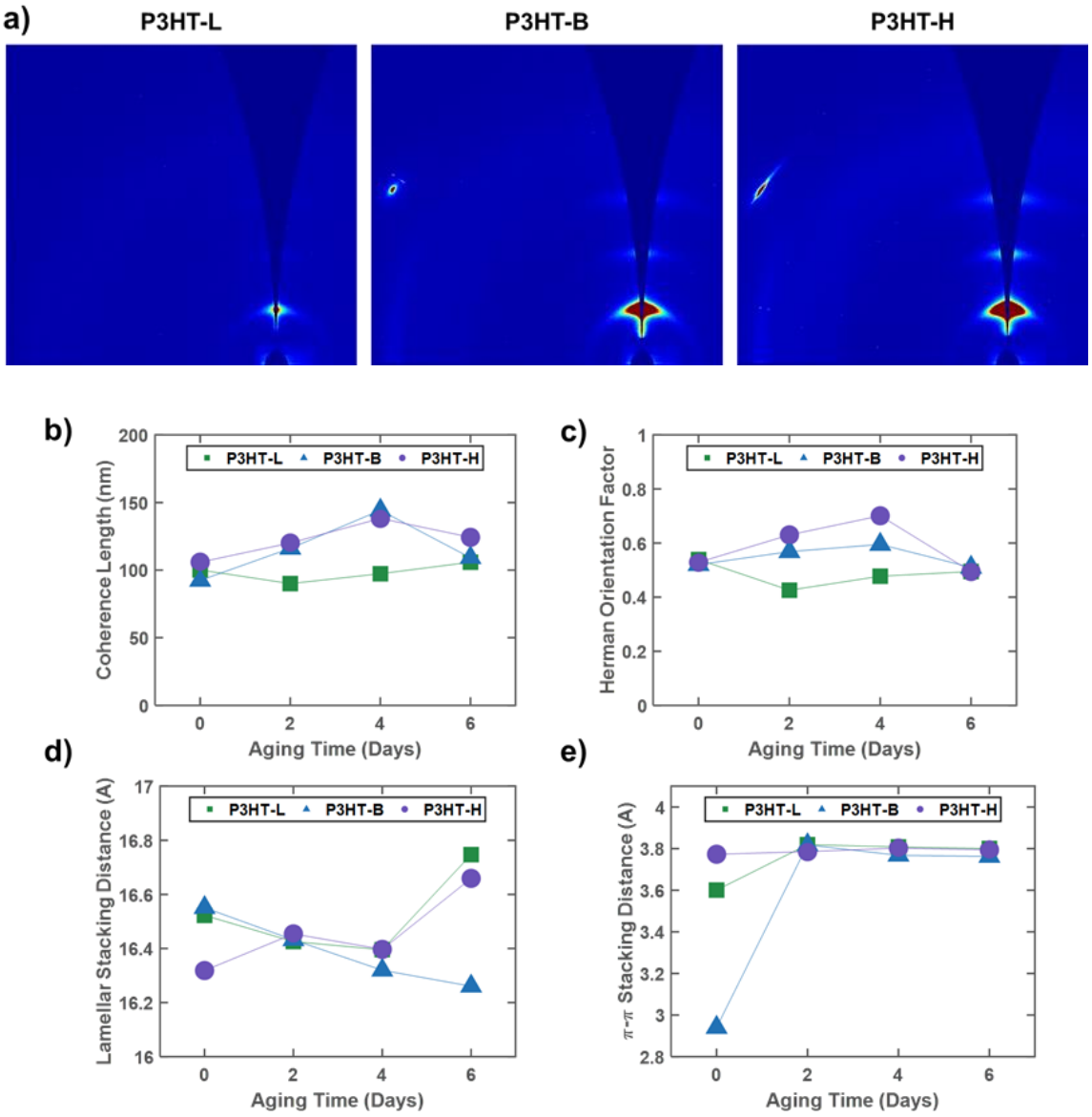

Figure 20: a) Example GIWAX patterns of Day 2 thin films for P3HT-L, P3HT-B and P3HT-H samples. Structural metrics including b) Lamellar stacking distance, c) π-π stacking distance, d) coherence lengths extracted from (100) peaks, and e) Herman orientation factors for P3HT-L, P3HT-B and P3HT-H samples as a function of aging time.

An incremental broadening of the (010) peak was observed for P3HT-H beginning at Day 2 (**Figure 21**) and persisting through Day 6, which is not present for P3HT-B. This suggests that paracrystalline disorder in the π-π stacking direction increased at long aging times for the high-MW sample, but not for the blend, which could explain the difference

in charge carrier mobility. In agreement with the UV-vis analysis (**Figure 17**), the increased level of aggregation in the high-MW sample limits inter-grain connectivity, resulting in an increase in paracrystalline disorder.

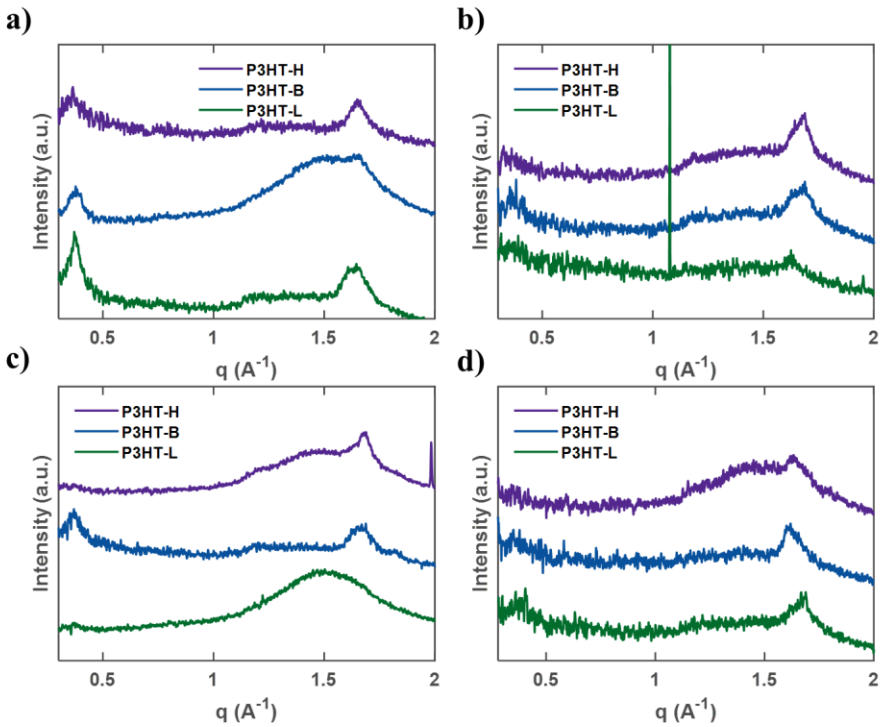

Figure 21: In-plane X-ray scattering profiles of P3HT-L, P3HT-B and P3HT-H samples with solution aging of a) 0, b) 2, c) 4, and d) 6 days of solution aging.

3.2.3 Morphological Characterization

The evolution of thin-film nanofibrillar morphology can help elucidate the role of the molecular weight distribution on polymer self-assembly and its impact on charge carrier mobility. As discerned from the atomic force microscopy (AFM) images in **Figure 22a,** the degree of fibrillar alignment and packing density can be modulated by both polymer molecular weight and post-UV irradiation solution aging time. Immediately after UV irradiation, neither P3HT-L nor P3HT-B exhibited distinguishable features. This is not to say that self-assembled structures had not formed, but rather they were not observed at

the film-air interface. In the P3HT-M and P3HT-H analogs, the few fibers that were evident were randomly orientated and embedded in an apparently amorphous matrix of disordered chains. As solution aging time increased, both the corresponding unidirectional alignment and fiber packing density in the thin films increased; both of which were quantified using an open source image processing algorithm.[70, 105] Borrowing from the liquid crystal community, the degree of fibrillar alignment can be estimated using the orientational order parameter (S_{2D}):[106-107]

$$S_{2D} = 2\langle \cos^2 \theta_n \rangle - 1 \tag{11}$$

where θ_n is the angle between an individual fiber pixel and the director of all fibers, *n*, the average orientation of the population of fibers. An image with fully aligned fibers will have an S_{2D} value of 1, while a random orientation image will have a value of 0. To quantify the packing density, a fiber length density, ρ_{FL}, is defined as the total length of all fibers per image area.[108] High degrees of alignment between neighboring fibers likely imply that the intervening amorphous material is not truly amorphous but has a correlated orientation as well. This has been probed via correlations between fiber alignment and enhanced mobility (**Figure 23**).[108] Whether fiber alignment is caused by tie chains formed in solution, or fiber alignment results in the formation of tie chains during drying, or a combination of both, is difficult to discern.[109]

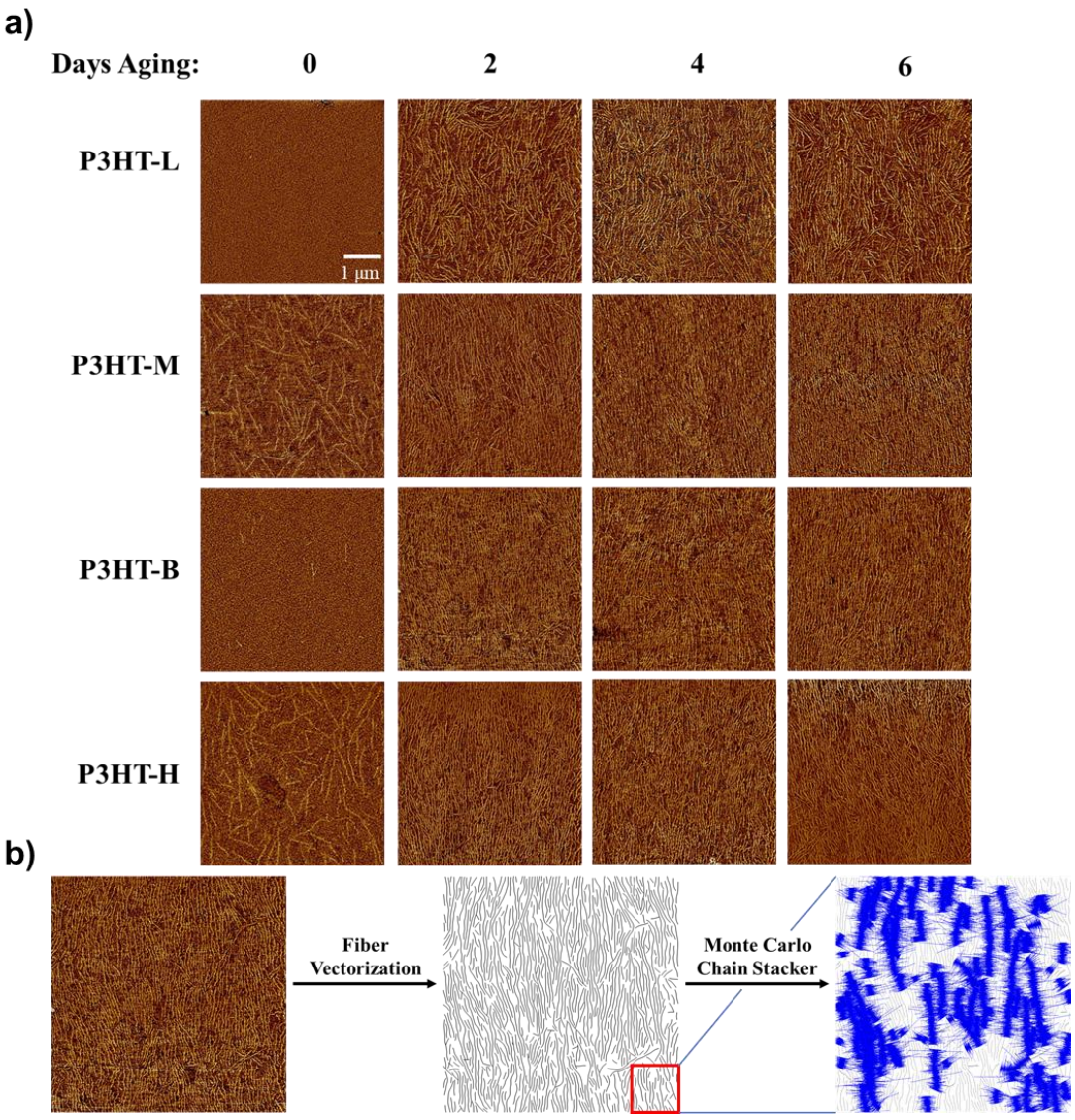

Figure 22: a) AFM phase images (5 x 5 µm) of P3HT thin films deposited by blade-coating P3HT solutions exposed to UV irradiation as a function of molecular weight and solution aging time. b) Illustration of chain backbone vectorization and chain stacking Monte Carlo simulation.

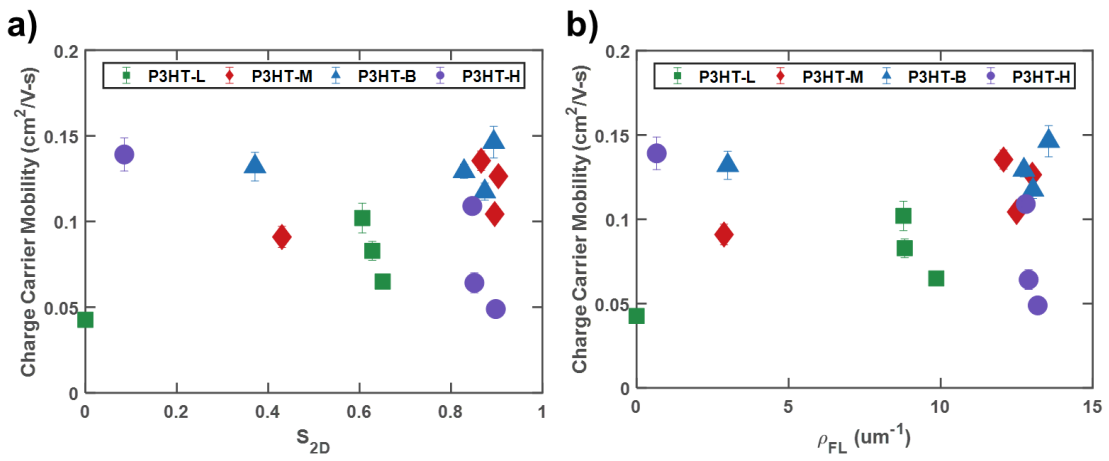

Figure 23: Correlations between mobility and a) orientational order and b) fiber length density as a function of molecular weights for 0 to 6 days aging.

However, knowledge of the location of crystalline grains through AFM as well as the molecular weight distribution of the polymers enables estimation of an upper bound on the number of tie chains that could form between neighboring fibers. Two key assumptions go into this analysis: 1) that there is no chain folding, i.e. every P3HT chain is fully extended, and 2) that only a 2-dimensional layer of polymer chains at the film surface is considered. The density of tie chains is estimated through Monte Carlo "Chain Stacker" simulations that model the spatial arrangement of fully elongated polymer chains on nanofiber backbones extracted from experimentally measured AFM images.[70, 105] Polymer chain lengths were randomly sampled from the measured molecular weight distributions (**Figure 12**), placed orthogonal to the nanofiber backbones and spaced according to π-stacking distances measured from GIWAXS (0.38 nm). **Figure 22b** illustrates the Chain Stacker procedure from raw AFM phase images to simulated chains for P3HT-B on Day 2. Potential tie chain density was calculated as the number of chains from neighboring fibers that intersect a chosen fiber's backbone, per unit length of the backbone. This quantity is averaged across every fiber in the image. It should be stressed that the tie chain

density calculated here represents an upper bound and should not be interpreted as an absolute measurement. Estimations of absolute tie chain densities remain an ongoing challenge in the field.[83, 92] The modeled structures do not attempt to resolve the incorporation of tie chains into a neighboring lattice; only how far each chain could extend and whether it could reach a neighboring fiber.

As shown in **Figure 24** all samples investigated here exhibited low orientational order, fiber packing density, and tie chain density at Day 0, before plateauing at their maximum values on Day 2. P3HT-L exhibited a substantially lower S_{2D} (~0.6), ρ_{FL} (~9), and tie chain density (~0.17 μm^{-1}) compared to the other samples. In light of the electrical performance results, the charge carrier mobility in low molecular weight samples was likely limited by the inability of short chains to interconnect with neighboring nanofibers. In contrast, P3HT-H exhibited significantly higher S_{2D}, ρ_{FL}, and tie chain density with values of 0.9, 13 and 1.77 μm^{-1}, respectively. The P3HT-H films achieved high levels of alignment with chains of sufficient length to form tie chains yet did not produce the expected charge mobility results: charge transport in high molecular weight samples was limited by longer-range (< 5μm) structural inhomogeneity (*vide supra*). Notably, the tie chain densities for P3HT-B (~0.82 μm^{-1}) and P3HT-M (~0.87 μm^{-1}) are similar, despite differences in polydispersity. This result suggests that the average molecular weight is a key determinant of the potential for tie chain formation, rather than the distribution as measured by the polydispersity index.

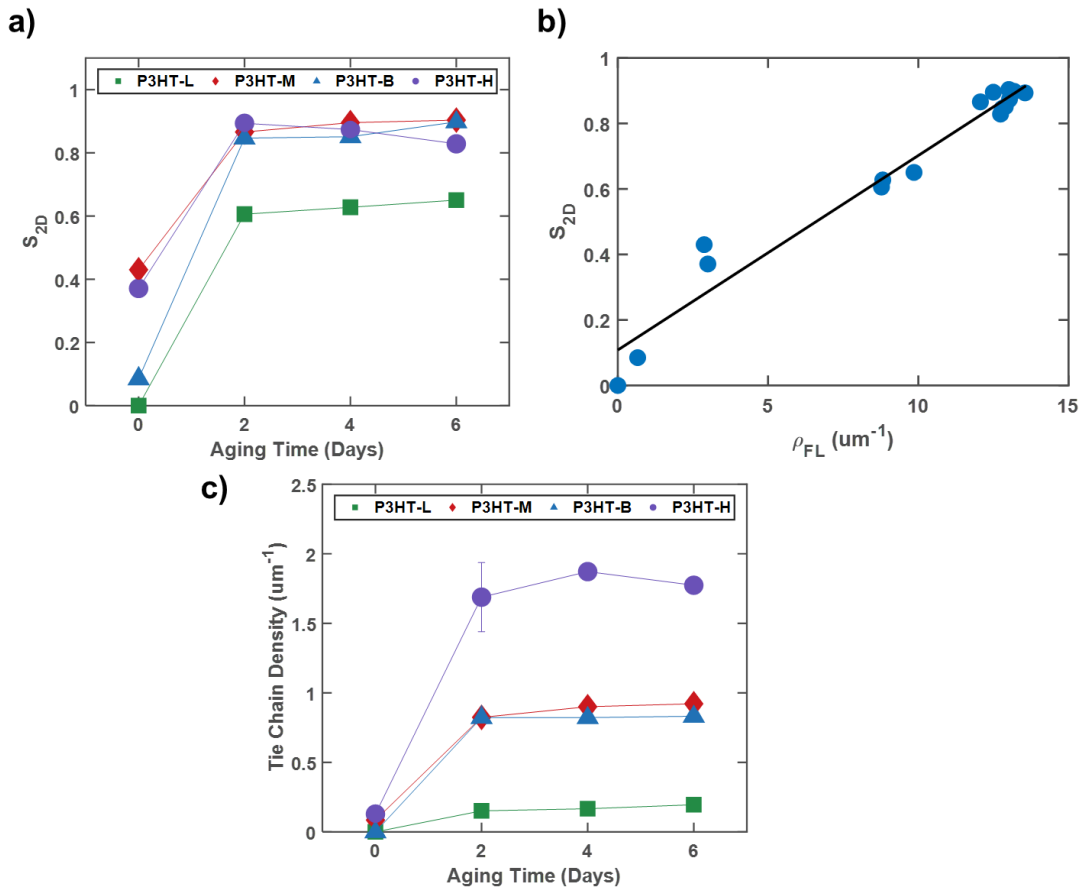

Figure 24: a) Orientational order parameter (S_{2D}) of blade coated thin films. b) Correlation of orientational order with fiber length density. c) Simulated tie chain density from Monte Carlo chain stacking as a function of molecular weight and solution aging time.

Cross-polarized optical microscopy (POM) and linearly polarized UV-vis spectroscopy was used to observe the persistence of alignment at the macroscale. The POM images of all aged samples exhibited clear birefringence with the complete extinction and re-emergence of brightness with rotation from 0 to 45° with respect to crossed polarizers (**Figure 25**). This indicates a highly anisotropic structure that is in agreement with the AFM analysis. The bulk structural anisotropy can be quantified as a function of aging time and molecular weight distribution using the dichroic ratio calculated from UV-vis absorbance spectra (**Figure 26**). This parameter is defined as the ratio of the (0-0) vibronic transition

peak between incident light polarized perpendicular and parallel to the coating direction. The dichroic ratio values generally mirror the AFM S_{2D} and POM results, suggesting that the fibrillar structure probed at the mesoscale by AFM is generally representative of the macroscale structure. Moreover, high dichroic ratio values are consistently observed for P3HT-B and P3HT-M, demonstrating that anisotropic alignment can enable high charge transport properties.

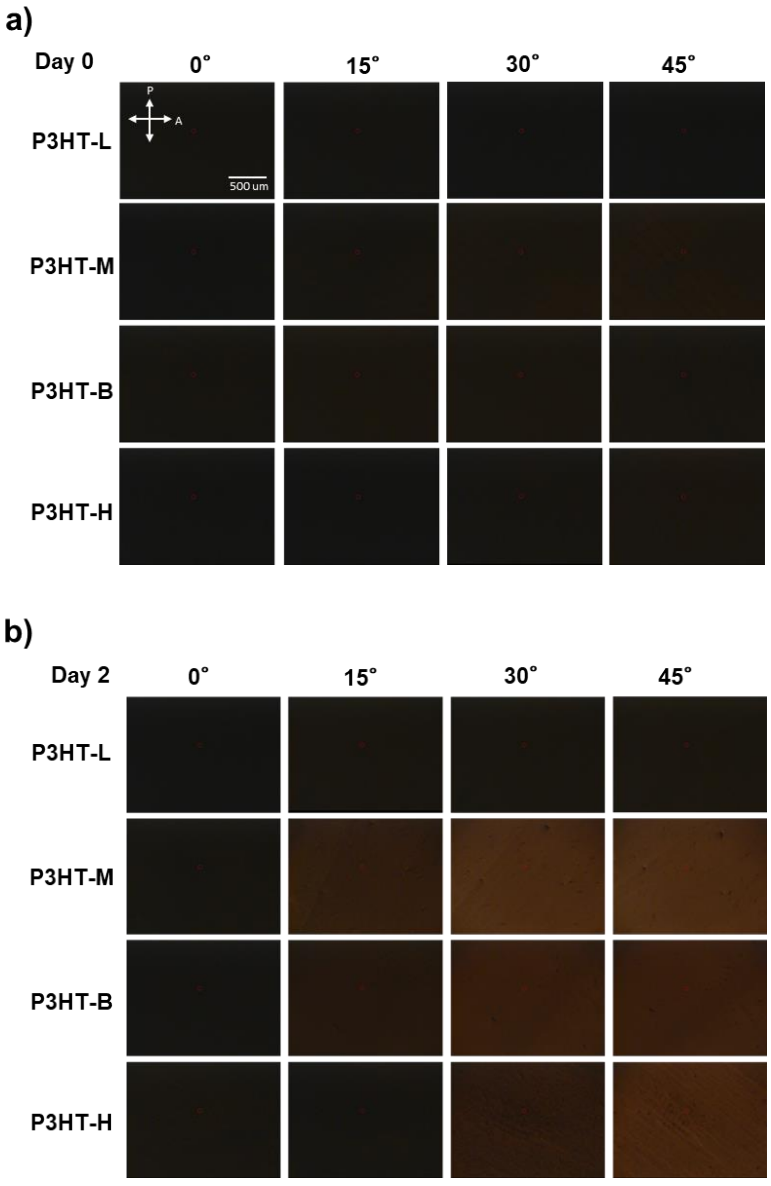

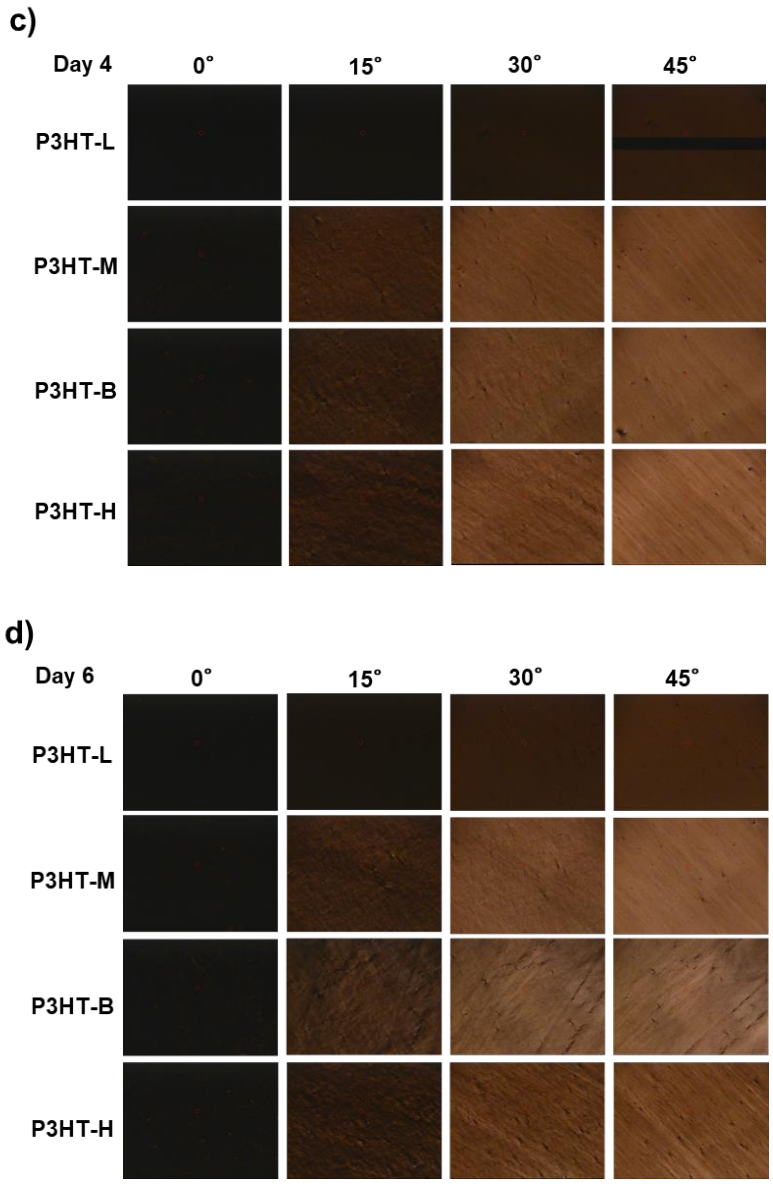

Figure 25: Polarized optical microscopy micrographs as a function of molecular weight, rotated in increments of 15° between polarizers for a) 0, b) 2, c) 4, and d) 6 days solution aging.

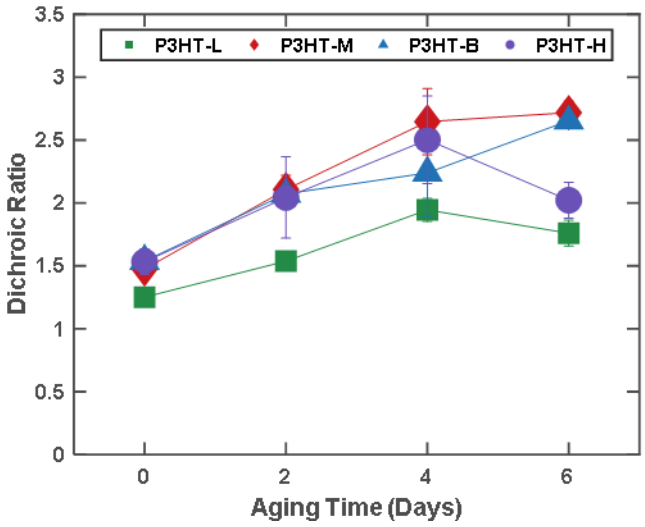

Figure 26: Dichroic ratio indicting the degree of structural anisotropy of P3HT aggregates on the macroscale as a function of molecular weight and aging time.

Backbone alignment however, does not guarantee improved charge mobility as illustrated by P3HT-H. This sample generally exhibited high levels of alignment, but suboptimal charge transport properties. A decrease in the dichroic ratio was observed for P3HT-H at Day 4 and Day 6, mirroring a similar decrease in orientational order (AFM), decrease in crystal coherence length (GIWAXS), and increase in exciton bandwidth (film UV-vis). Taken together, these structural changes suggest the presence of non-ideal, defect-containing P3HT aggregates that cause inhomogeneous drying and interrupt charge transport pathways.

3.3 Discussion

Self-assembly of P3HT in solution and during the film deposition process can be framed as a solubility-driven crystallization problem. Exposure of P3HT chains to low dose UV light is believed to result in a photoexcitation induced conformational change from an aromatic to quinoid structure.[41, 50, 66] In the excited state, enhanced π-orbital overlap

between adjacent thiophene rings results in increased planarization of the polymer backbone. This planarization facilitates the nucleation of ordered supramolecular assemblies through π-π stacking and is enhanced by the chain-length-dependent solubility, in which longer polymer chains favor polymer-polymer interactions over polymer-solvent interactions. Variations in the distribution of molecular weights impact the self-assembly process in two ways: 1) chain solubility, and 2) tie chain formation.[110-113] Chain solubility will impact the growth rate of crystalline nanofibers while the ability to potentially form tie chains between nanofibers will impact the interconnectivity of any as formed network. In this study, the mass concentration of polymer rather than the molar concentration remained constant, further suggesting that the faster aggregation rate of P3HT-H arises from a driving force associated with solubility, rather than polymer chain concentration. An illustration of the proposed self-assembly mechanism is presented in **Figure 27**.

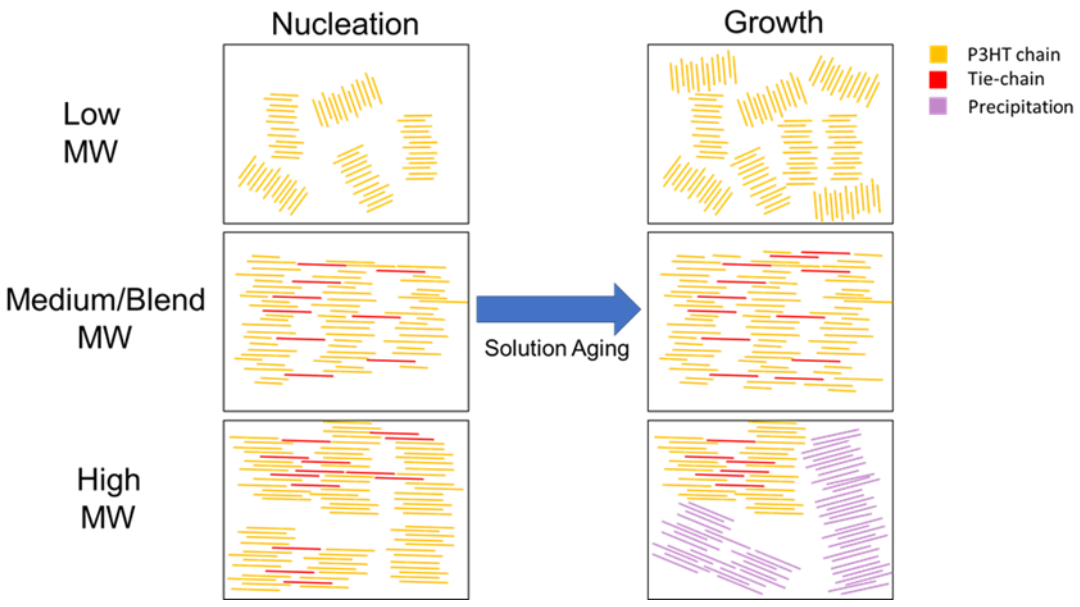

Figure 27: Illustration of proposed mechanism in solution with low M_W (top row), medium/mixed M_W (middle row), and high M_W (bottom row) after nucleation and growth. Low M_W samples enhanced chain solubility limits self-assembly while the short chain lengths limits tie chain formation in subsequent solution aging. Medium/blend samples leverage the enhanced solubility of short chains with tie-chain arising from long chains to form stable percolative networks. High M_W samples form interconnected structures, but limited solubility creates grain boundaries with solution aging.

As discussed above, the solutions prior to deposition start from different aggregate fractions, but the solid films end at approximately the same aggregate fraction. Since fibers rapidly come closer together as solvent evaporates, it is highly probable that the additional aggregation that occurs during drying accounts for some tie chain formation. Thress conditions are necessary to ensure that this final wave of aggregation yields a uniformly interconnected network of aggregates: (1) aggregates should remain suspended as long as possible and not phase separate into precipitates that cease to interact with the rest of the solution, (2) there must be enough free long chains to connect these suspended aggregates as they dry and come into closer contact, and 3) aggregates must be sufficiently aligned to ensure conjugation along the tie chain backbones. The 6-day-aged high-MW solution with

high aggregate fraction presents two problems: large, likely entangled aggregates that phase separate too quickly (shown in **Figure 27**), and a lack of sufficient free material to form additional tie chains. Conversely, the low-MW solutions likely have (1) too few aggregates to start with, and (2) not enough free long chains. In the blend, a moderate amount of aggregated material seems to satisfy both requirements.

Understanding the role of polymer chain length on solubility and self-assembly provides insight into strategies to ensure long term stability of solution (semiconducting ink) formulations required for manufacturability. The proposed formation of tie-chains has implications not only on charge transport, but also on the alignment of nanofibers during blade coating. Solution-based ink formulations that lack robust structural stability will translate into unreliable electrical performance during high-volume, solution printing of low-cost flexible electronics. While filtration techniques could be adapted to remove undesired precipitates, this would add an additional layer of processing.[46] Instead, the results presented here demonstrate that both short and long-term stability can be achieved by tailoring the distribution of semiconducting polymer molecular weights prior to nucleation and growth. While the average molecular weight appears to be more critical than the distribution, over multiple weeks, the blended polydisperse sample exhibited improved stability. Moreover, recent studies on the mechanisms of local aggregation, alignment, and charge transport anisotropy in non-semi-crystalline polymers suggest transferability of this blend approach to balance solubility and polymer network formation to systems beyond P3HT.[29, 109, 114]

3.4 Conclusion

The need to develop interconnected aggregated polymer domains to form a percolative network for enhanced charge transport has been at the forefront of studies pertaining to the design and development of polymer semiconductor solution processing techniques. To date, the polymer electronics community has largely relied on high molecular weight, low polydispersity index materials to attain thin films of such networked structures. The results presented here provide a framework to better understand the interplay between polymer solubility, network interconnectivity and charge transport by varying the distributions of molecular weights across four samples. Herein, it was confirmed that self-assembly of semicrystalline polymers such as P3HT into interconnected networks is indeed dependent on polymer molecular weight: low molecular weight (37 kDa) P3HT displayed slow growth of aggregates after a UV-irradiation induced nucleation step affording poorly interconnected, nonaligned films exhibiting lower charge transport characteristics, while the reduced solubility of high molecular weight (95 kDa) samples of the same polymer resulted in rapid aggregate formation, ultimately leading to inhomogeneous films that interrupted percolative charge transport. The medium molecular weight P3HT sample (58 kDa) and one formulated with a blend of shorter and longer chain length samples (50:50 wt% 37:95 kDa) both displayed superior hole transport characteristics. The results suggest that the solubility characteristics of semiconducting polymers should be optimized in order to leverage polymer solution properties to achieve effective, interconnected charge transport pathways. Furthermore, the similar performance attributes between the blend and medium molecular weight materials, suggests that

blending of multiple batches of the same conjugated polymer is a viable approach to achieving robust and reproducible electronic performance.

From an applications perspective, achieving and maintaining stable electrical performance from thin films derived from conjugated polymer solutions is paramount to enabling a printable electronics manufacturing environment. While this work utilized processing methods to self-assemble nanofibrillar aggregates, the conclusions obtained on retaining solubility to form percolative pathways during thin film deposition can be generalized to include non-self-assembling polymers. Here, a consistent mechanism that links the role of molecular weight to the level of aggregation in solution (process) and alignment of resultant nanofibrillar aggregates in thin films (structure) with charge carrier mobility (property) has been presented. Notably, similar structures and properties can be achieved with formulations comprising a single synthetic batch of polymer or blends of batches with notably different molecular weights to create samples with similar average molecular weight but different molecular weight distribution. This characteristic presents a realistic path to achieving manufacturable, low-cost semiconducting polymer ink formulations having reliable and reproducible performance attributes, obviating the need for precision, large-scale polymer synthesis on a commercial scale.

CHAPTER 4. CONTROL OF NUCELATION DENSITY IN CONJUGATED POLYMERS VIA SEED NUCLEATION

4.1 Introduction

Conjugated polymers are typically semi-crystalline resulting in a distribution of crystalline states and morphologies in the solid state depending on both the solution and thin film processing history. Macroscopic charge transport properties are thus governed by the assortment of interconnected pathways between highly conductive crystalline domains and less conductive amorphous regions. A myriad of studies has revealed microstructural features that influence charge transport including i) electron delocalization arising from ordered crystalline domains, ii) the formation of percolative charge transport pathways between crystalline domains, and iii) alignment of the crystallographic direction relative to the active channel. Developing processing techniques to understand and control the dynamic and complex crystallization processes in solution and during thin film formation to target specific structures is necessary to enable large scale, low cost printing of organic devices.

Advances in processing strategies to achieve controlled manipulation of the morphology can be divided into three categories: 1) solution preprocessing, 2) controlled deposition methods, and 3) solid state post preprocessing. Poly(3-hexylthiophene) (P3HT) has emerged as a workhorse system to study these complex process-structure-property relationships in polymeric semiconducting devices. Advances in solution preprocessing methods have enabled the repeatable formation of semicrystalline π-π stacked nanofibril

structures. Highly controlled crystallization methods including self-seeding via cooling-heating cycles and solvent quality manipulation[115-116] result in highly crystalline nanofibrils but are limited by their inability to form percolative charge transport networks. A variety of other preprocessing techniques including ultrasonication,[63] UV-irradiation,[66] and microfluidics[55] form semi-crystalline nanofibril domains that are interconnected via tie chains enabling percolative charge transport. However, these latter preprocessing methods lack control over the crystallization process as the manipulated variables are limited to only processing time. For example, in the case of UV-irradiation processing is limited to irradiation time. The ability to more precisely influence the crystallization process could aid in the reduction of grain boundaries that limits percolative charge transport.

Controlled deposition techniques promise the ability to manipulate polymer crystallization by promoting long-range alignment between semicrystalline domains to reduce grain boundaries. Deposition of polymeric solutions has progressed from spin-coating techniques to shear-coating methodologies that allow tuning of the time scale of solvent evaporation and/or chain planarization to promote self-assembly.[56, 108, 117] Zone casting,[118] doctor blading,[50, 119] and template guided shear coating[120-121] have all been shown to enhance alignment and thereby to increase the electrical performance of organic field effect transistors. However, these approaches require complex equipment and/or procedures to prepattern substrates and the blade and still result in the formation of significant grain boundaries. As an alternative approach, combined solution processing and controlled deposition protocols have been investigated to initialize the crystallization process in solution before being completed during film formation.[122] Kim *et al.* proposed a general approach of shear-coating pre-aggregated polymer solutions using an off-center

spin coating procedure to manipulate the crystallization process.[123] They observed enhanced charge carrier mobilities and mobility anisotropy using this approach with poly[(E)-1,2-(3,3'-dioctadecyl-2,2'-dithienyl)ethylene-alt-dithieno-(3,2-b:2', 3'-d)thiophene] (P18), and diketopyrroleopryrolethieno[3,2-b]thiophene (DPPT-TT). Similarly, Chang *et al.* studied the use of preformed one-dimensional nanofibers in solution prior to a simple blade coating deposition method.[56] Improvements in charge mobility were demonstrated using both P3HT and poly(3-butylthiophene) (P3BT), compared with spin coated nanofibers and blade coated pristine solutions. The importance of forming pre-aggregated polymer solutions before controlled deposition continues to be an active area of research with recent reports showing improved electrical performance using P(NDI2OD-T2)[124] and PDPPDCBT.[125] However, strategies to develop these nanofibers still rely upon temperature-controlled crystallization or solvent quality induced assembly limiting their implementation on an industrial-scale with continuous device fabrication. Facile processing methods to manipulate the nucleation process in the solution phase to enable *in situ* structural control remain elusive.

Herein, we demonstrate a facile blending approach to control the self-assembly of P3HT chains into interconnected polymer structures via seed nucleation. Polymer solutions were pretreated with low-dose ultraviolet (UV) irradiation to induce nucleation into nanofibrillar structures, which has been previously demonstrated in the literature[50]. These crystalline nanofibrillar structures serve as seeds. The nucleated P3HT samples were blended with amorphous, non-nucleated counterparts in different blend ratios to tailor the relative amount of seeds versus free chains. These solutions were subsequently aged to drive further growth and self-assembly into an interconnected network composed of

crystalline regions connected by tie chains. Enhanced aggregation of UV-irradiated P3HT solutions was driven by time-dependent self-assembly (solution aging).[50, 126] The role of varying the nucleation seed density on structure and corresponding charge transport was studied in both a batch system and continuous flow approach. Further, the impact of the formed P3HT networks on charge transport was characterized via organic field-effect transistor (OFET) device measurements. Analysis of the UV-vis solution and thin-film absorption spectra, small-angle X-ray scattering (SAXS), wide-angle X-ray scattering (WAXS), and atomic force microscopic (AFM) and polarized optical microscopic (POM) images informed mechanistic understanding of the relationships between nucleation seed density, structure of formed networks, and charge transport. Overall, blending of nucleated and non-nucleated polymer solutions was demonstrated to be a viable approach to control the growth rate of interconnected networks, an essential characteristic of robust, continuous large-scale processing.

4.2 Results and Discussion

4.2.1 Mobility Dependence on Seed and Amorphous Chain Molecular Weight

Two P3HT samples having different molecular weights (Mw) and polydispersity index (PDI) values (Table 1) were evaluated to investigate ideal polymer characteristics of the nucleated samples (seeds) and amorphous samples (tie chains). The investigated combinations of molecular weights are highlighted in **Table 5**. **Figure 28** illustrates the process to produce seed nucleated samples by treating one solution with 8 min of UV irradiation (nucleated: UV) followed by blending with an untreated sample (amorphous: AM). Blend ratios of 20%, 50%, and 80% by volume were subsequently aged up to 48

hours and deposited via blade-coating onto field-effect transistors for AFM and electrical analysis.[126] Notably, the blade-coating direction is parallel to the source and drain electrode to produce uniaxially aligned nanofibers per prior reports in the literature.[50]

Table 5: Sample acronyms and corresponding molecular weights of nucleated and amorphous components.

Sample Name	Nucleated M_w (kDa)	Amorphous M_w (kDa)
UV37:AM95	37	95
UV95:AM37	95	37
UV95:AM95	95	95

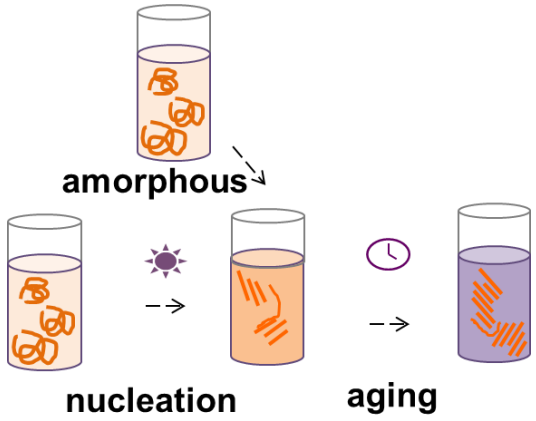

Figure 28: Solution blending procedure of blending pre-nucleated seeds formed via UV-irradiation with amorphous chains followed by solution aging.

Variations in the nanofibril morphology probed via AFM analysis can help elucidate relationships between polymer network formations and molecular weights of the seed and tie chain polymers. Immediately after UV-irradiation and blending, only the UV95:AM95 sample displayed discernable features, but only with the 80% nucleated sample. Notably, this does not indicate that nanofibers were not present, but rather they

were not found at the P3HT-air interface. All samples investigated exhibited nanofibril morphologies after 48 hours of solution aging (**Figure 29**).

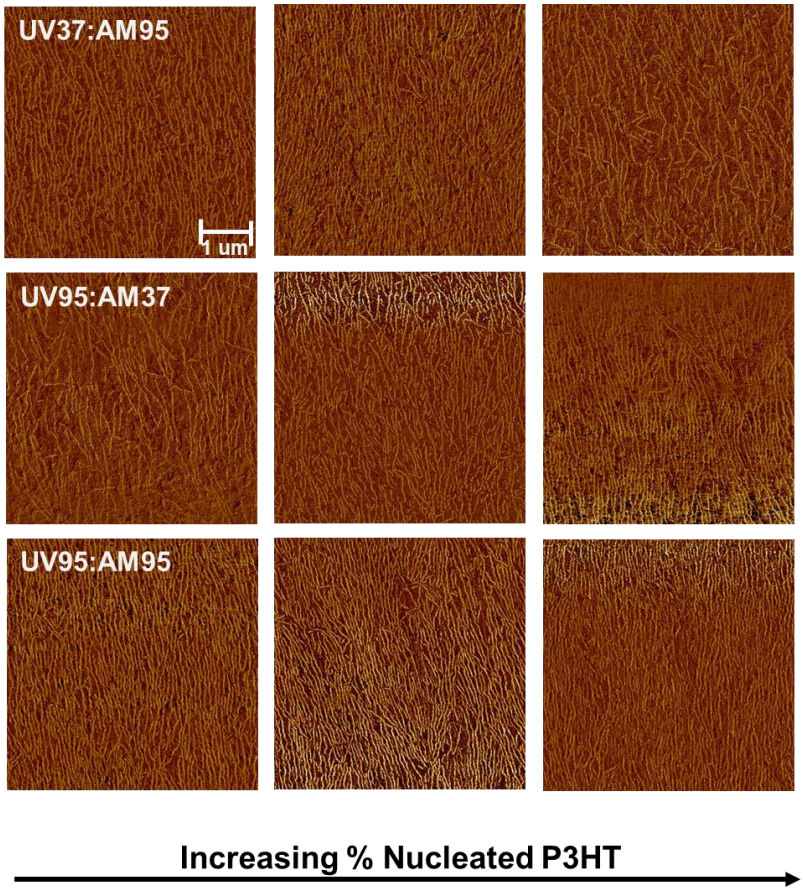

Figure 29: AFM images of P3HT-air interface after 48 hours of solution aging.

Recent advances in AFM image processing has enabled quantification of alignment and packing density of nanofibril structures to help elucidate relationships between processing and structures.[70, 108] **Figure 30** shows the AFM images of the UV37:AM 95 and UV95:AM37 samples after image processing. These images suggest that enhanced alignment occurs when high molecular weight chains are free in solution to form tie chains between seed crystals. Inclusion of a higher percentage of 37 kDa P3HT regardless if it was nucleated or not (ie UV37:AM95 or UV95:AM37) resulted in less densely packed and

more isotropic fibers and *vis versa*. In contrast, the UV95:AM95 sample exhibited densely packed and highly aligned morphologies, independent of the volume fraction of nucleated P3HT. Morphologically the improved alignment and packing density suggests that larger interconnected networks are formed when both seeds and tie chains are comprised of higher molecular weight P3HT.

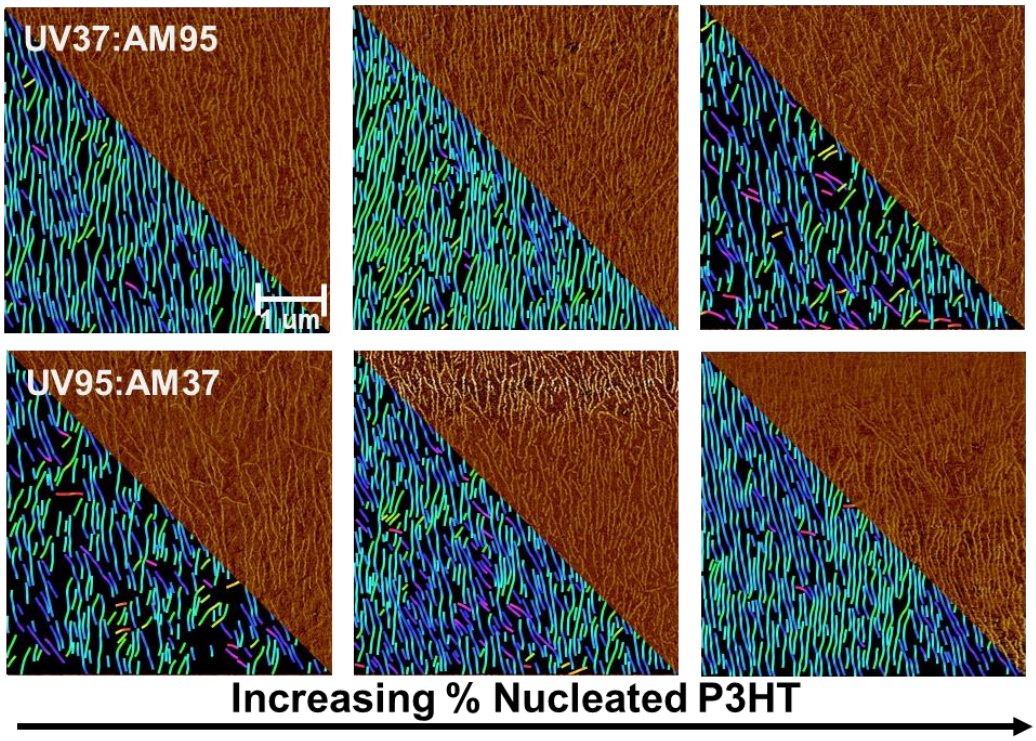

Figure 30: AFM images and corresponding imaged-processed results for the UV37:AM 95 (top) and UV95:AM37 (bottom) as a function of increasing percent seed nucleation.

A similar conclusion can be drawn when evaluating the percolative charge transport properties from OFET analysis. **Figure 31a** depicts the charge carrier mobility (μ) for all three samples as a function of aging time and volume percent of nucleated P3HT. Immediately after mixing the seed and tie chains solutions (0 hrs), an increase in μ with an increase in the percent of nucleated P3HT was observed for all samples. Similarly, solution

aging increased charge mobility in all cases. Combined, these indicate a nucleation and growth mechanism via seed nucleation induced crystallization as the seeds provide few potential pathways for charge transport at 0 hrs, followed by improved interconnectivity from additional crystallization with solution aging. Notably, the UV95:AM95 sample exhibited the highest charge mobility after 48 hours of solution aging with average values exceeding 0.18 cm^2/V-s, independent of the nucleation volume fraction. In contrast both the UV37:AM95 and UV95:AM37 exhibit a positive correlation between charge mobility and percent of nucleated P3HT. These results suggest synergistic enhancements when high molecular weights polymers are employed as both seed nuclei and tie chains which can be attributed to the improved formation of an interconnected percolative network in the solid state.

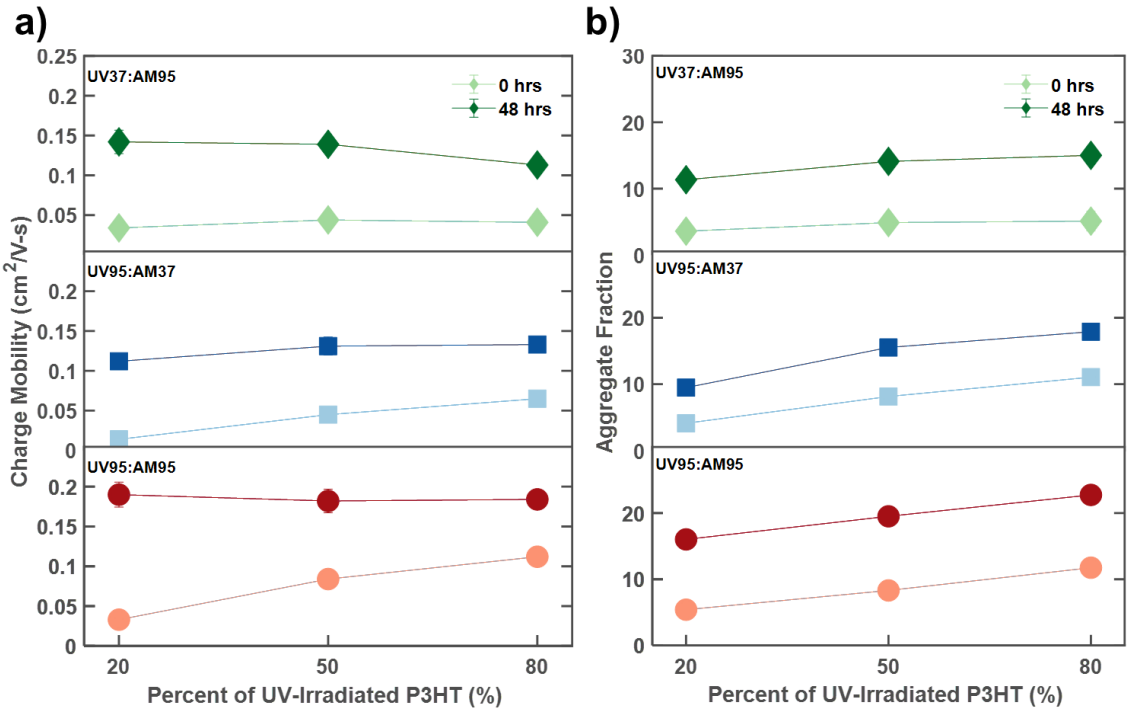

Figure 31: a) Charge mobility and b) solution aggregate fraction as a function of seed and amorphous molecular weight and volume percent of seeds.

Examination of the solution UV-vis absorption spectroscopy can help elucidate the role of solution self-assembly on the final thin film properties. Immediately after solution preprocessing, both samples comprised of 95 kDa P3HT seeds display similar aggregation behavior, independent of the amorphous polymer Mw, as shown in **Figure 31b**. At this time point, the addition of the amorphous solution does not impact the solution self-assembly but does influence the final film properties as seen in the charge mobility curves (**Figure 31a**). The addition of the amorphous 95 kDa solution results in higher charge mobility compared to the 37 kDa P3HT solution, suggesting improved interconnectivity between the seeds with higher Mw chains during the deposition process. Furthermore, upon solution aging, the UV95:AM95 sample exhibits more aggregation compared to the UV95:AM37 sample, indicating enhanced time-dependent aggregation in solution with higher Mw chains that transfers during the film deposition. This likely arises due the reduced solubility of higher molecular chains in solution.[126] Finally, the decreasing electrical performance of the UV37:AM95 samples at 48 hrs likely arises from the formation of grain boundaries beginning at the mixing of the nucleated and amorphous samples (0 hrs). The low aggregate fractions at 0 hrs, even at a nucleated volume fraction of 80%, demonstrates that low molecular polymers do not readily form seed crystals due to their high solubility. While solution aging with amorphous 95 kDa P3HT does result in large aggregates as shown via AFM (**Figure 30**), this likely arises from solubility driven self-assembly of the higher molecular chains, previously reported in the literature and in subsequent sections.

4.2.2 Mechanistic Understanding of Seed Nucleation via Controlled Self-Assembly

The observed tunability of both the solution and thin film properties makes the UV95:AM95 sample a prime candidate to elucidate the mechanism of self-assembly of interconnected polymer networks derived from seed nucleation. Blends with 0, 20, 50, 80 and 100% nucleated samples were blended with amorphous counterparts and subsequently characterized after aging in solution. **Figure 32** presents the evolution of the solution UV-vis absorption spectra of all nucleated samples as a function of aging time.

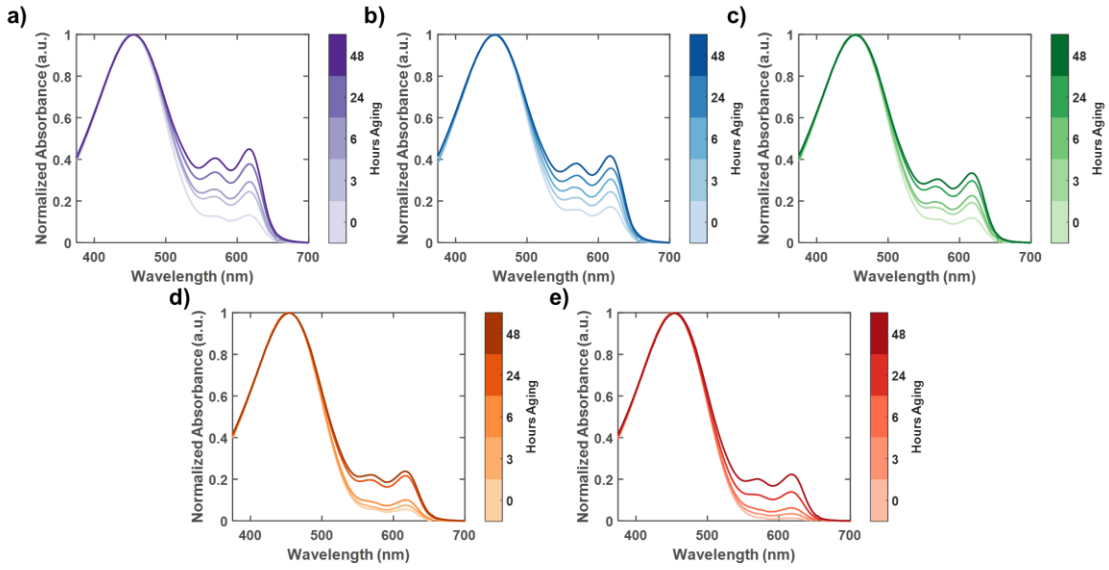

Figure 32: Solution UV-vis absorption spectra of a) 100%, b) 80%, c) 50%, d) 20%, and e) 0% nucleated P3HT.

To quantify the degree of aggregation in solution, the spectra were deconvoluted into amorphous and aggregated contributions. **Figure 33a** depicts the change in solution aggregation fraction as a function of volume percent of nucleated P3HT solution and aging time. Note that the aggregate fraction does not provide information on the absolute size or quantity of crystals but instead is a bulk measurement quantifying aggregation. Once again, an increase in aggregate fraction is observed with increases in aggregate fraction and aging

time, indicating a time-dependent seed crystallization self-assembly process. This crystallization process was modelled according to the Avrami equation to quantify the growth kinetics and dimensionality of growth. This equation is given by

$$\theta(t) = \theta_t - \theta_o = 1 - \exp(-(kt)^n) \tag{12}$$

where $\theta(t)$ is the crystallinity at time t, k is the growth rate constant and n is the Avrami exponent that describes the dimensionality of the growth process. As seed crystallization was modelled here, the contribution of aggregation from the seeds (θ_o) was subtracted from the recorded crystallinity at each time point (θ_t).

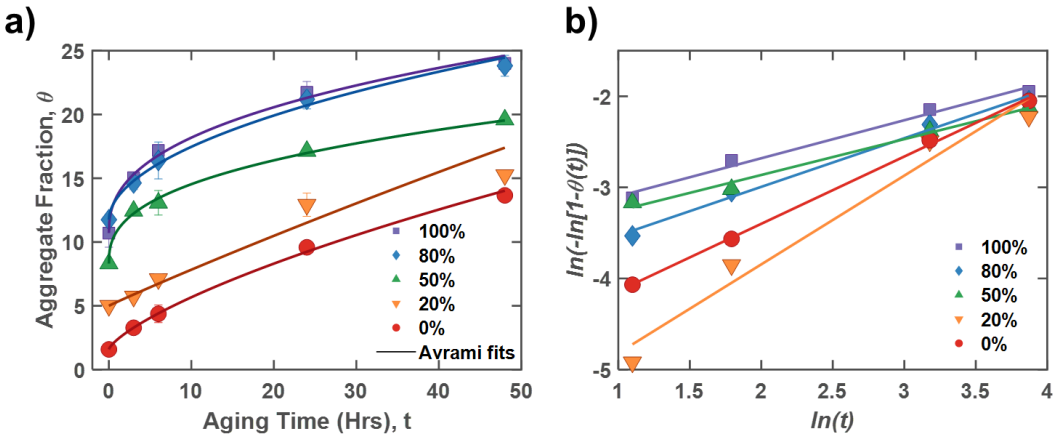

Figure 33: a) Aggregate fraction as a function of seed percent and aging time from deconvolution of UV-vis absorption spectra and b) Sharp-Hancock plots to extract n and k from the slope and intercept, respectively.

The modeled data is generally in good agreement with **Equation 12** as shown in the Sharp-Hancock plots in **Figure 33b** with the extracted growth rate and Avrami exponent values tabulated in **Table 6**. The low Avrami exponents (<1) are consistent with previous reports on polymer crystallization studies in which crystal growth is hindered through the partial incorporation of chains in neighboring crystals or an inability of chain

segments to diffuse away from the growth front.[127-128] Herein, two distinct crystallization processes are observed depending on the volume fraction of seeds. A higher value of *k* and lower *n* are observed with higher volume fractions of seeded P3HT (>50%) and *vice versa*. This suggests that while a large seed ratio results in faster growth of aggregated domains, the growth process is heavily influenced by the transport of chains to the growth front. In contrast, with a low seed ratio the slower crystallization process allows chains to successfully locate and crystallize at the growth front. Structurally, this should result in a mixed crystalline-amorphous motif of aggregates connected via tie chains with a high seed ratio compared to 1D nanofibril structures with a low seed ratio. Note that the 20% nucleated sample exhibits a significantly higher root mean squared error (0.199).

Table 6: Growth constants extracted from linear fits of the Avrami equation.

Percent Nucleated P3HT (%)	k (hrs^{-1})	n	RMSE
100	0.230	0.420	0.053
80	0.110	0.534	0.057
50	0.240	0.393	0.046
20	0.003	0.974	0.199
0	0.030	0.738	0.029

UV-vis absorption spectroscopy of the thin films indicate that the structures formed in solution survived the deposition process. The spectrum demonstrated distinct dependence on both the seed volume fraction and solution aging time (**Figure 34**). The exciton bandwidth (W) was extracted from these spectra to describe the degree of

intrachain order according to Spano's model.[76, 129] A low *W* corresponds to a long conjugation length and high intramolecular order, and *vis versa*. Again, a time-dependent decrease in the exciton bandwidth was observed for all seed ratios as shown in **Figure 36a**. Moreover, lower *W* values are observed as the volume percent of nucleated P3HT increases, in agreement with the Avrami analysis. The decrease in exciton bandwidths from over 75 meV immediately after mixing to *W* values under 50 meV for all samples except the 0% nucleated sample suggests the growth of interconnected tie chain between aggregates from a high degree of intrachain order. In contrast, in the absence of seeds, the exciton bandwidth does not decrease below 70 meV, consistent with the formation of isolated 1D nanofibers.

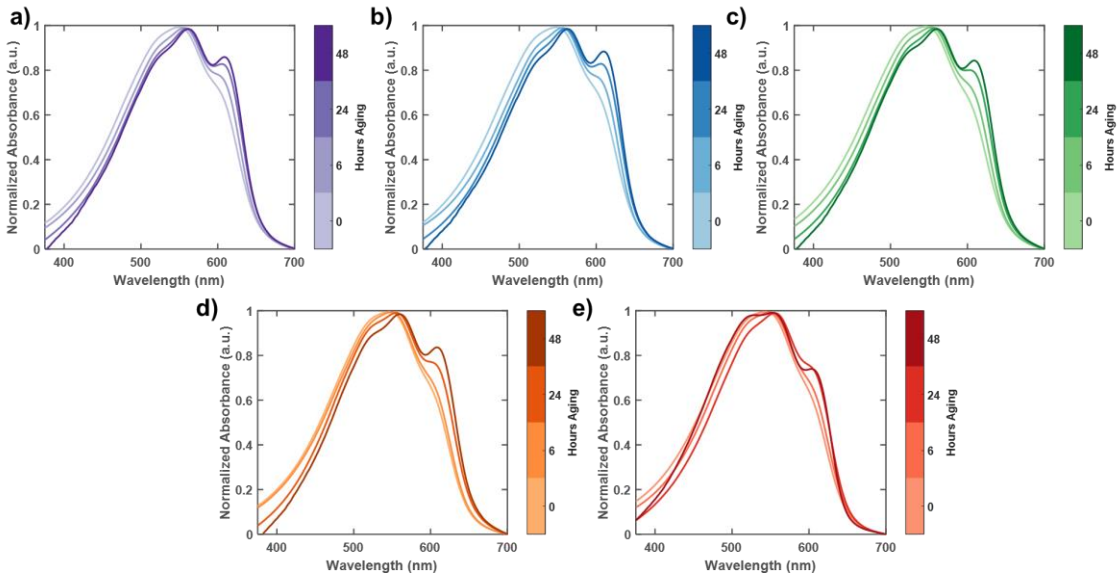

Figure 34: Thin film UV-vis absorption spectra of a) 100%, b) 80%, c) 50%, d) 20%, and e) 0% nucleated P3HT.

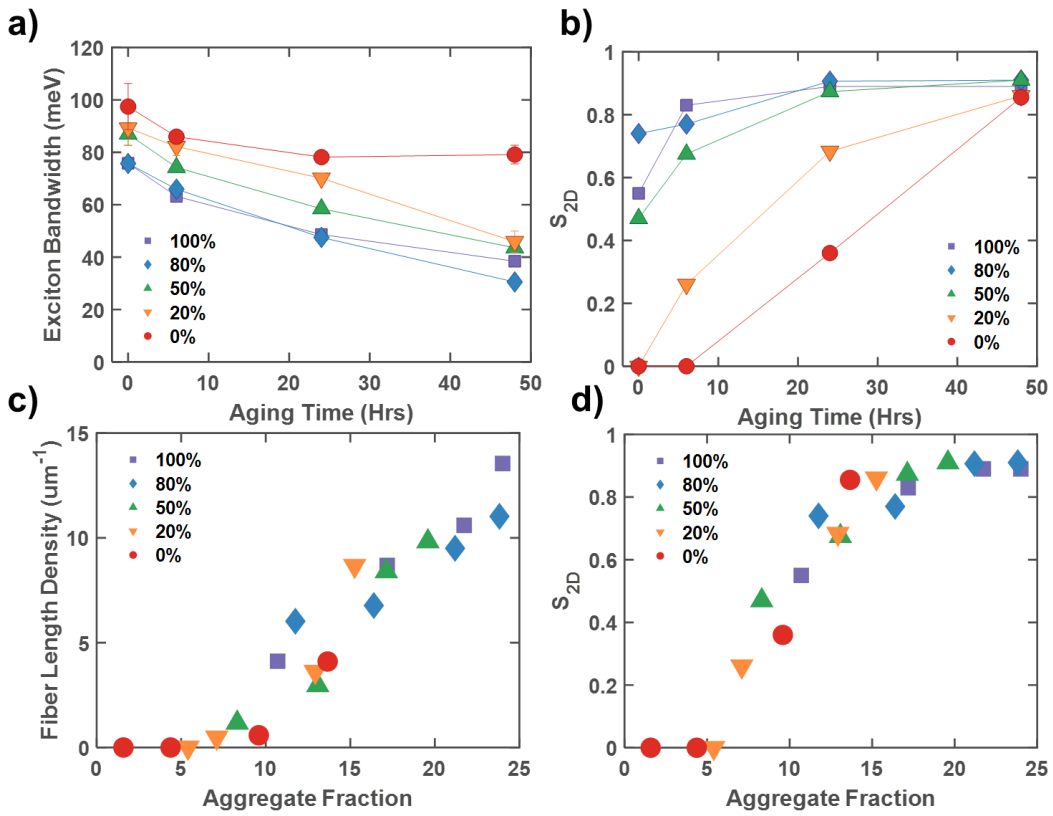

Figure 35: a) Thin film exciton bandwidth and b) S_{2D} as a function of seed volume fraction and solution aging time. c) Positive correlation between fiber length density extracted from AFM analysis and aggregation fraction extracted from solution UV-vis analysis. d) Positive correlation between orientational order extracted from AFM analysis and aggregation fraction extracted from solution UV-vis analysis.

The degree of alignment across multiple length scales has been presented as a proxy for polymer network interconnectivity. **Figure 36** depicts representative AFM images after 24 hours of solution aging in which a clear increase in orientation and fiber packing density (ρ_{FL}) with an increase in the percent of nucleated P3HT can be observed. The S_{2D} and ρ_{FL} values calculated for each image are in good agreement with the solution UV-Vis and Avrami analysis. A clear distinction can be observed between samples with a percent of nucleated P3HT above 50%, which exhibit an S_{2D} greater than 0.4 with 0 hrs of aging before plateauing at 0.9 after 24 hours aging, compared to samples below 20% that exhibit no alignment at 0 hrs and require at least 48 hours reaching maximum alignment (**Figure**

36b). Combined with the Avrami analysis, these S_{2D} results suggest that the degree of orientational order is likely a strong proxy to quantify the degree of polymer assembly interconnectivity. Samples with a higher S_{2D} experience enhanced interconnectivity. Furthermore, both the packing density of fibers and orientational order are strongly correlated with the aggregate fraction across all samples observed in solution as shown in **Figure 35c and d**. A direct and robust correlation between solution characteristics and film structures has been a long-desired goal in solution processed organic electronics to enable *in-situ* control and monitoring of the solution phase for industrially relevant processing. The results herein suggest that the UV-vis solution aggregate fraction could serve as this metric.

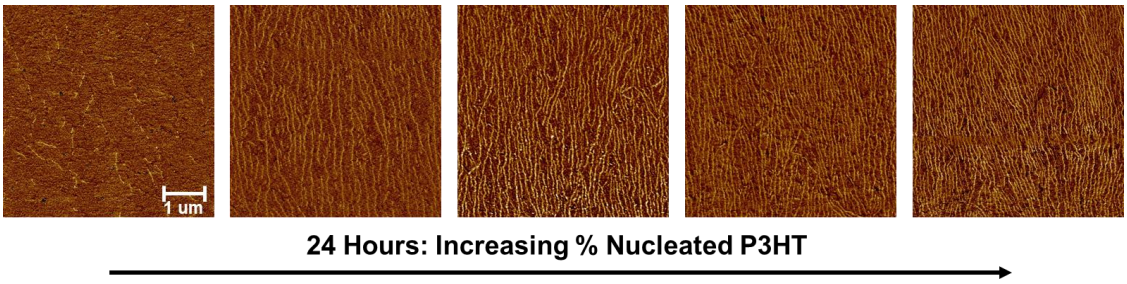

Figure 36: AFM images of all samples after 24 hours of solution aging with increasing nucleated P3HT from 0 to 100%.

A high degree of alignment was seen beyond the mesoscale using POM and linear polarized UV-vis absorbance. Alignment quantified by normalizing the intensity of POM images and the dichroic ratio extracted from polarized UV-vis analysis, as shown in **Figure 37**, exhibited similar trends as the AFM analysis. This suggests that orientational order found at the meso scale also exists on the macro scale. This trend is generally seen across all samples except in the 100% seed nucleated sample. In this sample, the macroscale order, as probed via POM images and the dichroic ratio decreases after 24 hours aging. This could

arise from the formation of aggregates that are too large to effectively align upon deposition, resulting in lower orientational alignment as discussed in **Chapter 2**.

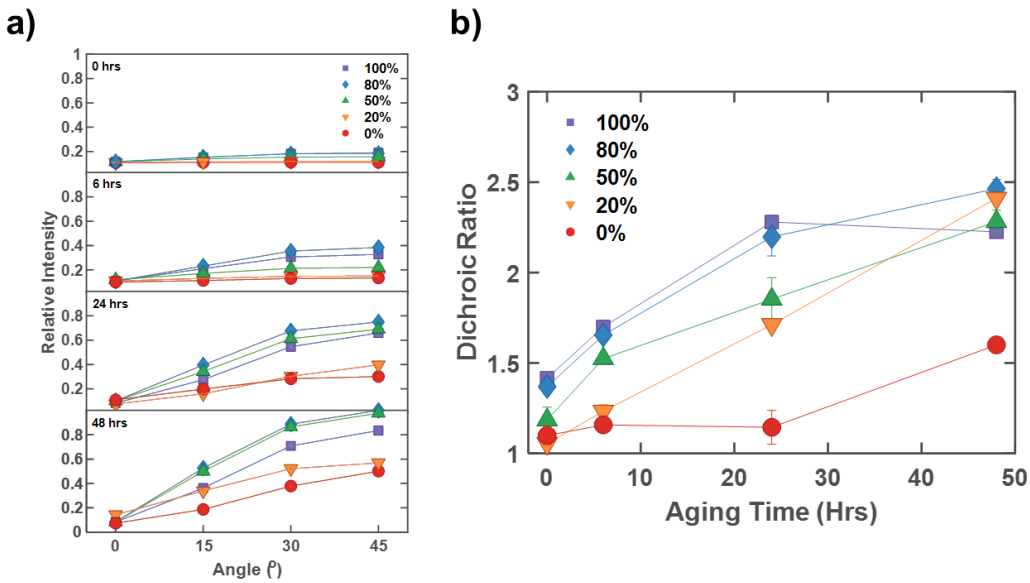

Figure 37: a) Relative intensity extracted from POM images and b) dichroic ratio as a function of seed volume fraction and aging time

Both wide angle X-ray scattering (WAXS) and small angle X-ray scattering (SAXS) were utilized to probe the role of seed nucleation on the crystalline texture on the mesoscale. **Figure 38** shows the representative SAXS images from 24 hours of solution aging while **Figure 39** shows the corresponding WAXS images.

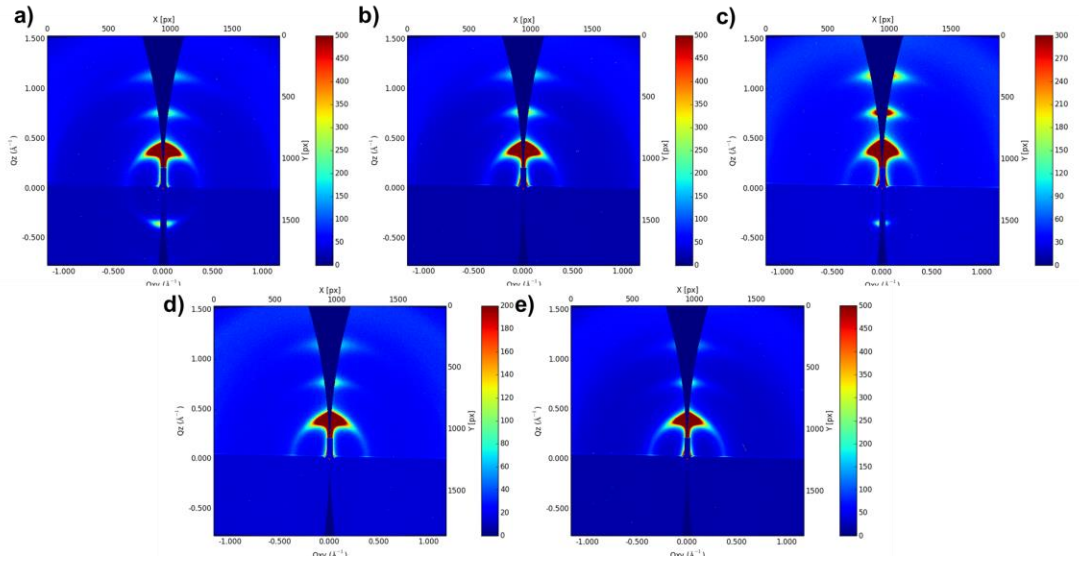

Figure 38: SAXS images of a) 100%, b) 80%, c) 50%, d) 20%, and e) 0% nucleated P3HT after 24 hours of solution aging.

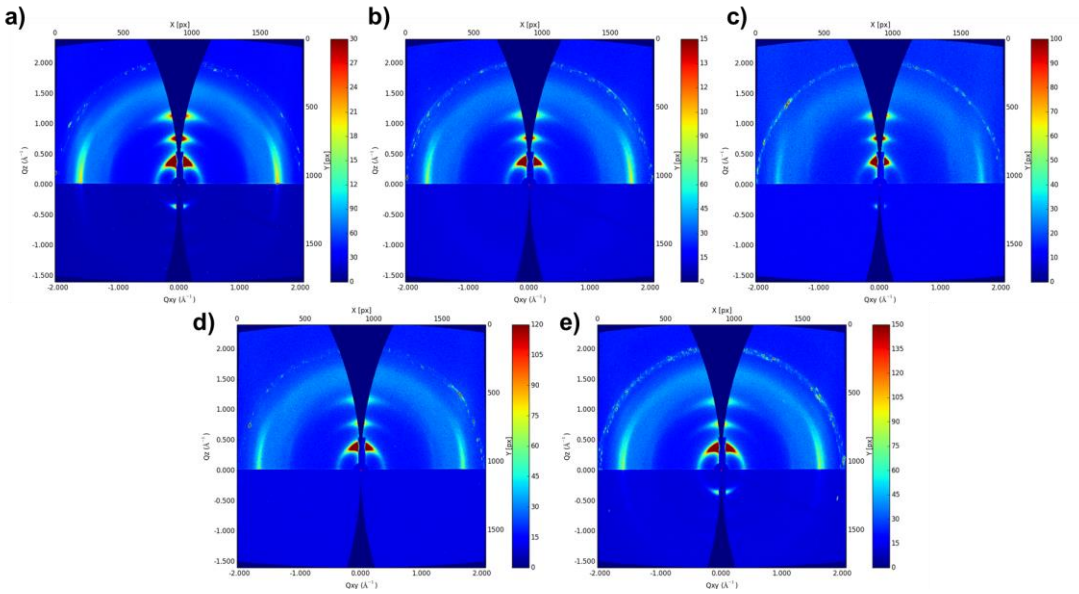

Figure 39: WAXS images of a) 100%, b) 80%, c) 50%, d) 20%, and e) 0% nucleated P3HT after 24 hours of solution aging.

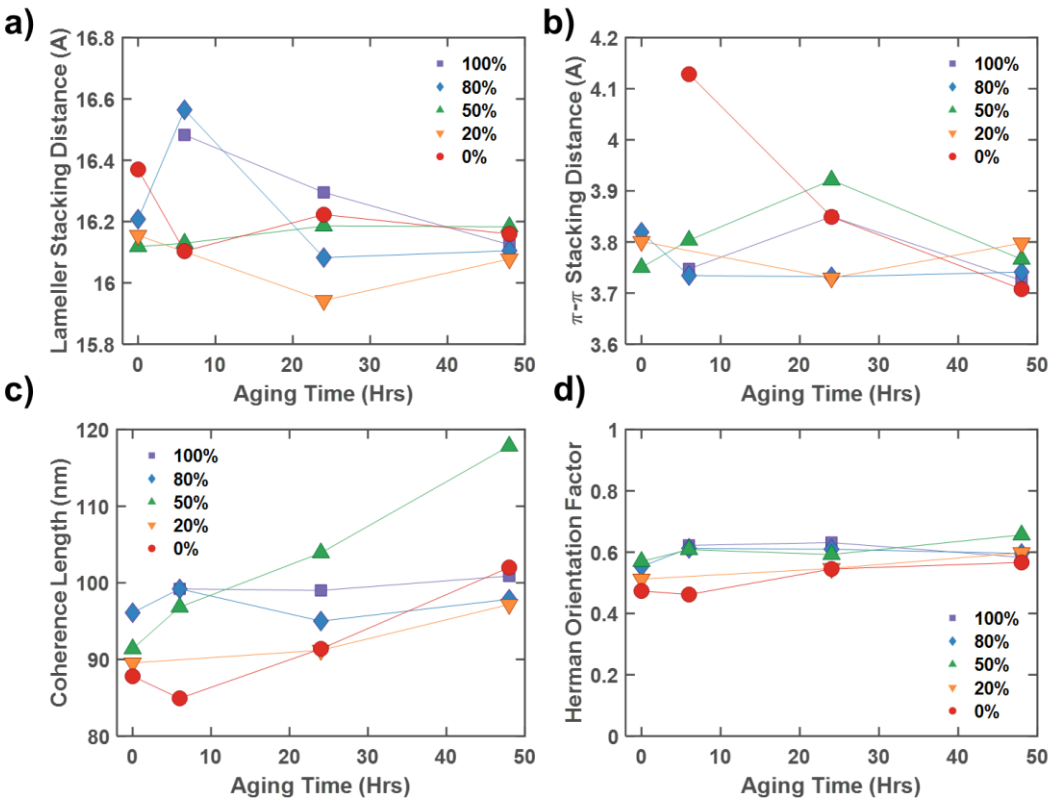

Figure 40: a) Lamellar stacking distance, b) π-stacking distance, c) coherence length, and d) Herman's orientation factor of thin film as a function of seed volume fraction and solution aging time.

Lamellar and π- π stacking distances were quantified from the (100) and (010) peaks, respectively. No observable trends relating the lamellar and π- π stacking distances to the seed nucleation percent or aging time were seen with values ranging between 15.9 and 16.6 Å and 3.7 and 4.1 Å respectively (**Figure 40a and b**). A dependence on the seed nucleation percent and aging time was observed in the coherence length along the (100) direction and Herman's Orientation Factor (**Figure 40c and d**). Once again, distinct differences between samples with a high seed nucleation percent (>50%) and those with a low (<20%) were exhibited. A generally higher coherence length (>90 nm) and Herman's orientation factor (>0.55) was observed with a high nucleation percent and *vice versa*. These results suggest, in agreement with the UV-vis and AFM analysis, that a higher

fraction of seed nuclei results in structures with a lower degree of paracrystalline disorder manifesting in increased local crystallinity and meso-and macroscale alignment. Notably, the 50% nucleated P3HT sample displays a linear increase in coherence length along the (100) direction with solution aging time from 91 nm at 0 hrs to 117 nm after 48 hours. This likely arises from an optimal balance of seed-induced growth in solution with the film formation process during blade-coating.

Ultimately, the structural features proposed through the prior characterization should manifest in differences in electrical properties. Electrical charge transport properties were characterized through OFET analysis of transistors operating in the saturation regime. All transfer curves displayed the typical features of p-channel OFETs operating in the accumulation mode. The extracted charge carrier mobility and threshold voltage results are presented in **Figure 41a and b.** Immediately after mixing the seed and amorphous samples (t = 0 hrs) charge transport is driven mainly by the presence of seeds as μ increased from $4x10^{-3}$ cm^2/V-s with 0% seeds to $1.2x10^{-1}$ cm^2/V-s with 100% seeds. Aging of the solutions results in a general increase in the measured charge transport properties. Notably, the 20% seed sample exhibits the largest enhancement in electrical properties, with an initial μ of $3.3x10^{-2}$ cm^2/V-s to mobility values exceeding $1.9\ x10^{-1}$ cm^2/V-s after 48 hours of solution aging. As suggested in the characterization discussion above, the increase in electrical performance arises due to the formation of structural motifs that are more conducive to transport. The results shown here indicate that samples comprised of 20%, 80%, and 50% P3HT seed volume fractions can effectively form interconnected polymers networks resulting in enhanced charge transport. In contrast, the 100% P3HT seed case rapidly forms an aggregated structure, but further aging results in the formation of grain boundaries that

disrupt charge transport. The 0% P3HT seed case is likely subjected to a nucleation and growth mechanism that promotes the formation of a small number of 1D nanowires. Notably, the degree of aggregation in the 0% P3HT seed case is similar to that of the 20% case (**Figure 33c**) so the main difference between these two samples is the relative number of nuclei. The 0% P3HT seed case lacks nuclei distributed throughout the medium resulting in the formation of grain boundaries that disrupt charge transport.

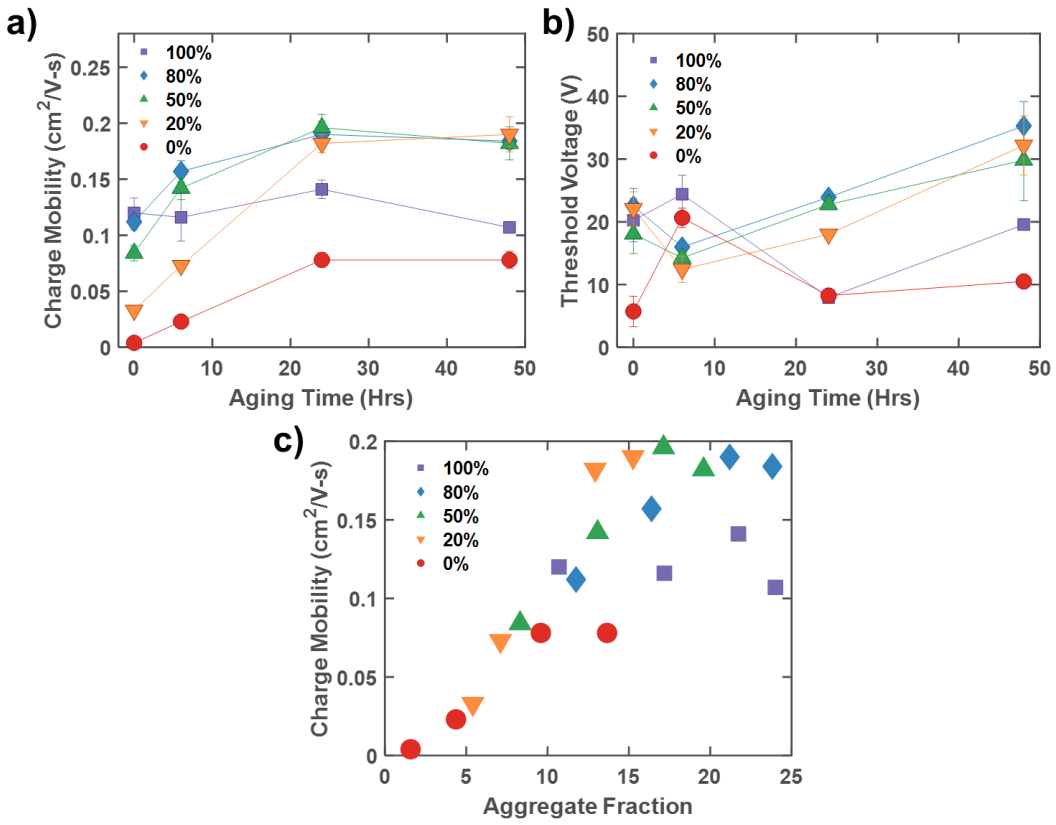

Figure 41: a) Charge carrier mobility and b) threshold voltage extracted from OFET analysis as a function of seed volume fraction and solution aging time. c) Positive correlation between charge mobility and solution aggregate fraction.

Overall, this study suggested that the nucleation and growth rate can be tuned by varying the volume fraction of P3HT seeds added to an amorphous sample with subsequent solution aging. By varying the seed volume fraction in solution, the mechanism of growth

has been shown to vary between 1D nanofibers in low seed volume fractions and interconnected polymer networks with high seed volume fractions. Notable the degree of aggregation in solution can be manipulated via the percent of seeds, suggesting the use of feedback control systems to precisely control process-structure relationships in large scale, industrial settings (**Figure 41c**). Furthermore, the ability to obtain similar μ values despite differences in the quantity of seeds indicates a robust processing method over 20-80% seeding.

4.2.3 Mechanistic Understanding of Seed Nucleation via Controlled Self-Assembly

As industrial-scale roll-to-roll printing of large area solution processable organic electronic devices continues to advance, morphological control must process from batch experiments into continuous flow systems. **Figure 42** illustrates the continuous flow microfluidic setup in which two polytetrafluorethylene (PTFE) tubes (Cole-Parmer Instrument Company) of inner diameter of 0.762 mm and length 3.35 m were connected to syringe pumps containing dissolved P3HT in chloroform. One of the tubes was exposed to UV light over a residence time of 15 seconds to form nucleated P3HT before mixing via a static mixer with a non-nucleated sample[55]. The mixture subsequently flowed through a recollection tube to promote nanofibrillar and polymer network growth. Blade coating onto OFET substrates and glass slides for characterization was completed approximately 5 minutes later to reduce the impact of aging affects.

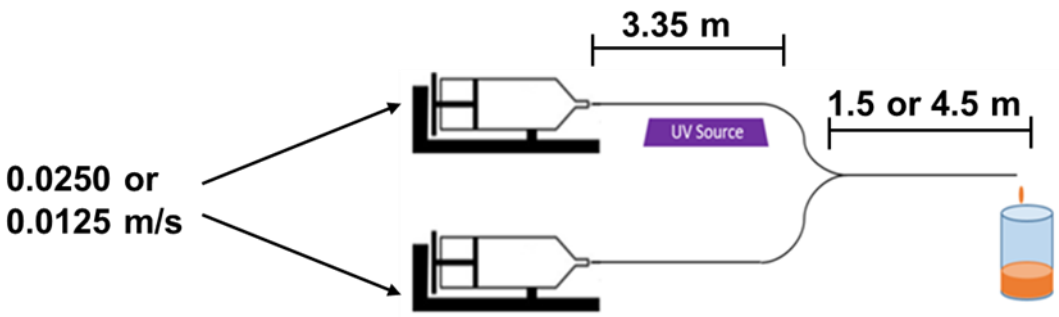

Figure 42: Continuous flow setup in which P3HT solutions are pumped through PTFE tubing before mixing in a static mixer. The UV-irradiation residence time is fixed at 15 seconds. The pump flow rate and tube length after mixing are the varied process parameters in this system.

A two-level, two-factor experimental design scheme was used to investigate the impact of flow rate and recollection tube length on P3HT self-assembly into ordered, interconnected fibrillar domains. The high and low levels for the flow rates were 0.025 ml/s and 0.0125 ml/s while the recollection tube length was either 1.5 m or 4.5 m. These settings are summarized in **Table 7.** To compare the results to the batch studies conducted in this study, the same molecular weight mixtures (UV37:AM95, UV95:AM37 and UV95:AM95) were used to screen for the impact of chain length on seed and amorphous chain properties.

Table 7: Continuous flow settings for the recollection tube length and flow rate.

Sample Name	Recollection Tube Length (m)	Flow Rate (ml/s)	Aging Time (s)
LL:LF	1.5	0.0125	27.4
HL:LF	4.5	0.0125	82.1
LL:HF	1.5	0.0250	13.7
HL:HF	4.5	0.0250	41.0

*Sample names: Low (L) and high (H) settings of tube length (L):flow rate (F)

*Eg LL:LF has low tube length and low flow rate settings

*All samples exposed to 15 s of UV-irradiation by changing tube length exposed to light

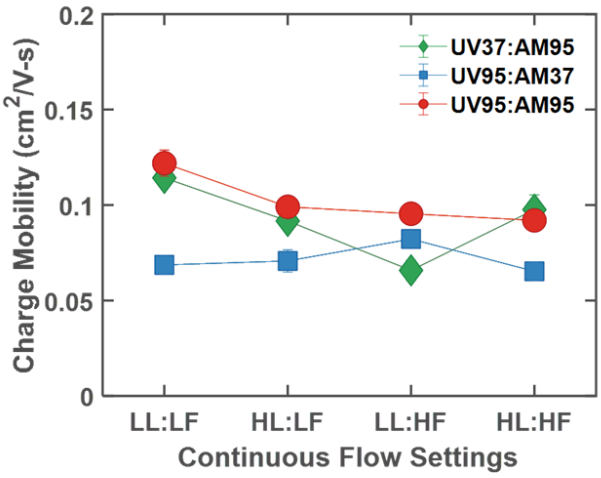

Figure 43: OFET charge mobility from the continuous flow system as a function of flow settings and molecular weights.

Figure 43 highlights the charge carrier mobility results as a function of sample (seed: amorphous ratio) and flow conditions. Generally higher charge carrier mobility values were observed for samples with a high amorphous P3HT MW (95 kDa) regardless of the MW of the P3HT seed, in agreement with the results obtained in the batch studies shown in **Figure 28**. The mobility values for these samples (UV37:AM95 and

UV95:AM95) exceed 0.09 cm^2/V-s, with the exception of the LL:HF sample flow condition. In contrast, UV95:AM37 with a low molecular weight as the amorphous sample, exhibited significantly lower mobility, ~0.07 cm^2/V-s. The differences in the mobility values likely arise from the degree of interconnectivity as reported in the batch discussions above. Notably, the mobility values observed in the continuous flow study are generally lower than the batch 48-hour aged results (**Figure 28**). This could arise due to "over-processing" of the continuous flow samples that requires further optimization or a distinct self-assembly mechanism.

UV-vis absorption spectra of the solution state depict distinct differences in the assembly behaviour in solution between continuous flow processing and batch processing. **Figure 44a** depicts the aggregate fractions obtained via continuous flow processing as a function of seed and amorphous molecular weights and flow processing conditions. Generally, higher flow rates result in larger aggregate fractions regardless of the molecular weights of the seeds and the tube length as seen in the LL:HF and HL:HF conditions with aggregate fractions exceeding 30% in these samples. This likely arises from the increased shear that helps to planarize individual chains to form aggregates.[55] The increased aggregate fraction of the UV95:AM95 (37%) sample at the HL:LF condition compared to the UV37:AM95 (27%) and UV95:AM37 (25%) is likely a combination of the decreased solubility of the longer chains and the longer residence in the tube systems.

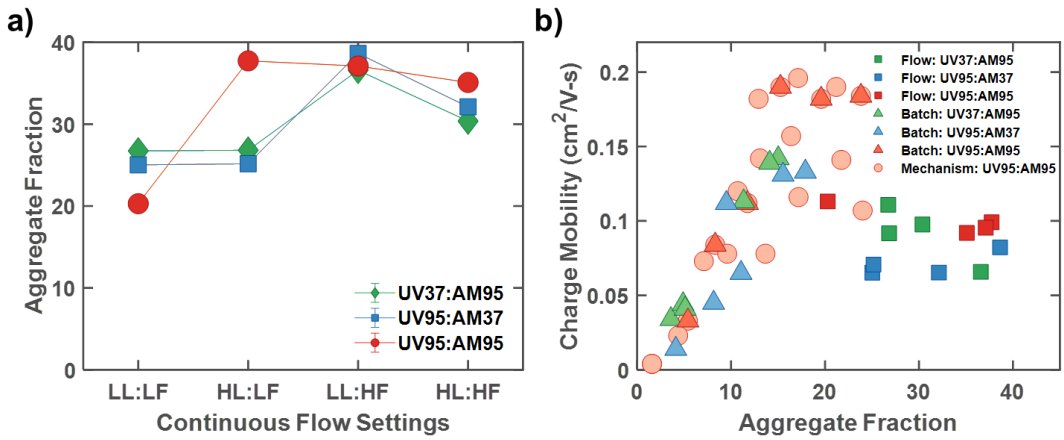

Figure 44: a) Aggregate fractions obtained via the continuous flow system as a function of molecular weight and flow settings and b) Correlations between aggregate fraction and charge mobility for all processing conditions conducted in this study.

Notably, the aggregate fractions obtained via the continuous flow system are substantially higher than their batch counterparts. This is shown in **Figure 44b** with the aggregate fraction and corresponding charge carrier mobility plotted as a function of processing conditions for all datapoints collected in this study. Note that the squares represent the continuous flow data presented in this section, the triangles are the batch data from **Section 4.2.1,** and light circles represent the data collected in the previous section, **Section 4.2.2**. A strong positive correlation between aggregate fraction and charge mobility exists for all batch processing as an increase in aggregate fraction results in enhanced charge transport. However, an increase in solution aggregate fraction obtained during continuous flow processing does not result in improved charge carrier mobility. This could arise from the combination of two effects 1) there exists a different mechanism of self-assembly in continuous flow processing compared to batch processing or 2) the continuous flow system has resulting in "over processing" to form large aggregates that limit charge transport through grain boundaries. Studies by Wang *et al.* have hypothesized the

formation of shish-kebab structures that differ structurally from interconnected nanostructures through examination of the structures obtained via AFM analysis.[55, 82]

Differences in the thin film morphology alignment and packing density can be seen via quantification of AFM images. **Figure 45a and c** depict the orientational alignment (S_{2D}) and fiber packing density from AFM images as a function of seed and amorphous chain molecular weight and continuous flow settings. The UV95:AM95 sample exhibits enhanced alignment and fiber packing density compared to the UV37:AM95 and UV95:AM37 samples but this does result in improved charge carrier mobility (**Figure 43**). Similarly, to the aggregate fraction analysis, devices fabricated from continuous flow processing cluster in distinct areas when plotted against charge carrier mobility (**Figure 45b and d**). The features that form during continuous flow processing are structurally different from those formed in batch processing.

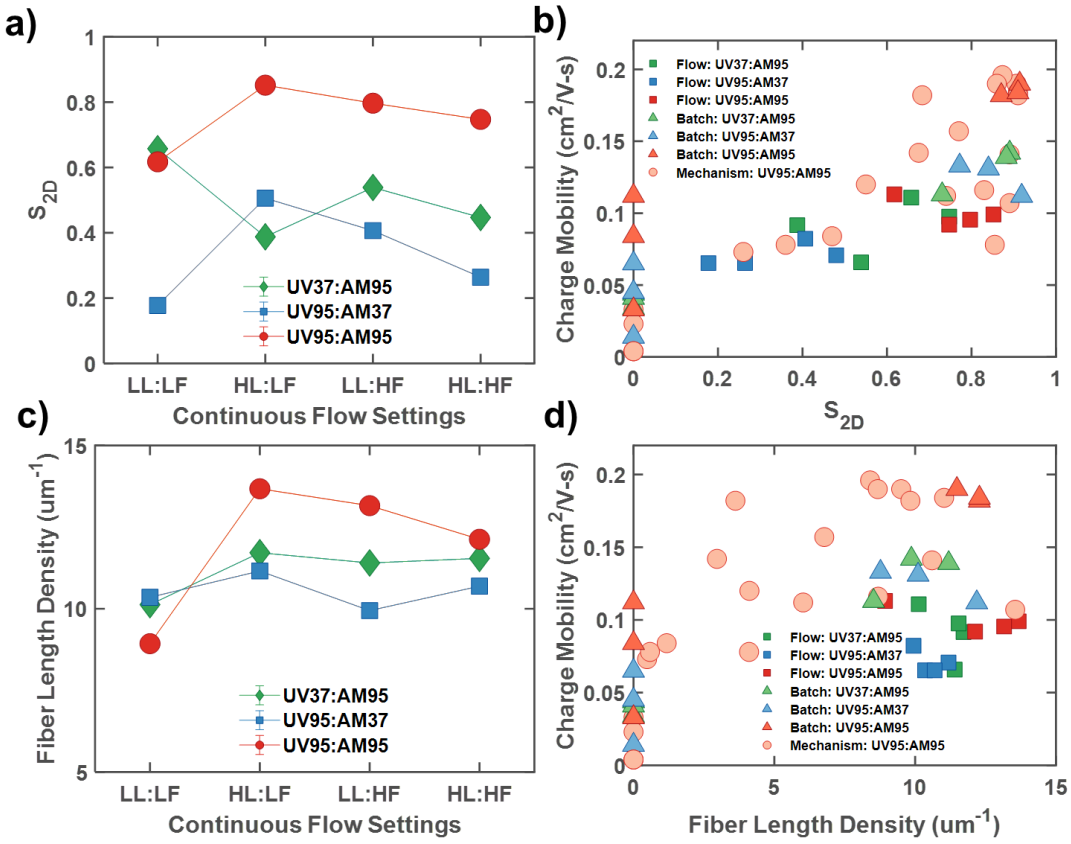

Figure 45: a) S_{2D} order parameters obtained via the continuous flow system as a function of molecular weight and flow settings. b) S_{2D} and charge mobility for all processing conditions conducted in this study. c) Fiber length density obtained via the continuous flow system as a function of molecular weight and flow settings. d) Fiber length density and charge mobility for all processing conditions conducted in this study.

In light of the report process-structure-property relationships reported herein, several key points of interest require discussion. Firstly, in this study, batch processing was shown to obtain higher electrical properties but requires the cost of additional processing time (solution aging). Furthermore, it is unknown if structures formed during batch processing can be subsequently flown through nozzles to enable desired roll-to-roll printing. In contrast, continuous flow process exhibited lower electrical properties in this study, but at the benefit of a more robust and facile processing method. This is not to state that continuous flow processing results in structures that are detrimental to percolative

charge transport but rather that subsequent optimization experiments exploring the impact of tube length or tube size need to be conducted. Secondly, the charge mobilities of all the samples (UV37:AM95, UV95:AM37 and UV95:AM95) are consistent regardless of the tube length or flow rate (**Figure 43)** compared to the dependence on aging time and seed volume fraction demonstrated in the batch studies. This suggests a more robust and consistent self-assembly process in continuous flow compared to batch processing. Overall, the quantification of process-structure-property relationships can help guide the transferability of processing methods from batch to continuous flow systems that may be required to enable industrial-scale solution printing of organic electronic devices.

4.3 Conclusions

The use of seed nucleation as a processing method in organic electronics enables precise control of the nucleation and growth rate in solution. Control over the growth of semicrystalline nanofibers is essential to the development of high-performance OFET devices. Supramolecular ordering and crystal alignment on both the meso- and macroscale was greatly enhanced through the addition of seed nuclei prior to solution aging. Herein, it was found that the molecular weight of both seed crystals and amorphous chains is a key processing parameter to enable the growth of interconnected polymer networks for percolative charge transport. Higher molecular weight chains can more effectively form seed nuclei due to the lower solubility of the long chains. Furthermore, higher molecular weights samples are better served as the amorphous component due to their ability to interconnect crystalline domains.

Strong correlations between the solution aggregate fraction and charge mobility values were observed in batch processing studies. This may enable feedback control systems that can be implemented to add more seeds or amorphous chains to maintain an ideal solution structure. It is likely that a similar approach can be adopted to further control the self-assembly in the continuous flow system once an optimal processing window is discovered that results in the formation of fewer aggregates (aggregate fraction <20%).

The results provided here underscore the importance of control over the formation of grain boundaries and interconnected networks for polymeric semiconductors. As such the results found in this study using P3HT should be generalizable to other self-assembling polymer systems such as PBTTT. Furthermore, it is expected that other methods to initially form seeds, such as solution aging or poor solvent addition, would be applicable to this approach. The systematic quantification of process-structure-property relationships is essential as the development of organic electronic processing methods transfer from lab scale curiosities to high volume manufacturing.

CHAPTER 5. A GENERAL APPRAOCH TO DEVELOP GLOBALLY INTERCONNECTED CONJUGATED POLYMERS VIA POOR SOLVENT MANIPULATION

5.1 Introduction

The complex role that the choice of solvent plays in the morphological evolution of conjugated polymers from the solution state into thin films, has been of key interest since the discovery of solution processable organic electronics.[30, 130-131] Understanding of the role of solvents on morphology has progressed from the use of binary solvents towards tuning the solvent quality through cosolvent addition. The selection of the good solvent, a solvent with energetically favorable interactions with the polymer, can reduce entanglements and promote chain elongation. The addition of a poor solvent that has unfavorable interactions with the polymer can enable self-assembly of aggregates as the chains reorganize to minimize unfavorable interactions in the solution phase[64]. Furthermore, the use of cosolvents with differing volatilities and surface tensions adds increased complexity to the formation of structures during thin film deposition processes. More recently, efforts to select solvents that are compatible with multiple components, for example elastomers with conjugated polymers to enable stretchable devices, have been investigated.[49] The potential to elucidate process-property relationships that generalize across multiple conjugated polymer systems makes the cosolvent approach a promising approach for large scale, industrial applications.

Although significant advances have been made towards demonstrating multi-solvent systems as an industrially relevant processing technique, several challenges remain. The mechanism of poor solvent driven-assembly relies upon minimizing unfavorable interactions between polymers and poor solvents. This mechanism has been hypothesized to form nanofibers with enhanced intramolecular ordering but limited intermolecular connectivity; fringe chains that could potential form tie chains are instead retracted due to the poor solvent[108]. Processing methods to promote the formation of interconnected polymer networks through manipulation of the cosolvents are required for enhanced charge transport. Furthermore, elucidating the relationship between cosolvent selection and time-dependent self-assembly is essential for the formulation of reliable and robust ink formulations. The role of time-dependent self-assembly has been previously demonstrated to enhance charge transport properties in binary solvent systems but has not yet been applied to cosolvent systems.

Herein, we propose a general blending approach to optimize interconnected polymer networks by controlling the volume fraction and time-dependent self-assembly using cosolvent addition. This approach was demonstrated using the conjugated polymer poly(3-hexylthiophene) (P3HT) dissolved in chloroform with 2-methylpentane (2-MP) as the poor solvent. The role of time-dependent self-assembly was investigated by 1) adding poor solvent followed by solution aging, 2) solution aging followed by poor solvent addition and 3) comparing to a control sample without poor solvent. Analysis of the solution and film UV-vis absorption spectra, small-angle X-ray scattering (SAXS), wide-angle X-ray scattering (WAXS), and atomic force microscopic (AFM) and polarized optical microscopic (POM) images were used to elucidate the mechanism of self-assembly

in cosolvent-driven self-assembly. It was found that aging a polymer solution prior to poor solvent addition forms an interconnecting polymer network with enhanced charge transport properties as characterized via organic field-effect transistor (OFET) device measurements. Time dependent self-assembly was also observed in poly[2,5-bis(3-tetradecylthiophen-2-yl)thieno[3,2-*b*]thiophene] (PBTTT) demonstrating the generalizability of the approach.

5.2 Methods

Consistent with the other studies in this thesis, a constant concentration of 5 mg/ml of P3HT in chloroform was used. P3HT was dissolved in $CHCl_3$ at 55°C for 20 minutes and subsequently cooled to room temperature for 15 minutes. In the Age:Poor sample, P3HT was withdrawn from this stock solution at times of 0, 6, 24, and 48 hours and added to 4 ml borosilicate vials followed by the addition of 20% by volume of 2-methylpentane (2-MP) to each sample. The vials were then stirred at 300 RPM for 5 minutes to ensure homogeneous mixing of the good and poor solvents. Device and structural characterization were then conducted according to the procedures outline in **Chapter 2**. In the Poor:Age sample, 20% of 2-MP was added to the cooled stock solution and stirred at 300 RPM for 5 minutes. Device and structural characterization were then conducted immediately (0 hrs) and at 6, 24, and 48 hours. Finally, the Age sample served as the control without poor solvent. All samples were stored in ambient conditions in the dark. These processing methods are illustrated in **Figure 46**.

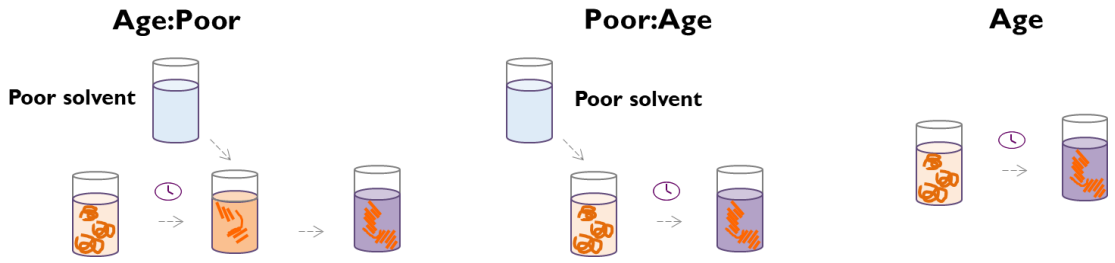

Figure 46: Illustration of investigated processing methods to investigate role of poor solvent addition and time-dependent self-assembly.

5.3 Results and Discussion

5.3.1 Mechanistic Understanding of Self-Assembly using P3HT

5.3.1.1 Solution UV-Vis Characterization

Solution UV-vis absorption was used to characterize the degree of self-assembly in solution. The absorption spectra of the three investigated cases termed Age:Poor, Poor:Age, and Age are shown in **Figure 47**. The broad peak centered at ca. 455 nm corresponds to isotropic chains with random degrees of conjugation. The addition of poor solvent, in the Age:Poor and Poor:age samples results in the development of shoulder peaks at ca. 615 nm (0-0) and 570 nm (0-1). These peaks arise from the increase in conjugation length as chains planarize and self-assemble in nanofibril aggregates. The UV-vis absorption spectra can be deconvoluted into aggregate and amorphous contributions by fitting the vibrionic peaks to Frank-Condon progressions. **Figure 47d** depicts the extracted aggregate fractions of the three samples as a function of solution aging time. The solution without poor solvent and relies purely on time-dependent self-assembly displays an increase in the aggregate fraction from 2% at time 0 to 14% after 48 hours of solution aging. In contrast, the Age:Poor and Poor:Age samples display a small increase in aggregate fraction upon addition of the poor solvent (9%) before a large increase to ca.

35% after 6 hours of aging regardless of the order of processing. Notably, after 6 hours of solution aging the time of poor solvent addition does not impact the aggregate fraction of the Age:Poor sample. In contrast, the Poor:Age sample continues to follow time-dependent self-assembly. As the composition of the Poor:Age and Age:Poor samples are identical and only differ by the order of processing, similar solution aggregation behavior is expected; the aggregate fraction only informs the degree of aggregation and not the size or quantity of aggregated.

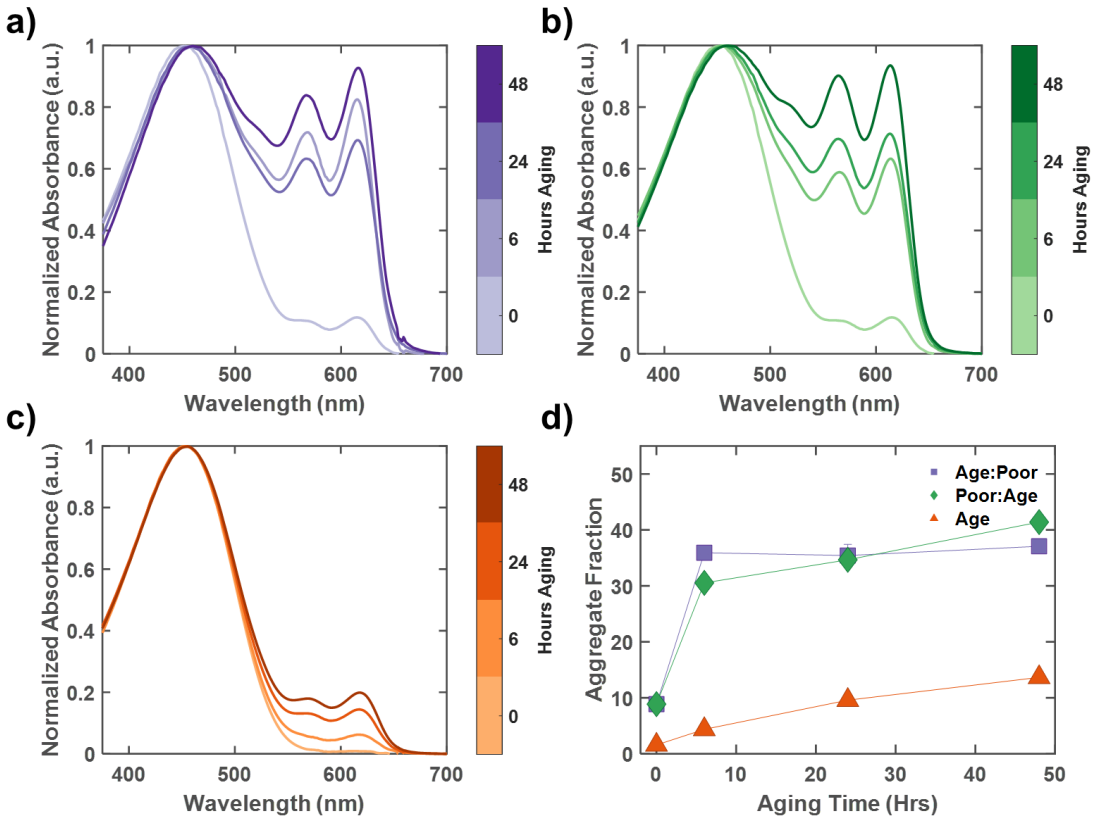

Figure 47: Solution UV-vis spectra of a) Age:Poor, b) Poor:Age, and c) Age samples as a function of aging time. d) Extracted aggregate fraction from deconvolution of UV-vis spectra.

5.3.1.2 X-Ray Scattering Analysis

X-Ray scattering was used to probe the mesoscale crystallinity of the thin films after blade coating. **Figure 48** depicts representative small angle X-ray scattering (SAXS) images of the three samples after 24 hours of aging. The lamellar packing distance was extracted from the peak position of the (100) peak and displayed values between 16 and 18 Å, consistent with literature values for P3HT. There were no observable trends in the lamellar stacking distance as a function of processing order or solution aging time.

The full-with half maximum of the (100) peak was used to quantify the coherence length, a measurement of the size of the crystalline grains (**Figure 48b**). The Age sample displayed the lowest coherence length with values ranging between 84 nm at 6 hrs of solution aging and 100 nm after 48 hours. The lack of an external driving force for self-assembly besides solution aging results numerous microscale defects from imperfect packing at the aggregate level, resulting in a low coherence length. In contrast the Poor:Age sample displays the highest coherence length that is also subjected to time-dependent assembly. The coherence length in this sample increases from 108 nm after 6 hours of aging to 119 nm after 48 hours, indicating the addition of poor solvent plus solution aging reduces defects at the microscale level. In contrast, the Age:Poor sample exhibits a constant coherence length (ca. 104 nm) with solution aging time. This likely suggests the formation of a baseline degree of crystallinity that is locked into place upon addition of the poor solvent.

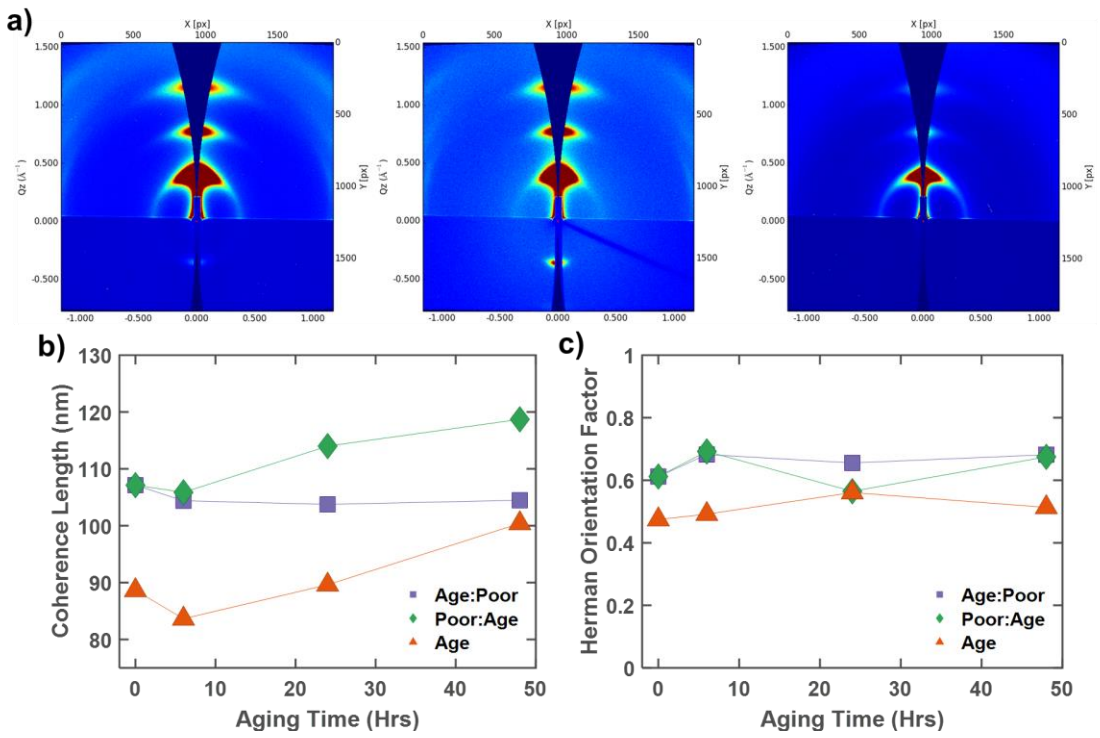

Figure 48: a) SAXs images of Age:Poor (left), Poor:Age (center) and Age (right) after 24 hours of solution aging time. b) Coherence length and c) Herman's orientation factor as a function of processing conditions and solution aging time

Finally, the angular dependence of the scattering intensity of (100) peak was used to determine the Herman's orientation factor that describes the orientation of crystalline grains relative to the substrate surface, shown in **Figure 48c**. Both the Age:Poor and Poor:Age samples display similar Herman's orientation factor values (ca. 0.65). This indicates that the crystalline domains formed display a large edge-on fraction compared to face-on. In transistor applications in which carriers move parallel to the substrate surface, more edge-on characteristics has been shown to be beneficial to enhancing charge mobility. The Age samples has a constant Herman's orientation factor around 0.5, indicating a more random distribution of orientations relative to the surface. These results suggest that the development of nanofibril domains aids the orientational ordering of the nanofibers during the film deposition process.

5.3.1.3 Morphological Characterization

Finally, atomic force microscopy (AFM) images were used to characterize the degree of alignment and packing density of nanofibrillar domains. Based on the image process AFM images shown in **Figure 49**, the observed morphologies for the Age:Poor and Poor:Age are fairly isotropic despite the use of shear-inducing blade coating procedure. In contrast the Age sample displays more anisotropic features but only after 48 hours of solution aging. Note that nanofibers were not observed in the AFM images taken immediately after initial processing (0 hrs). The degree of orientation order and packing density can be quantified using open-source imaging process software. **Figure 50a** displays the extracted S_{2D} orientational order parameters while **Figure 50b** displays the packing density. Notably, the Age:Poor sample generally exhibits a higher degree of orientational order than the other two samples, reaching a value of 0.83 after 24 hours of aging compared to a maximum value of 0.58 for the Poor:Age sample. Interestingly, the Age sample displays the highest orientational order but at cost of 48 hours of solution aging. In terms of packing density, the Age:Poor displays the highest values followed by the Poor:Age.

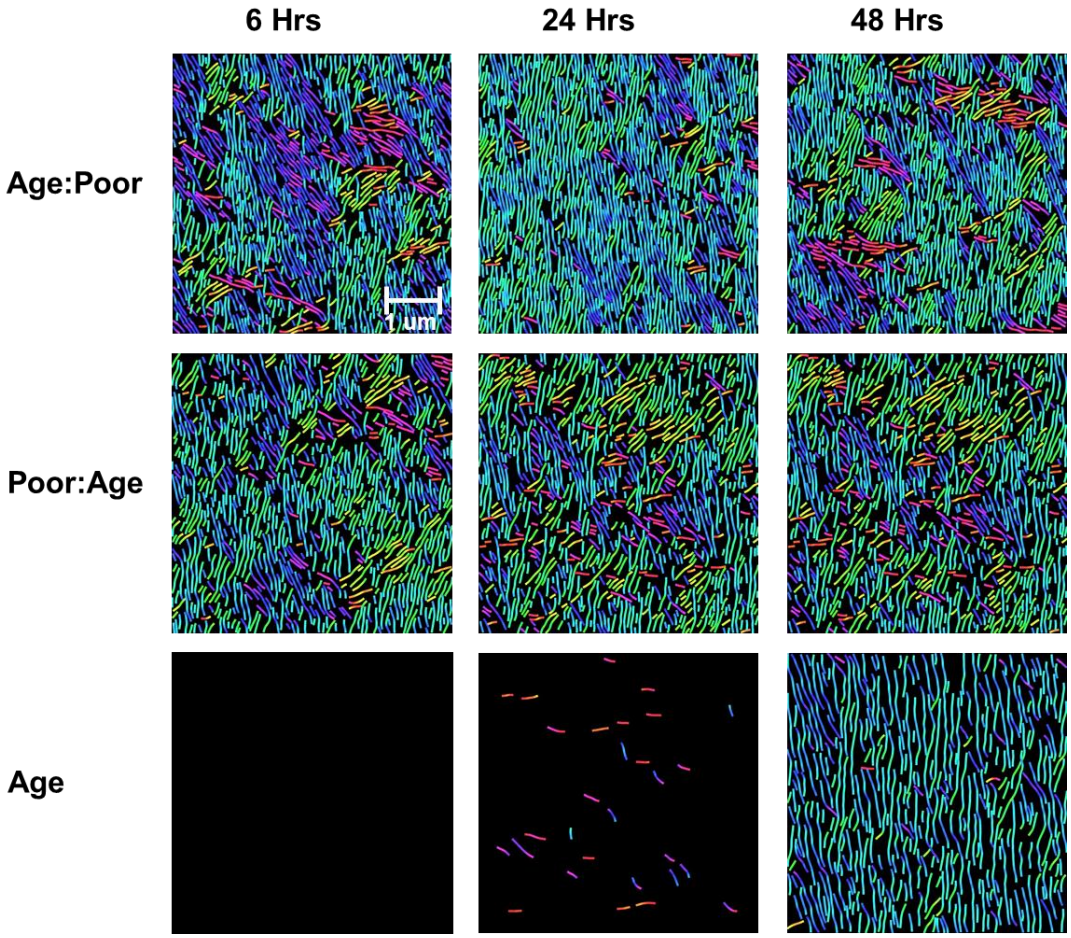

Figure 49: AFM images after image processing as a function of processing method and solution aging time.

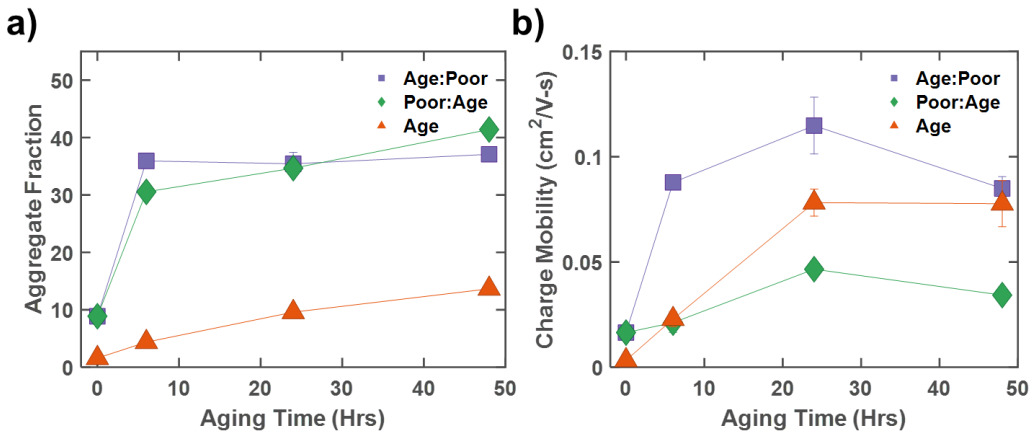

Figure 50: a) S_{2D} order parameter and b) fiber length density as a function of processing method and solution aging time.

It has been proposed that the degree of orientational order that arises during shear coating is correlated with the degree of interconnectivity of the polymer network. This theory is supported by the alignment results presented in this study. In the case of the Age sample, aggregate growth is slow, but chains have sufficient time to assemble with multiple neighboring chains. Once a threshold density of chain connections has been formed, nanofibers can then rapidly grow. Deposition at this point results in highly aligned domains as the nanofibers are highly interconnected. In the Poor:Age case, the poor solvent rapidly induces self-assembly of aggregates. However, the presence of the poor solvent in solution retracts the fringe chains on the edge of nanofibers that could otherwise serve as tie chains. This results in many well-defined but isotropically aligned nanofibers. Finally, in the case of the Age:Poor case, fibers are given time to form initial interconnections with neighboring chains before being forced together due to the poor solvent. Upon blade coating, a sufficient amount of tie chains exists to promote alignment.

5.3.1.4 Electrical Performance

Ultimately, the charge transport properties measuring using organic field-effect transistors (OFETs) can be used to characterize the degree of percolative transport. The charge mobility values of the three samples are shown in **Figure 51.** Immediately after initial solution processing (0 hrs) the charge mobility for all samples is relatively low (~1.0×10^{-2} cm^2/V-s), indicative of a limited number of connective pathways for charges to transports from source to drain electrodes. As shown in the UV-vis analysis, the solutions have not had a sufficient amount of time to assemble into semicrystalline domains (**Figure 52a**). After 6 hours of aging, a significant increase in the charge mobility is observed (0.09 cm^2/V-s) but only for the Age:Poor sample. This likely arises from the formation of a

percolative charge network from the synergistic effects of solution aging that creates an initial polymer network followed by poor solvent addition that forces the network to assembly into interconnected nanofibers. This mechanism of self-assembly continues with further aging of the solutions prior to the addition of poor solvent, reaching a maximum mobility of 0.11 cm^2/V-s after 24 hours. Further aging of the solution prior to the addition of poor solvent results in a reduction in mobility to 0.09 cm^2/V-s, likely from the growth of grain boundaries that reduces mesoscale orientation order (**Figure 52b)**. In contrast, the Poor:Age sample displaces the lowest charge mobility values with a maximum values of 0.05 cm^2/V-s, due to the vast number of grain boundaries. Finally, the age sample is able to naturally form percolative charge transport pathways but are limited by intrachain disorder at the microscale. Overall, these results highlight the importance of interconnected polymer networks for percolative charge transport in organic electronic devices that can transcend from the solution phase to the final thin film (**Figure 52c**).

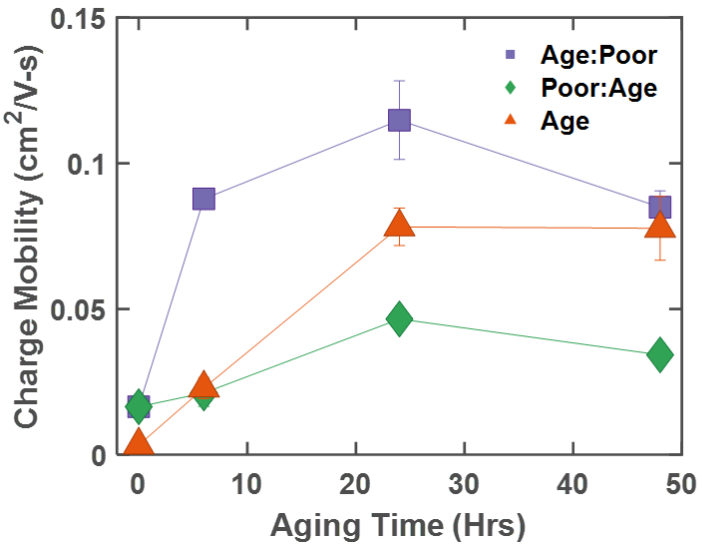

Figure 51: Charge mobility as a function of processing condition and solution aging time.

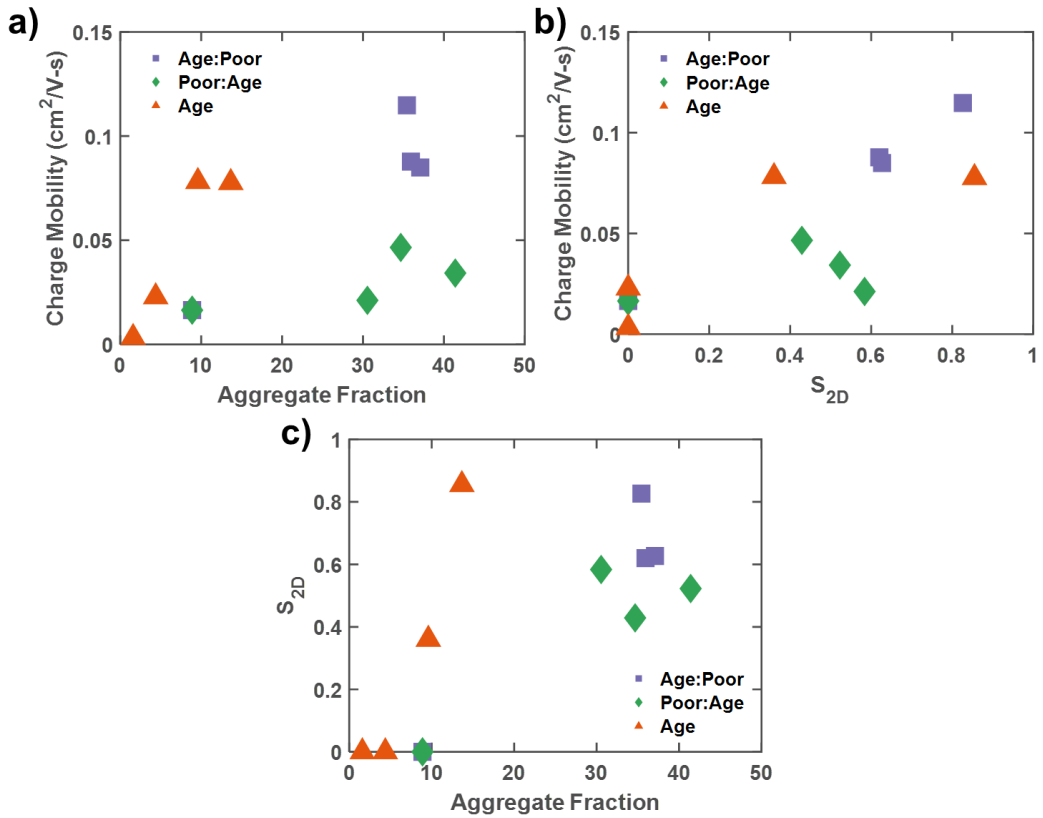

Figure 52: Relationship between a) aggregate fraction from solution and b) S_{2D} on charge carrier mobility as a function of poor solvent and time-dependent self-assembly processing method. c) Correlation between aggregation fraction from solution and S_{2D}.

5.3.2 Transferability of Processing Approach beyond P3HT

Initial experiments were conducted to verify the generalizability of this approach to semiconducting polymers beyond P3HT. PBTTT represents another known semicrystalline semiconducting polymer.[29] Time-dependent self-assembly was observed in a solution of 3 mg/ml of PBTTT in dichlorobenzene within 1 day of solution aging as shown in **Figure 53a**. Notably, this phenomena was not observed within 2 days of solution aging using chlorobenzene, trichloroethylene, or chloroform, indicating the polymer-solvent interactions must be precisely matched to induced time-dependent assembly. The

same poor solvent, 2-MP, used in the P3HT assembly was found to be a sufficient poor solvent for PBTTT as well. **Figure 53b** shows the impact of poor solvent addition on the UV-vis absorption spectra. The observed red shift to longer wavelengths and thus lower energy suggests the formations of aggregated domains that are better able to delocalize charges. Characterization of the electrical properties using field-effect transistors indicates the existence of an optimal amount of added poor solvent (45% by volume) as shown in **Figure 53c**. Overall, these results suggest that the approach of poor solvent addition to polymeric systems that experience time-dependent self-assembly can be generalized across semicrystalline semiconducting polymers.

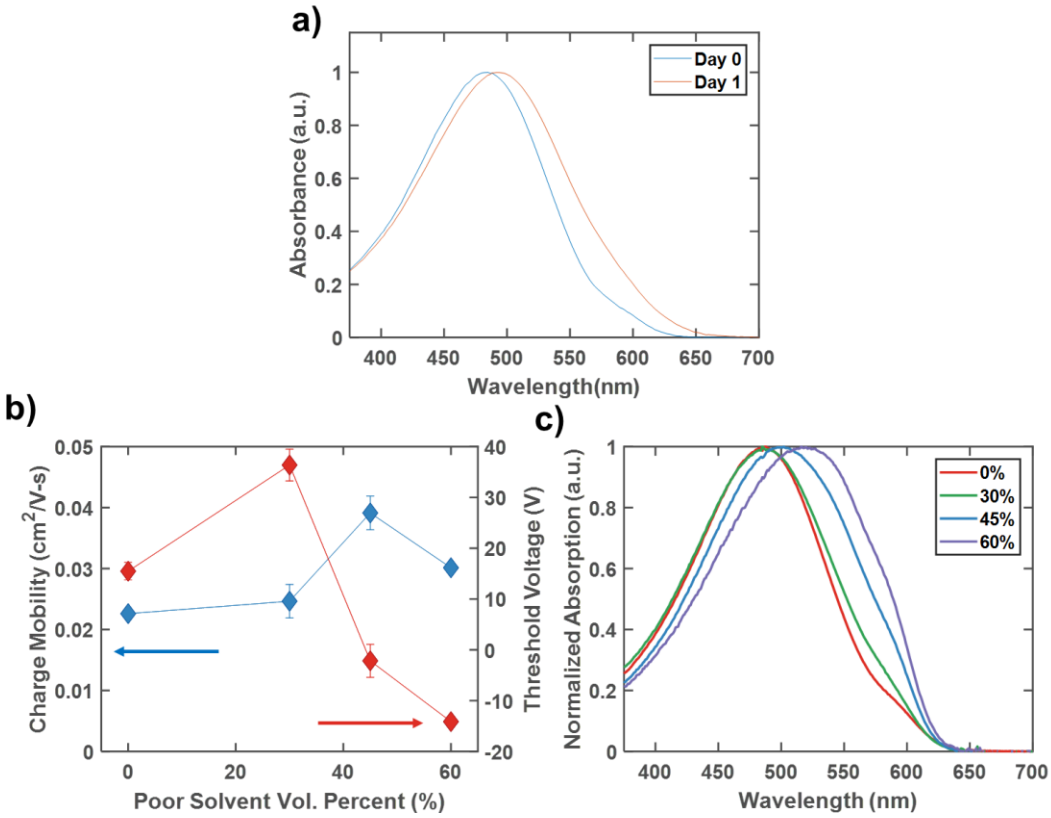

Figure 53: a) Time-dependent UV-vis absorption spectra of PBTTT in DCB. b) Charge mobility and threshold voltage as a function of poor solvent volume fraction. c) Dependence of solution UV-vis spectra on volume fraction of poor solvent (2-MP) addition.

5.4 Conclusions

Cosolvent addition offers an industrially relevant processing approach to induce aggregation of semicrystalline conjugated polymers for precise control of the morphology and thus electrical properties. However, the use of poor solvent is generally limited by the formation of grain boundaries as polymer chains move away from poor solvent molecules to reduce energetically unfavorable interactions. This phenomenon is detrimental to charge transport as percolative pathways are reduced.

Herein we propose a processing method that leverages the time-dependent self-assembly of semicrystalline polymers. Allowing a polymer solution to aging in solution prior to the addition of poor solvent (Age:Poor) enables the formation of interconnected domains that are then maintained when the poor solvent is added. Without this solution aging effect, the addition of poor solvent results in well-defined by isolated nanofibers (Poor:Age) that limits the charge mobility. Structural characterization including UV-vis absorption, small-angle X-ray scattering (SAXs), and AFM analysis was used to develop process-structure-property relationships that supports the proposed formation of interconnected polymer networks in the Age:Poor sample.

However, challenges remain when expanding this method to additional self-assembling polymer systems. A significant amount of work is required to screen solvents that enable time-dependent self-assembly. Additional screening must then be conducted to identify the marginal or poor solvent and to identify the optimal volume fraction of poor solvent that limits the formation of grain boundaries. While not explored in this study, the impact of vastly different boiling points or surface tensions of the two solvents may also play a role. Overall, this work provided an approach to overcome the formation of grain boundaries that generally limits the charge mobility in multi-solvent systems.

CHAPTER 6. SOLVING MATERIALS' SMALL DATA PROBLEM WITH DYNAMIC EXPERIMENTAL DATABASES

6.1 Introduction

Research institutions and their funding sources have made a strong push in recent years to leverage the tools of modern data analytics for scientific research. This effort has fostered the creation of large centralized data repositories, the proliferation of more open-source software and code libraries, and a general move toward 'open science'.[132] The tools of data analytics and informatics were developed to analyze truly massive databases containing millions to billions of entries, such as the collective Google search history of a country's population, or the Amazon shopping history of the same. As such, early efforts in the sciences have focused on the assembly of the largest possible collections of data, namely: thermodynamic constants for every known chemical compound, density functional theory (DFT) simulations of every known crystalline material, or characterization data from every known biological protein.[133-137]

While the scope of these centralized databases is vast, they still do not capture the full extent of the scientific data collected and published on a daily basis. Day-to-day research is not driven by a desire to fill in the billionth row of a central repository, but rather to solve problems and produce knowledge in specialized fields with moderately-sized communities and dynamic trends. The design of a new research study is most often based upon the results of a few dozen previous studies at most. This would not be considered 'big data' by any measure, yet these small sets of experimental results play a

crucial role in daily decision-making. In order to use data analytics to guide this decision-making process, it would be beneficial if the datasets from related publications were assembled into interim databases with a common schema. It is likely that many researchers already aggregate data in this way, especially for a formal literature review. This is all the more reason to develop tools and strategies to work quantitatively with these small, sometimes sparse datasets.

Experimental research in materials processing depends crucially on the selection of a promising initial design region within the available process parameters. When processing a material, there are many potential design variables by which to optimize its properties and performance, including formulation, equipment selection, and settings. The challenge of process design for materials differs from chemical production, because the process influences the material's structure, which further influences its properties. Some crystalline solids and disordered liquids are processed to reach an equilibrium structure, but many materials, such as the soft materials presented here, are guided to process-dependent non-equilibrium states, sometimes with multiple phases. Furthermore, interfacial structures can often influence or even dictate the final performance beyond the bulk material properties. Selecting a process variable design space for a new experiment should thus be approached using as much quantitative knowledge as possible.[138]

Data mining approaches to experimental design have experienced a recent uptick in interest. For example, Kim *et al.* performed an automated review of the synthesis conditions of metal oxides across over 12,000 manuscripts. Their data extraction pipeline consisted of a combination of trained machine learning models and software such as ChemDataExtractor. A decision tree classifier considering 27 synthesis variables was

trained to predict whether or not a titania synthesis route would produce nanotubes, achieving 82% accuracy.[139] Agrawal *et al.* compared a range of machine learning approaches, including multivariate polynomial regression (R^2 = 0.9801), support vector machines (R^2 = 0.9594), and artificial neural networks (R^2 = 0.9724), to predict the fatigue strength of steels.[140] Input variables describing chemical composition, processing temperatures and times, and upstream processing details were taken from the National Institute of Materials Science (NIMS) MatNavi.[141] Ren *et al.* combined literature data and high-throughput experiments to predict the likelihood of finding metallic glasses in the Co–V–Zr ternary.[142]

The use of the design of experiment methodologies to generate ideal process–property databases is another approach to enable subsequent data mining of process–property relationships. This is exemplified by AbuOmar et al. and Zhang et al., where polymer nanocomposite databases were generated via carefully designed experiments.[143-144] The databases generated using uniform design approaches typically only survey low-dimensional design spaces with *a priori* domain knowledge to appropriately grid experimental values.[145] The common element among databases generated via design of experiments is the accessibility of fully informed databases with all descriptors fully characterized and reported.

The scientific literature can be conceived as an unstructured materials database, rich with process–property data points, and sometimes containing structural measurements. However, the nature of exploratory materials discovery suggests a high-dimensional design space, with individual publications providing a limited number of data points. There are several challenges in constructing and analyzing a literature database, even with manual

construction by domain experts, namely: (1) literature reports do not have standardized fields for frequently-reported quantities; (2) authors report non-overlapping sets of information, leading to data sparsity; and (3) reporting of design variables and property measurements suffer from variability due to measurement equipment, inconsistent application of mathematical models, and human error.[146] Persson et al. provides an illustrative example of these challenges by mining the literature on poly(3-hexylthiophene) organic field effect transistors.[147] Over 200 data points from 19 publications describing the role of 28 processing variables were curated to predict charge carrier mobility. Identifying a subset of the five most similar devices reduced the range of charge carrier mobility values from over six orders of magnitude to three. The presence of unreported, missing data limited the applicability of the standard classification and regression materials informatics techniques.

Herein, we demonstrate how the construction of a structured database containing relevant literature results can be used to guide experimental design for materials processing. This tailored approach to classification is proposed to specifically handle datasets with missing data but is also applicable to fully characterized databases. The set of best performing points indicates a promising design region for future experiments. Two case studies are presented to demonstrate the approach, with each database containing 100–200 data points. The number of data points is largely governed by the available relevant publications. The analysis is primarily intended to guide future experiments into regions likely to have the desired properties. Further local optimization can then be performed using response surface methodology.[148-149] Once the optimal point is identified, then

additional design variables could be added to enable further improvement, or previously unexplored regions could be explored.

6.2 Materials and Methods

6.2.1 Database Construction

The databases are constructed manually using a Microsoft Excel spreadsheet. The data extracted from relevant publications is found in text, tables, and graphical format. Each row in the spreadsheet corresponds to a particular data point. The columns represent the process design variables, which may be numerical (continuous or integer) or categorical. In some cases, the categorical variables (e.g., solvent type) are augmented with numerical descriptors to quantify their properties (e.g., solvent boiling point). In other cases, the categorical variables are hierarchical (e.g., deposition method: spin-coat) with associated numerical values quantifying that category (e.g., spin rate and spin time). Each property measurement is also associated with a column. Additional columns are included so as to document the source of each datapoint, including its digital object indicator (DOI). Further metrics of the journal impact factor and the number of citations of the paper can also be included, but present additional complications as they change over time.

While this manual, *ad hoc* approach is not ideal from a scalability standpoint, the cost of automating this step can be prohibitive in terms of time and expertise. Furthermore, the automation of data extraction requires a significant number of labeled training examples, and the construction of the training set frequently accomplishes so much of the labeling that it makes more sense to simply finish the job manually. This trade-off should be evaluated on a case-by-case basis.

6.2.2 Classification Approach

A common approach to the classification of data is the support vector machine (SVM), which, in its simplest form, constructs a hyperplane to divide two prelabeled classes. This approach is exemplified by Kim et al., who separated metal oxide structures into nanotube-forming and non-nanotube-forming by their processing conditions.[139] SVMs are optimized to maximize the distance between the decision boundary and the nearest point from each class. In other words, SVMs try to minimize the occurrence of misclassification on both sides of the boundary. In exploratory research, however, it is much worse to exclude a potential positive result from consideration than it is to run an experiment that turns out negative. Here, we apply a different approach to classification, in which the objective is to retain all datapoints with good properties in the "promising region".

A property of interest is selected, then a critical value of that property is specified by the user. All datapoints in the database are thus labeled as 'high' or 'low', depending on whether they lie above or below this critical value. The region of the design space that contains all the 'high' points is then constructed. **Figure 54** illustrates this classification approach. This approach helps to ensure that potential positive results are never excluded from the promising region. It is, however, inherently sensitive to outlier points, in which a 'high' property value has been incorrectly reported. These outliers should be uncommon, because such results would most likely have received great interest and scrutiny in the review process. Nonetheless, points with a reported 'high' performance should receive further investigation in subsequent experiments, that is, they should be repeated to validate (or invalidate) their good performance.

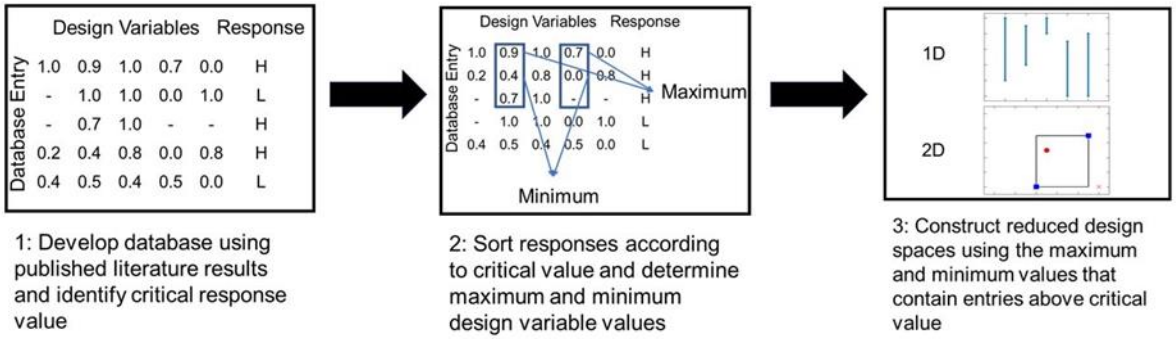

Figure 54: Steps in the classification approach to construct reduced design regions

One possible implementation for quantifying the promising region is to construct a convex hull containing all of the 'high' points in the literature database. Here, we take a simpler approach, which is to calculate the upper and lower bounds of each design variable within which all of the 'high' points are contained, defining a box. The rationale is to provide better intuition and visualization for the user. For each design variable, one compares the minimum and maximum values for 'high' performance to the minimum and maximum values in the entire database. The design space for future experiments is subsequently reduced by focusing future experiments on past 'high' performing regions. This reduction r_S can expressed mathematically, as follows:

$$r_s = \frac{\prod_1^{n_s} l_{s_i}}{\prod_1^{n_s} L_{s_i}} \tag{13}$$

where S is the set of indices for a subset of the design variables, n_s is the dimensionality of the design space (equivalent to the size of S), l_i is the span of variable i that contains 'high' points, and L_i is the span of variable i over all points in the database. In the one-dimensional (1-D) case, r_S is the relative length of the line segment that contains the 'high' points, while in the two-dimensional (2-D) case, r_S is the relative area that contains the 'high' points.

Each design variable, or combination of design variables, is then represented with a value of r_S between 0 and 1, where it is hypothesized that a smaller value signifies that the associated design variable is a better predictor of a 'high' performance.

While r_S expresses the volumetric reduction of the design space, it is also useful to understand the fraction of the original data contained in the promising region, as data density is likely non-uniform. This is expressed as follows:

$$F_r = \frac{|d|}{|D|} \tag{14}$$

where d is the number of points contained within the box and D is the total number of observations in the database. Each observation corresponds to a row in the Excel spreadsheet database.

It is certainly possible that the box excludes potential regions of high performance that were not investigated in previous studies. One could apply a padding parameter to the box bounds to reduce this risk. Alternatively, future experiments can explore additional regions, locally, through response surface methodology, or more globally, with random experimental settings or a particular focus on unexplored regions. Certainly, physical models and domain expertise will also guide future experiments, but the details of the experimental design are beyond the scope of this chapter.[148-150]

6.2.3 Case Studies

6.2.3.1 Poly(3-hexylthiophene) (P3HT)

Poly(3-hexylthiophene) is a semiconducting polymer that has been widely studied for application in large-area flexible electronics.[151] Such systems could access new markets beyond silicon transistors if they can be printed economically in a roll-to-roll process. Thin films of P3HT exhibit hole mobilities that vary by orders of magnitude, depending on how they are processed.[82] Distinct fibrillar morphologies are observed in the atomic force microscopy, and the morphology can be influenced by the process, and correlated with the hole mobility.[70, 108] Design variables that are reported in the literature include polymer molecular weight and regioregularity, solvent and concentration, deposition method and film thickness, and annealing time.[147] Many of these design variables were investigated in **Chapter 3-5**. This system is depicted in **Figure 55**.

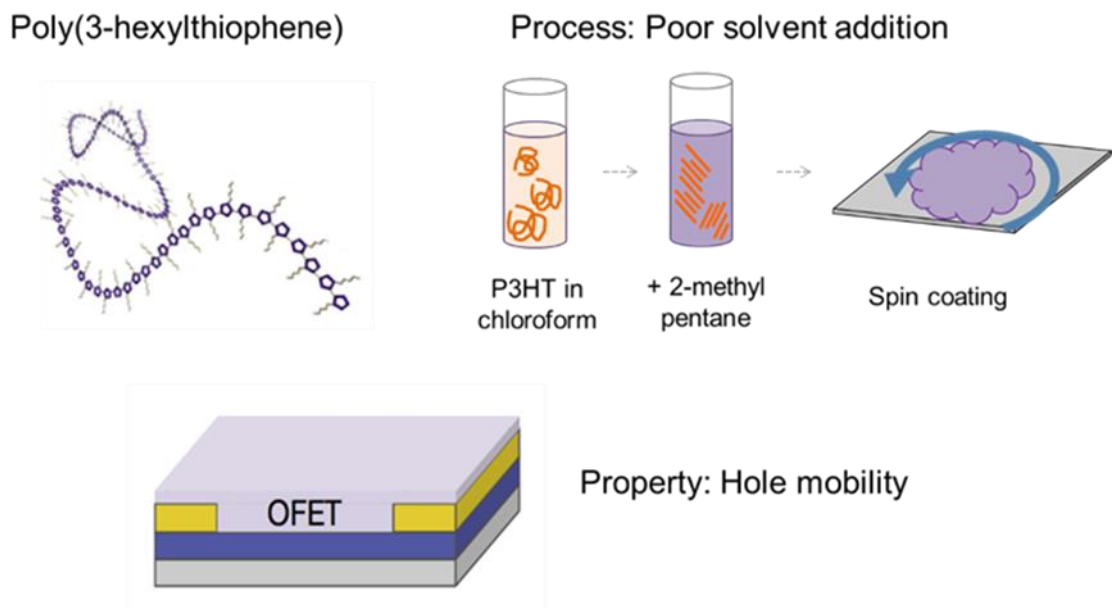

Figure 55: One possible processing route for poly-3-hexylthiophene (P3HT), and a key property of interest in organic field-effect transistor (OFET) performance.

The analyzed database is comprised of 218 datapoints from 19 publications.[147] To model process–property relationships to obtain high mobility devices, 29 design variables were identified that are either numerical (20 design variables) or categorical (9 design variables). The design variables were removed from consideration if all relevant entries were identical, exceptionally sparse, or deemed irrelevant according to expert opinion (e.g., dip rate, dip time, process environment, and electrode material). The mobility values in this database range from 1.0×10^{-6} to 2.8×10^{-1} $cm^2/V\text{-}s$.

This database is included in the supporting data files and is also publicly accessible at: http://www.github.com/Imperssonator/OFET-Database.

6.2.3.2 Polypropylene-Talc Composites

The properties of polymeric materials can be altered and improved by mixing them with fillers to create a composite material.[152-154] In addition, the processing method impacts the properties.[155] Polypropylene (PP) has relatively strong mechanical properties for a polymer and it is widely available. If its properties could be further enhanced, polypropylene might be a candidate for replacing metals, for example in the additive manufacturing of automotive parts. Here, we consider talc as our filler. Talc is a clay material composed of magnesium silicate. It is a good filler candidate for our study because it has been reported to enhance polypropylene performance in many literature studies and because it is relatively inexpensive, enhancing commercial viability.[156-157] This system is illustrated in **Figure 56**.

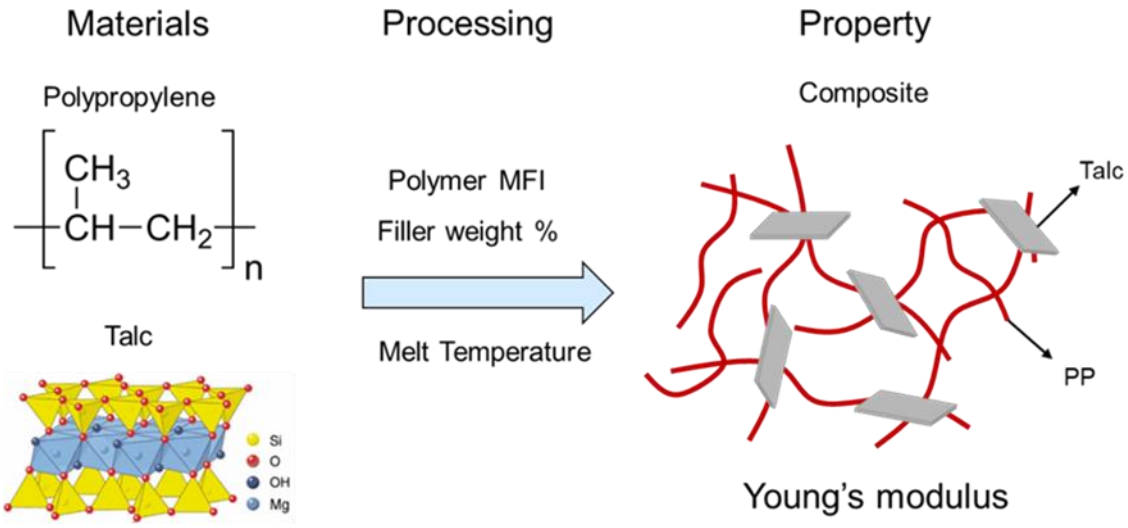

Figure 56: Proposed polymer and filler to develop high strength composites and a key property of interest: Young's modulus.

The polypropylene-talc database is comprised of 140 datapoints from 22 publications with the goal of improving the strength of polypropylene. The Young's

modulus was selected as the relevant mechanical parameter representing the materials' strength. Fourteen design variables were selected for this analysis, with eleven being numerical and three being categorical. Expert opinion was leveraged to characterize differing melt mixer equipment by recording the highest temperature in a multistate extruder. The Young's modulus values for this database vary from 0.38 to 6.94 GPa.

This database is included in the supporting data files and is also publicly accessible at: https://github.com/DocMike/TALC-Database.

6.3 Results

6.3.1 Case Study 1: Poly(3-hexylthiohene)

The breadth of processing conditions recorded in the P3HT database illustrates the utility of the proposed classification approach. In this database, a mobility cutoff value of 0.1 cm^2/V-s was selected to differentiate between 'high' and 'low' devices. The design variables extracted from the literature can be grouped into five main categories, namely: (1) polymer characteristics, (2) solvent environment, (3) deposition conditions, (4) post-deposition processing, and (5) transistor configuration. All of these variables have been hypothesized to influence the morphology of the final semiconducting film and thus the charge carrier mobility.[79, 158]

Figure 57 illustrates the classification approach applied to the P3HT database for 13 of the continuous design variables contained in the database, out of a total of 29 design variables of numerical and categorical type. The one-dimensional analysis is shown in **Figure 52a** for these 13 design variables, with results scaled to the full range of values

reported in the database. For each of these design variables, the difference between the maximum and minimum values associated with a 'high' performance l_i, is divided by L_i, the difference between the maximum and minimum values associated with all entries in the database, according to Equation (13). In some cases, a 'high' performance is observed only for a small fraction of the full reported range, such as for regioregularity, spin rate, and channel width, such that $r_S < 0.1$. In other cases, a 'high' performance can be observed at most of the reported values (molecular weight, initial concentration, boiling point, annealing temperature, and time), such that $r_S > 0.9$. In other intermediate cases, a restricted range can be observed, namely: polydispersity, Hansen radius, film thickness, and channel length.

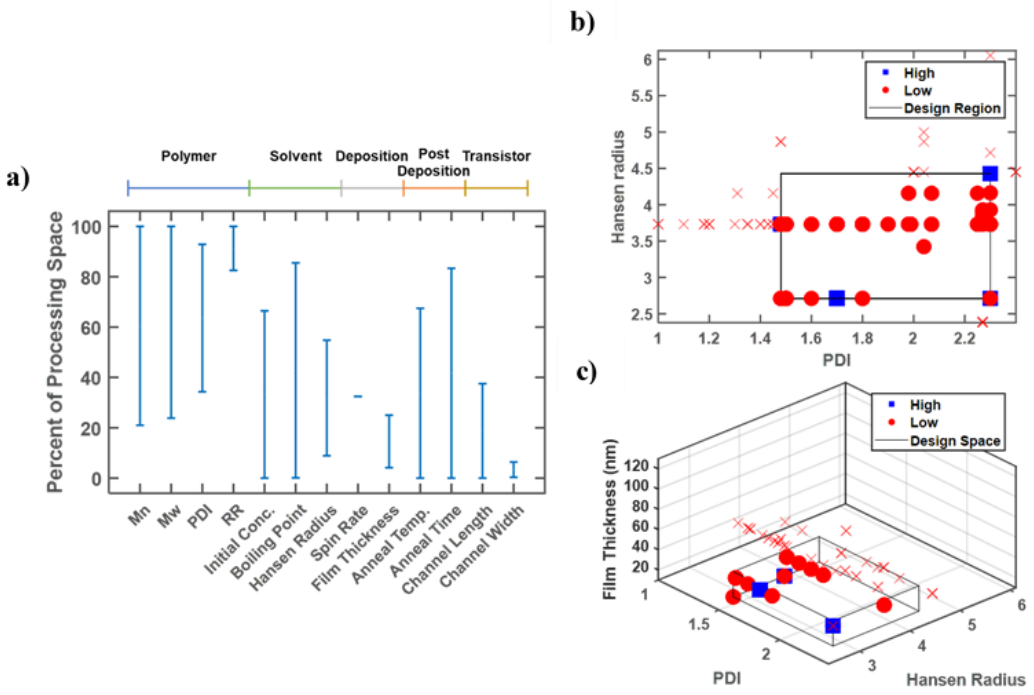

Figure 57: Representative analysis plots of (a) one-, (b) two-, and (c) three-dimensional classifying design variables, resulting in charge mobility values exceeding 0.1 cm^2/V-s. Blue squares are data points above the cutoff, red dots represent points below the cutoff but within the target design region, and red x

markers indicate all other data points below the cutoff but not within the target region. All axis ranges denote the full range of values present in the database.

One might first focus on regioregularity, spin rate, and channel width to reduce the design space for future experiments. However, these are not the best candidates. Regioregularity must be high for a 'high' performance, which is well known; only a small number of the earlier papers used polymers with lower values of regioregularity.[5, 53] Moreover, precision synthesis and characterization of a specific regioregularity is infeasible.[159] Of the 37 'high' devices, only 8 report a spin rate and all 8 arise from the same publication. Thus, spin rate is not an ideal candidate. The channel width is also shown to impact the observed mobility, but device physics indicate that it should not influence the transistor performance.[20] The standardization of test conditions is necessary to improve the quantification of results in polymer organic electronics, and future experiments should conform to this common standard.[160]

The more revealing design variables are those with a moderate reduction of the design space, namely: polydispersity, Hansen radius, film thickness, and channel length. Like channel width, channel length affects performance through device physics rather than material properties and can be excluded. This leaves three key design variables, which can be visualized in two or three dimensions, as shown in **Figure 57b and c**. Note here that original variable scales are used, rather than the scaled variable ranges shown in **Figure 57a**. A high value of polydispersity is required to achieve a good performance, but low values of the Hansen radius and film thickness are also needed.

The two-dimensional plots can be generated for each pairwise combination of design variables, or on the selected promising design variables identified in the one-

dimensional analysis. **Figure 57b** delineates the promising design region using the polymer polydispersity index (PDI) and Hansen radius. The area of the identified design region relative to the full area spanned by the design variables is quantified by $r_S = 0.27$, for $S = \{3,7\}$. Thus, future experimental efforts can be focused on only 27% of the original design region. When film thickness is additionally added as a classifier, $r_S = 0.056$, for $S = \{3,7,9\}$.

However, quantifying the reduction using r_S without visualizing results or utilizing additional metrics can lead to misleading conclusions, depending on the quality of the information in the database. Issues with only characterizing the relative reduction can be grouped into two main categories, as follows: (1) limited coverage of the entire design region (sparsity), and (2) inconsistent reporting and characterization. These cases are illustrated in **Figure 58**. Note that in **Figure 58b**, there are no datapoints shown with regioregularity (RR) values below 90%, despite their presence in the database, because film thickness was not reported for any of those datapoints.

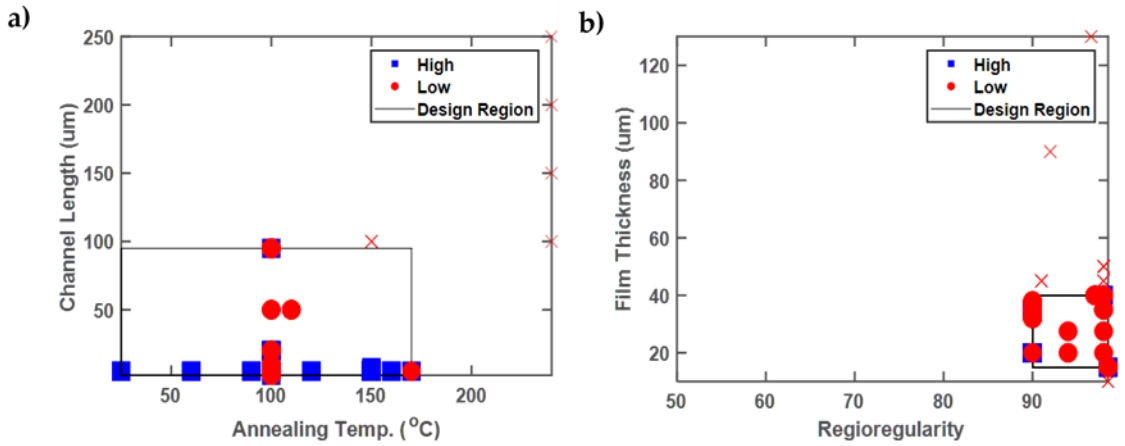

Figure 58: Illustrative two-dimensional plots indicating (a) limited collective screening of the entire design region (sparsity), and (b) inconsistent reporting and characterization. Axis values denote the full range of values present in the database.

The fraction of points contained within the reduced designed region (F_r) serves as a simple indicator for the distribution and sparsity of points throughout the entire design region. **Table 8** highlights both the reduced area and the fraction of points contained in this region. In general, r_s is smaller than F_r, indicating that the volumetric reduction of the design space is greater than the fraction of database points excluded. This can be rationalized in the context of Schrier's Dark Reaction Project; negative results are infrequently reported in the literature.[161] It makes sense that data density would be concentrated in the promising region, because other experimentalists intuitively concentrate their effort in a similar region, and because they omit negative results from outside that region. This is a source of significant bias in the training set, but it can also serve as a sanity check on the selection of the promising region. Nonetheless, the importance of reporting negative results cannot be overstated.

Table 8: Metrics for the two-dimensional analysis of the poly-3-hexylthiophene (P3HT) system. PDI—polymer polydispersity index, RR—polymer regioregularity.

	PDI/ Hansen Radius	PDI/Film Thickness	Hansen Radius/Film Thickness	Channel Length/Annealing Temp	RR/ Film Thickness
r_s (%)	27	12	10	25	4
F_r (%)	45	30	53	45	63

This classification approach can theoretically be scaled to any dimension. However, the reliability of the identified target region containing high performing devices decreases as the dimensions increase. This reliability issue is illustrated in **Figure 57c** with a box denoting the target design region. The data is distributed throughout the x and y plane (PDI and Hansen radius), indicating that these two variables are highly reported. In contrast, no

results are presented with a thickness greater than ~40 nm, despite thickness values as high as 130 nm being reported in the database. This problem arises from a lack of standardized reporting. Despite the fact that 146 of the entries report PDI, 190 report Hansen radius values, and 149 report film thickness, only 105 entries have all three of these variables specified. This issue can also impact the relative volume of the target design region. While the two-dimensional analysis (**Figure 57b**) points to a 'high' device with a PDI value of ~2.3 and a Hansen radius of ~4.5, this database entry does not contain a corresponding film thickness and as a result does not appear in **Figure 57c**. Thus, the analysis of higher-dimensional design spaces to simultaneously optimize numerous processing conditions relies heavily upon consistent and standardized reporting.

In addition to the 13 numerical design variables, three relevant categorical variables were identified. The choice of solvent influences the ability of the polymer chains to self-assemble in the solution and the solvent evaporation rate during the film deposition phase. The analysis performed in this study indicated that the use of chloroform and trichlorobenzene can result in 'high' performing devices, while toluene, thiophene, benzene, chlorobenzene, and styrene do not. **Section 6.3.1.2** will discuss how solubility parameters (Hansen radius) were used to represent a solvent on a continuous scale. Of the 37 'high' performing devices, 28 films were formed through drop casting, 8 via spin coating, and 1 film using dip casting, spanning all deposition methods in the database. It is likely that the interaction of these deposition methods with other process variables was optimized to produce favorable thin film microstructures. Finally, the treatment of the silicon dioxide capacitance layer to modify the wettability and polymer-substrate interface using hexamethyldisilane (HMDS) or no treatment at all can both result in 'high' devices.

In contrast, perfluorodecyltrichlorosilane (FDTS) and octadecyltrichlorosilane (OTS) surface treatments produced unfavorable results. Ideally, surface free energy would be reported as a way to quantify the surface treatment, similar to the Hansen radius for the solvent.

Once the target design region has been identified, hypothesis generation and future experiment planning can occur. Here, we briefly discuss the physical intuition that can guide experimental design beyond the selection of the promising design region.

6.3.1.1 Polydispersity Index

Long polymer chains are required to extend across grain boundaries and thus provide high-mobility pathways through otherwise amorphous regions of the film. The one-dimensional analysis of polymer characteristics (**Figure 52a**) suggests that 'high' performance devices can be obtained with number average molecular weights ranging from 26 kDa to 117 kDa. The PDI indicates the spread of the molecular weight distribution in a polymer sample, so a sample with a low average molecular weight could still contain many long chains if it has a high PDI. Our analysis indicates that a PDI >1.5 is required for a high-performance device. However, there is experimental difficulty in synthesizing polymers with tailored PDIs for systematic studies[126]. Instead, techniques to either fractionate the P3HT samples or blend multiple polymers samples to target a specified PDI have been employed, as presented in **Chapter 3**.[126]

6.3.1.2 Hansen Radius

Thin film formation is a complex and dynamic process in which solvent evaporation governs structural organization mechanisms such as polymer aggregation and phase separation.[41] These processes are captured, albeit incompletely, through the initial polymer concentration, solvent boiling point, and Hansen radius, in addition to the equipment deposition parameters (e.g., spin rate, spin time). According to the one-dimensional analysis, the Hansen radius provides better discrimination between high and low performance devices compared with both the initial polymer concentration and the boiling point. The Hansen radius is a numerical descriptor of solvent–polymer interaction energy and can be used to reduce the number of design variables when solvent mixtures are utilized.[61, 64, 142, 162] As an example, the dissolution of P3HT in a good solvent, followed by the addition of a poor solvent, was utilized as a processing method by 3 of the 19 papers in the database.[61, 64, 163] To fully characterize this, two categorical variables (good solvent, poor solvent) and one numerical variable (volume fraction of poor solvent) need to be specified. By applying the Hansen solubility model, these three variables can instead be reported as a single numerical value, the Hansen radius, simplifying the interpretation of the database and extraction of process–property relationships.

6.3.1.3 Film Thickness

An analysis of the database suggests that film thicknesses ranging from 25 to 40 nm are desired in order to obtain high-performing devices. This observation is in general agreement with work by Joshi et al., which explored the thickness dependence of the charge mobility of low molecular weight P3HT.[164] In their study, mobility plateaued after a

thickness of 15 nm, due to the orientation of crystalline grains at the transistor oxide-P3HT interfaces. Varying the thickness of the P3HT films is usually the result of changing another design variable, such as polymer concentration or spin rate, and is highly dependent on the kinetics of the solution-to-film phase transition.[164-165] Ideally, an influential design variable should be able to be varied independently from other process conditions. Recent advances in blade and shear coating techniques, currently not captured by the database, offer a promising approach to independently control the film thickness to explore its impact on charge carrier mobility.[50, 56]

6.3.2 Case Study 2: Polypropylene-Talc Composite

The polypropylene–talc database was constructed from 22 publications, with a total of 140 data points. The property of interest that was selected was Young's modulus. While there are many ways to quantify mechanical properties (fracture strength, toughness, etc.), Young's modulus was selected here, in part because of the importance of stiffness in a mechanical component such as an automotive part. It is also widely reported in the literature because it is relatively easy to measure. A cutoff value of 5 GPa was selected for the Young's modulus, with 11 points (8%) having 'high' values above the cutoff value.

Similar to the P3HT study, the minimum and maximum reported values of 11 continuous design variables were identified in the full database and the high-performing subset to calculate r_s. The results of this one-dimensional analysis are shown in **Figure 59a**, using variables scaled to the minimum and maximum values in the database. Several design variables have an extremely limited range of values associated with high performance, namely, polymer weight-average molecular weight, polymer polydispersity,

filler surface area, and composite density. In all four cases, this large reduction in range is due to very low rates of reporting. For example, only 30 data points have the molecular weight reported, and only two of those points have a ‘high’ performance. Both data points are from the same publication and have the same molecular weight. Other design variables have no range reported at all, including mold temperature and composite melt flow index (MFI), again due to underreporting—none of the high performing points have reported values for mold temperature or composite MFI.

In contrast, filler density and melt temperature are reported for most entries. Since the only filler in the database is talc, there is little actual variation in its reported density, except for one outlier entry that may be misreported. The melt temperature also extends across most of the range in the database, although low values (lowest 20% of the reported range) seem to be undesirable since they are never reported together with a ‘high’ performance.

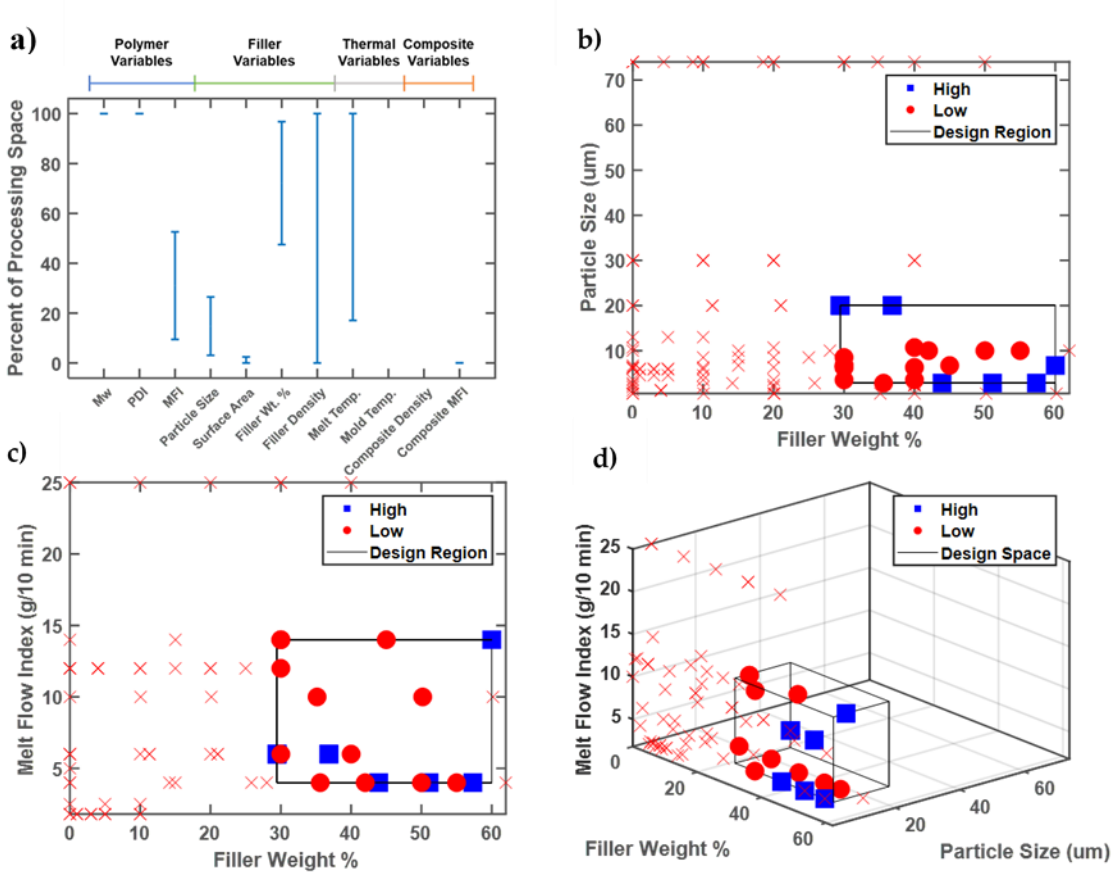

Figure 59: Representative analysis plots of (a) one-, (b,c) two-, and (d) three-dimensional analysis, classifying design variables that result in Young's modulus exceeding 5 GPa. All axis values denote the full range of values present in the database. Blue squares are data points above the cutoff, red dots represent points below the cutoff but within the target design region, and the red x markers indicate all other data points below the cutoff but not within the target design region.

The design variables with intermediate ranges in **Figure 59a** are polymer MFI, filler particle size, and filler weight percent. These three design variables contribute the most information to the future experimental design. It is notable that all three are related to material composition, rather than processing conditions. The melt flow index correlates inversely with the molecular weight, but is much more commonly reported in the database, because of the difficulty of dissolving polypropylene for the characterization of molecular weight by size exclusion chromatography.[166] The database analysis suggests that high

stiffness requires a low polymer MFI, or equivalently, a high molecular weight. The filler particle size falls in the lowest third of the reported values, while the filler weight percent falls within the upper half of the values reported in the database.

The data can also be viewed in higher-dimensional spaces, as follows: **Figure 59b** illustrates the promising design region associated with filler size and weight percent. Note here that original variable scales are used, rather than the scaled variable ranges of **Figure 59**. Future experiments can focus on this smaller box having low (but not too low) filler size and high filler weight %. The unexplored region of particle size in the range 35–70 μm could also be tested, depending on the experimental budget and availability of larger talc particles. **Figure 59** again shows a two-dimensional representation, with polymer MFI and filler weight %. The promising design region contains low values of MFI, although there is little data available at higher MFIs. Future experiments could attempt to expand this region into higher MFI values (lower molecular weight), which would also lower viscosity and thus ease processing.

The calculated metrics, including the relative area of the new design region, are shown in **Table 9**. Similar volumetric reductions (r_s) in the identified design region are observed for the PP–talc database compared to the P3HT study. However, similar values of data reduction in the design region (F_s) for the PP–talc database suggests that the community has more thoroughly sampled the entire design region compared with the P3HT community. This could arise from the reduced number of considered design variables for the polymer composites (14 variables) compared with P3HT for organic electronics (29 variables).

Table 9: Quantified metrics of two-dimensional analysis for the PP-talc system.

	MFI/Particle Size	MFI/Filler Wt.%	Particle Size/Filler Wt.%
r_s (%)	10	21	12
F_r (%)	28	14	15

Finally, a three-dimensional representation is shown in **Figure 59d**. The promising design region is about 5% of the volume of the full range of design variables reported in the database. Also notable in **Figure 59d** is the lack of data points at the high particle size of 74 μm, which were previously plotted in **Figure 59b**.[167] Since no value of polymer MFI was reported for those points, they cannot be visualized in **Figure 59d**, and more importantly, they cannot be reproduced since the value of the polymer MFI that was used is unknown. Since Gafur et al. did report the weight-average molecular weight, a model could potentially be used to estimate the unreported MFI.[166-167] Physically-based correlations provide a potential route to filling in missing data, which may be more effective than linear imputation[168] when the relationships between design variables are known and are nonlinear, such as the inverse correlation between MFI and weight-average molecular weight (Mw). However, since the Gafur et al. data points have a 'low' performance, such modeling would not change the promising region.

The polypropylene–talc database contains 11 continuous design variables, but also incorporates three categorical variables, namely compatibilizer, talc surface treatment, and the film formation method. Only 23 data points report a compatibilizer, with none of these data points resulting in 'high' performance. Twenty-two data points report a surface treatment, but only aminopropyl-trimethoxysilane (4 data points) resulted in Young's

modulus values above 5 GPa. This categorical variable presents a seldom-used processing condition to further explore. Films are formed either through extrusion or compression molding, but only compression molding produced a 'high' performance. Better understanding of the mechanistic reasons for improved performance via compression molding could help identify new processing conditions, but in the short term, compression molding is the preferred technique.

6.4 Discussion

Significant advances have been made in applying materials informatics and machine learning techniques to leverage the combined knowledge of research communities. The advent of large centralized materials data repositories that are publicly accessible has been a tremendous boon to accelerated materials discovery and process optimization. However, the curation and use of materials data that are generated on a day-to-day basis, within a given material system under a formalized materials informatics lens, is still in its infancy. Smaller, more specific databases relevant to a particular application will be required to rapidly provide chemical compositions and optimized processing conditions.

A key challenge seldom addressed in 'small data' materials research is how to extract meaningful process–structure relationships to target desired properties. Small data can be curated in two main approaches, namely (1) controlled experiments via the design of experiments or high-throughput methods within a single laboratory, and/or (2) mining the literature to leverage experiments conducted by the community. The former datasets are often well-structured, allowing process–property information extraction via material

informatics and/or machine learning methodologies.[140, 142] The latter approach involves a significantly wider scope of potential design variables, resulting in an unstructured database rife with missing and noisy data. Missing data limits the applicability of materials informatics approaches, including decisions tress, neural networks, and support vector machines. Instead, an approach that uses all available data in a small material database to identify promising design regions for future experimentation has been proposed. This approach aims to provide quantitative guidance to focus experimental work based on the collective work on the community. Ideally, these future experiments will fully characterize all design variables to enable regression and machine learning approaches. The metrics, r_s and F_r have been proposed to describe the relative importance of process variable combinations in determining material performance. Design regions with smaller r_s and F_r values should be prioritized for future experiments. Overall, the analysis presented is general and can be expanded to examine any subset of relevant design variables.

Several opportunities and obstacles still await the widespread use of literature-guided materials databases. Once the database has been reduced to a targeted design region that contains the 'high' performing data points, justifications for the presence of 'low' data points in this region can be suggested. In the polypropylene-talc case study, the three-dimensional promising region contains six high performing points, but also nine points with a low performance. Attempts to classify based on additional design parameters were unsuccessful. The impact factor of the journal was added as an additional classifier, which did separate the three studies containing high performance from the three studies containing low performance. With a more complex database, the incorporation of

additional variables has the potential to distinguish and inform more reliable and robust datasets.

A potentially problematic subset of data, termed ‘hierarchical data’, is prominent amongst materials literature. Hierarchical data is defined here as paired categorial and numerical data, in which the numerical data is only relevant for that category. An example from the P3HT case study is the spin rate that is only relevant to spin cast P3HT devices, rather than dip coated devices, which are quantified instead by the dip rate. Hierarchical data requires special attention to ensure that the numerical data is not used as a predictor without the associated categorical variables.

The most significant of challenges is the handling of missing data to ensure quality predictors that reflect all of the relevant publications and not just the most-well characterized. As discussed, mining data from highly exploratory work can result in unreported data from a lack of standardized reporting templates, the discovery of new important promising conditions and/or access to various equipment and characterization techniques. Data imputation techniques have been recently developed to fill in missing values. These techniques range in complexity from imputing the population mean value to modified nonlinear iterative partial least squares regression. The latter approach has been shown to be an effective technique when the missing data is randomly distributed, rather than in structured blocks.[169] Research by Nelson et al. and Ferrer et al. has shown that principal component analysis approaches are better suited to structured blocks of missing data that may be more prevalent when developing literature databases.[170-171] Data imputation has been applied to materials datasets but, to our knowledge, not been used on literature databases. For example, Verpoort et al. trained an artificial neural network to

identify erroneous values and impute missing data based on polymer composite properties provided by manufacturers' datasheets.[168] However, only eight out of thousands of data points were missing and imputed, a marked difference to the amount of missing data found in the literature databases. Secondary approaches to handle missing data involve physical models, where known data serves as the input to an established model to predict the missing values. In the talc case study, experimental data relating polymer molecular weight to MFI was highlighted as an example.[166] Relating the spin rate to predict missing film thickness values could serve as an example for the P3HT case study. However, accurate physically based models may require additional experiments for validation.

The development of a material database from literature data is still largely a manual process, with numerous decisions made by the curator.[139] Data must be extracted from text, tables, and graphs, and must be organized in a meaningful manner. At present, automated data extraction tools are in their infancy and their implementation presents a major technological hurdle to researchers not well-versed in machine learning. Manually extracted data will be instrumental in providing training sets for the development of such tools. In pursuit of this goal, it is essential that ontologies and schema remain flexible. Research data does not necessarily cluster into fields with hard boundaries, and as such, the entries from one field's database should be adaptable to other fields' databases.

Finally, experimental databases are dynamic, living documents that should be easily accessible to the community. To fully utilize an experimental database, new experiments must be added, and the analysis needs to be updated on a continual basis. The question of who curates and maintains material databases is still an ongoing question in the materials community. Kalidindi et al. suggested the National Laboratories as a central entity to create

a standardized strategy for materials data analysis, but this may only be appropriate in the case of big data.[132] The Protein Databank demonstrates a different model with an independent consortium as the curating body.[172] As small dynamic experimental databases are essentially quantified in literature reviews, the responsibility may rest on individual research groups to compile data for review articles, and on publishers for long term curation.

CHAPTER 7. CONCLUSIONS AND FUTURE WORK

7.1 Conclusions

Robust and industrially-relevant solution processing methods that precisely control polymer self-assembly are essential to achieving optimal and repeatable electronic device performance with semi-crystalline conjugated polymers. My research follows a bottom-up approach to develop process-structure-property relationships using the "fruit fly" of conjugated polymers, poly(3-hexylthiophene) (P3HT). The work presented herein progresses from varying chain lengths to mixing nucleated and non-nucleated samples to control the growth using a UV-irradiation technique that has thus far only been demonstrated on P3HT. The work then aims to exploit a general time-dependent self-assembly approach with poor solvent addition that is generalizable across self-crystalline semiconducting polymers. The commonality across all experimental work is the control of an interconnected pathway for charge carriers.

In **Chapter 3** the formation of these pathways was formed by blending solutions of known molecular weights to access molecular weight distributions that are otherwise inaccessible due to challenges with targeting specific chain lengths during polymerization. Superior charge transport properties, measured using organic field-effect transistors, were observed in samples with a "medium" MW (66-74 kDa), regardless of the polydispersity. Furthermore, the solution lifetimes of these samples exceed 14 days, a significant improvement over the two-day stability observed in samples outside of this MW range. UV-vis spectral analysis suggested that low M_W P3HT lacks the mesoscale crystallinity required for percolative charge transport. In contrast, the decreased solubility of high MW

P3HT, forces rapid aggregate formation resulting in films with a high degree of paracrystalline disorder. The role of grain boundaries, nanofibrillar order, and macroscale alignment further substantiate these claims through characterization by grazing-incidence wide-angle X-ray scattering (GIWAX), atomic force microscopy (AFM), and polarized optical microscopic (POM) techniques. The results presented in this study elucidate the interplay between polymer solubility, self-assembly, network interconnectivity, and charge transport required for robust polymer ink formulations.

Chapter 4 proposed the blending of pre-nucleated P3HT (seeds) and non-nucleated (amorphous) P3HT to promote the formation of interconnected polymer networks. UV-Vis spectral analysis indicated that the nucleation and growth rates of aggregates could be manipulated via the seed-to-amorphous ratio. This was further supported by examining the packing density and alignment of fibers via atomic force microscopy (AFM) image processing. It was found that samples with more seeds formed more densely packed films. However, faster growth rates and more densely packed films did not correlate with charge transport properties due to grain boundaries (observed in AFM and GIWAX measurements). An optimal ratio of seeds (20-50% by volume) to amorphous chains forms an interconnected network for percolative charge transport. This investigation demonstrates a facile solution processing approach to ensure reliable and reproducible ink formulations via controlled self-assembly. Finally, experiments in a continuous flow system were demonstrated, suggesting direct compatibility with roll-to-roll printing of organic electronics.

Chapter 5 focused on developing general process methods to induce interconnected polymer network formation by changing the solvent quality. The previous

two studies suggested that 'tie chains' that extend from one aggregate to a neighboring aggregate can result in formation of this network. However, these tie chains rapidly contract when exposed to a poor solvent, resulting in many small nanofibrillar structures that possess too many grain boundaries for efficient charge transport. Instead, aging the polymer in a marginal solvent prior to adding the poor solvent results in an interconnected network (structural characterization via AFM, GIWAX, POM). Using this approach, charge mobility values exceeding 0.12 cm^2/V-s were observed, compared to 0.04 cm^2/V-s for poor solvent addition prior to solution aging. This approach was found to be applicable to both P3HT and PBTTT and is expected to apply to all self-assembling conjugated polymers.

Finally, **Chapter 6** applied materials informatics methodologies have aided the development of new materials formulations by leveraging large experimental databases. The wealth of P3HT transistor studies provided an ideal case study. A database of 218 data points from 19 publications was created with mobility values ranging from $1.0x10^{-6}$ to 2.8 $x10^{-1}$ cm^2/V-s. A classification technique in which devices were sorted into high performing and low performing categories was applied. A reduced design space containing all high-performing points, as well as some having poor performance is identified for the purpose of focusing on future experiments. This study indicated that the polymer PDI, Hansen radius (describing solubility), and film thickness are highly influential parameters that impact charge mobility.

As a collective body of work, these four main chapters demonstrate a variety of approaches that help guide process-structure-property understanding towards the industrial use of solution process semiconducting polymers for large area, flexible electronics.

7.2 Future Work

The work presented in this thesis provides ample future studies to progress the field of solution processable organic electronics from lab scale experiments to large scale printing of both P3HT and newly development polymers. As indicated throughout this thesis, precise control of process-structure-property relationships is essential to enable large scale operations.

Feedback control of the self-assembly process in organic electronics provides one approach to control the morphology and electrical properties. The results in the seed nucleation batch study presented in this approach suggests the feasibility for feedback control due to a strong correlation between the solution aggregation fraction and charge mobility. However, there are numerous experiments that would need to be conducted prior to any feedback control. What is the impact of adding nucleated P3HT to a solution that has formed structures during a solution aging process? Can tie chains form between seeds added at different tie points or do they form grain boundaries? Furthermore, methods to reverse the processing would need to be developed in case a solution is "over-processed". Can this be done incrementally, or does the process need to be restarted? The problem can thus be framed in a Markov-state model framework[173] where aggregate fraction and solution exciton bandwidth, for example, are two distinct predictors for charge mobility. Experiments would need to be conducted to determine the feasibility of driving the solution properties within this space.

Secondly, methods to screen the impact of additives on the charge mobility remains an opening question in the field. In this thesis, methods to rapidly screen the required

volume fraction of poor solvent to optimize charge mobility could greatly enhance the development of robust process-structure-property relationships. Initial experiments have been conducted with PBTTT in which small aliquots of known volume of poor solvent are added to a stock solution in a good solvent. Solution UV-vis measurements after each addition can be used as a structural indicator. Initial results are presented in **Figure 60**. The rapid addition and UV-vis absorption characterization of aliquots of poor solvent can be monitored via spectral changes (**Figure 55a**). The deconvolution of the absorption spectra into aggregate and amorphous contributions can map process-structure properties. A stepwise increase in the aggregate fraction at 45% 2-MP suggested the presence of a metastable regime. Subsequent thin film deposition and electrical characterization indicates enhanced charge transport at this point. Further experiments need to be conducted to test the general applicability of this approach. If proven successful, this high-throughput screening method would vastly enhance the ability to generate global process-structure-property relationships.

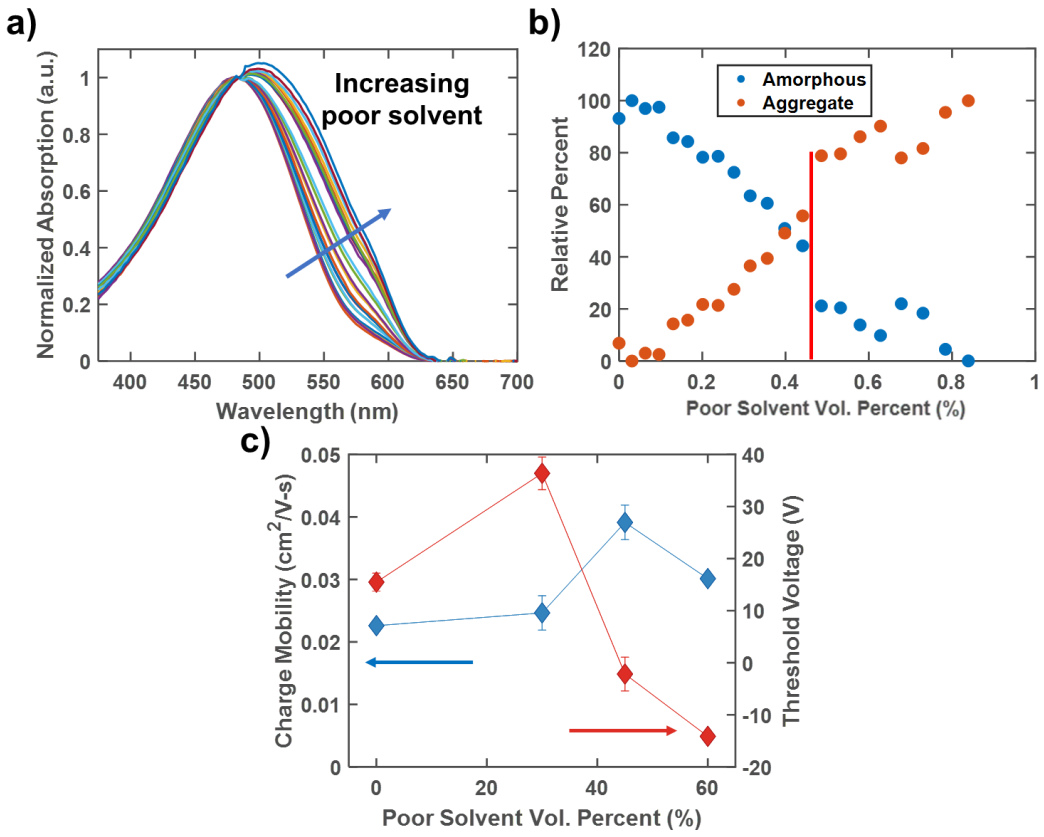

Figure 60: a) Rapid screening of impact of poor solvent on structural development in UV-vis analysis. b) Deconvolution of spectral peaks into amorphous and aggregated contributions c) Observed maximum in charge mobility at point of step-wise increase in aggregate component.

REFERENCES

1. Shirakawa, H.; Louis, E. J.; Alan G. Maciarmid; Chiang, C. K.; Heeger, A. J., Synthesis of Electrically Conducting Organic Polymers: Halogen Derivatives of Polyacetylene, (Ch)X. *J.C.S. Chem. Comm.* **1997,** (16), 578-580.

2. Rughooputh, S. D. D. V.; Nowak, M.; Hotta, S.; Heeger, A.; Wudl, F., Soluble Conducting Polymers: The Poly(3-Alkylthienylenes). *Synthetic Metals* **1987,** *21*, 9.

3. Sirringhaus, H., 25th Anniversary Article: Organic Field-Effect Transistors: The Path Beyond Amorphous Silicon. *Adv Mater* **2014,** *26* (9), 1319-35.

4. Tessler, N.; Preezant, Y.; Rappaport, N.; Roichman, Y., Charge Transport in Disordered Organic Materials and Its Relevance to Thin-Film Devices: A Tutorial Review. *Advanced Materials* **2009,** *21* (27), 2741-2761.

5. Sirringhaus, H.; Brown, P. J.; Friend, R. H.; Nielsen, M.; Bechgaard, K.; Langeveld-Voss, B.; Spiering, A.; Janssen, R.; Meijer, E.; Herwig, P.; de Leeuw, D., Two-Dimensional Charge Transport in Self-Organized, High-Mobility Conjugated Polymers. *Nature* **1999,** *401*, 685-88.

6. Brédas, J. L.; Street, G. B.; Thémans, B.; André, J. M., Organic Polymers Based on Aromatic Rings (Polyparaphenylene, Polypyrrole, Polythiophene): Evolution of the Electronic Properties as a Function of the Torsion Angle between Adjacent Rings. *The Journal of Chemical Physics* **1985,** *83* (3), 1323-1329.

7. Oh, J. Y.; Rondeau-Gagne, S.; Chiu, Y. C.; Chortos, A.; Lissel, F.; Wang, G. N.; Schroeder, B. C.; Kurosawa, T.; Lopez, J.; Katsumata, T.; Xu, J.; Zhu, C.; Gu, X.; Bae, W. G.; Kim, Y.; Jin, L.; Chung, J. W.; Tok, J. B.; Bao, Z., Intrinsically Stretchable and Healable Semiconducting Polymer for Organic Transistors. *Nature* **2016,** *539* (7629), 411-415.

8. Virkar, A. A.; Mannsfeld, S.; Bao, Z.; Stingelin, N., Organic Semiconductor Growth and Morphology Considerations for Organic Thin-Film Transistors. *Adv Mater* **2010,** *22* (34), 3857-75.

9. Kippelen, B.; Brédas, J.-L., Organic Photovoltaics. *Energy & Environmental Science* **2009,** *2* (3), 251.

10. Lee, Y.; Gomez, E. D., Challenges and Opportunities in the Development of Conjugated Block Copolymers for Photovoltaics. *Macromolecules* **2015,** *48* (20), 7385-7395.

11. Sekine, C.; Tsubata, Y.; Yamada, T.; Kitano, M.; Doi, S., Recent Progress of High Performance Polymer Oled and Opv Materials for Organic Printed Electronics. *Sci. Technol. Adv. Mater.* **2014,** *15* (3), 034203.

12. Sekitani, T.; Nakajima, H.; Maeda, H.; Fukushima, T.; Aida, T.; Hata, K.; Someya, T., Stretchable Active-Matrix Organic Light-Emitting Diode Display Using Printable Elastic Conductors. *Nat. Mater.* **2009,** *8* (6), 494-9.

13. Rumens, C. V.; Ziai, M. A.; Belsey, K. E.; Batchelor, J. C.; Holder, S. J., Swelling of Pdms Networks in Solvent Vapours; Applications for Passive Rfid Wireless Sensors. *Journal of Materials Chemistry C* **2015,** *3* (39), 10091-10098.

14. Singh, R.; Singh, E.; Nalwa, H. S., Inkjet Printed Nanomaterial Based Flexible Radio Frequency Identification (Rfid) Tag Sensors for the Internet of Nano Things. *RSC Adv.* **2017,** *7* (77), 48597-48630.

15. Pu, K.; Shuhendler, A. J.; Jokerst, J. V.; Mei, J.; Gambhir, S. S.; Bao, Z.; Rao, J., Semiconducting Polymer Nanoparticles as Photoacoustic Molecular Imaging Probes in Living Mice. *Nat Nanotechnol* **2014,** *9* (3), 233-239.

16. Wang, S.; Xu, J.; Wang, W.; Wang, G. N.; Rastak, R.; Molina-Lopez, F.; Chung, J. W.; Niu, S.; Feig, V. R.; Lopez, J.; Lei, T.; Kwon, S. K.; Kim, Y.; Foudeh, A. M.; Ehrlich, A.; Gasperini, A.; Yun, Y.; Murmann, B.; Tok, J. B.; Bao, Z., Skin Electronics from Scalable Fabrication of an Intrinsically Stretchable Transistor Array. *Nature* **2018,** *555* (7694), 83-88.

17. Wang, X.; Liu, Z.; Zhang, T., Flexible Sensing Electronics for Wearable/Attachable Health Monitoring. *Small* **2017,** *13* (25), 1602790.

18. Loo, Y.-L.; McCulloch, I., Progress and Challenges in Commercialization of Organic Electronics. *Materials Research Society Bulletin* **2008,** *33*, 653-662.

19. Jacoboni, C.; Canali, C.; Ottaviani, G.; Alberigi Quaranta, A., A Review of Some Charge Transport Properties of Silicon. *Solid-State Electronics* **1977,** *20* (2), 77-89.

20. Horowitz, G., Organic Field Effect Transistors. *Advanced Materials* **1998,** *10* (5), 365-377.

21. Newman, C. R.; Frisbie, C. D.; da Silva Filho, D. A.; Brédas, J.-L.; Ewbank, P. C.; Mann, K. R., Introduction to Organic Thin Film Transistors and Design of N-Channel Organic Semiconductors. *Chemistry of Materials* **2004,** *16* (23), 4436-4451.

22. Horowitz, G., Organic Field-Effect Transistors. *Advanced Materials* **1998,** *10* (5), 365-377.

23. Coropceanu, V.; Cornil, J.; da Silva Filho, D. A.; Olivier, Y.; Silbey, R.; Brédas, J.-L., Charge Transport in Organic Semiconductors. *Chemical Reviews* **2007,** *107* (4), 926-952.

24. Bao, Z.; Locklin, J., *Organic Field-Effect Transistors*. CRC Press, Taylor & Francis Group: Boca Raton, FL, 2007.

25. Holstein, T., Studies of Polaron Motion: Part 1. The Molecular-Crystal Model. *Annals of Physics* **1959,** *8*, 325-342.

26. Holstein, T., Studies of Polaron Motion: Part Ii. The "Small" Polaron. *Annals of Physics* **1959,** *8*, 343-389.

27. Brédas, J.-L.; Beljonne, D.; Coropceanu, V.; Cornil, J., Charge-Transfer and Energy-Transfer Processes in Π-Conjugated Oligomers and Polymers: A Molecular Picture. *Chemical Reviews* **2004,** *104* (11), 4971-5004.

28. Gruhn, N. E.; da Silva Filho, D. A.; Bill, T. G.; Malagoli, M.; Coropceanu, V.; Kahn, A.; Brédas, J.-L., The Vibrational Reorganization Energy in Pentacene: Molecular Influences on Charge Transport. *Journal of the American Chemical Society* **2002,** *124* (27), 7918-7919.

29. Noriega, R.; Rivnay, J.; Vandewal, K.; Koch, F. P.; Stingelin, N.; Smith, P.; Toney, M. F.; Salleo, A., A General Relationship between Disorder, Aggregation and Charge Transport in Conjugated Polymers. *Nat Mater* **2013,** *12* (11), 1038-1044.

30. Rughooputh, S. D. D. V.; Hotta, S.; Heeger, A. J.; Wudl, F., Chromism of Soluble Polythienylenes. *Journal of Polymer Science: Part B: Polymer Physics* **1987,** *25*, 1071-1078

31. Assadi, A.; Svensson, C.; Willander, M.; Inganäs, O., Field-Effect Mobility of Poly(3-Hexylthiophene). *Applied Physics Letters* **1988,** *53* (3), 195-197.

32. Sato, M.; Tanaka, S.; Kaeriyama, K., Soluble Conducting Polythiophenes. *J. Chem. Soc., Chem. Commun.* **1986,** (11), 873-4.

33. Yoshino, K.; Love, P.; Onoda, M.; Sugimoto, R., Dependence of Absorption Spectra and Solubility of Poly(30alkylthiophene) on Molecular Structure of Solvent. *Jpn. J. Appl. Phys.* **1988,** *27*, L2388-92.

34. Das, S.; Chatterjee, D.; Ghosh, R.; Nandi, A., Water Soluble Polythiophenes: Preparation and Applications. *RSC Advances* **2015,** *5* (26), 20160-20177.

35. Zhu, J.; Han, Y.; Kumar, R.; He, Y.; Hong, K.; Bonnesen, P. V.; Sumpter, B. G.; Smith, S. C.; Smith, G. S.; Ivanov, I. N.; Do, C., Controlling Molecular Ordering in Solution-State Conjugated Polymers. *Nanoscale* **2015,** *7* (37), 15134-41.

36. Salammal, S.; Mikayelyan, E.; Grigorian, S.; Pietsch, U.; Koenen, N.; Scherf, U.; Kayunkid, N.; Brinkmann, M., Impact of Thermal Annealing on the Semicrystalline Nanomorphology of Spin-Coated Thin Films of Regioregular Poly(3-Alkylthiophene)S as Observed by High-Resolution Transmission Electron Microscopy and Grazing Incidence X-Ray Diffraction. *Macromolecules* **2012,** *45* (13), 5575-5585.

37. Chen, T.; Yu, X.; Rieke, R., Regiocontrolled Synthesis of Poly(3-Alkylthophenes) Mediated by Rieke Zinc: Their Characterization and Solid-State Properties. *Journal of American Chemical Society* **1995,** *117* (1), 233-244.

38. Amou, S.; Hama, O.; Shitato, K.; Hayakawa, T.; Ueda, M.; Takeuchi, K.; Asai, M., Head-to-Tail Regioregularity of Poly(3-Hexylthiophene) in Oxidative Coupling Polymerization with Fecl3. *Journal of Polymer Science Part A: Polymer Chemistry* **1998,** *37*, 1943-1948.

39. Baggioli, A.; Famulari, A., On the Inter-Ring Torsion Potential of Regioregular P3ht: A First Principles Reexamination with Explicit Side Chains. *Phys Chem Chem Phys* **2014,** *16* (9), 3983-94.

40. Brinkmann, M., Structure and Morphology Control in Thin Films of Regioregular Poly(3-Hexylthiophene). *Journal of Polymer Science Part B: Polymer Physics* **2011,** *49* (17), 1218-1233.

41. Chang, M.; Lim, G.; Park, B.; Reichmanis, E., Control of Molecular Ordering, Alignment, and Charge Transport in Solution-Processed Conjugated Polymer Thin Films. *Polymers* **2017,** *9* (6), 212.

42. Agbolaghi, S.; Zenoozi, S., A Comprehensive Review on Poly(3-Alkylthiophene)-Based Crystalline Structures, Protocols and Electronic Applications. *Organic Electronics* **2017,** *51*, 362-403.

43. Wang, H.; Xu, Y.; Yu, X.; Xing, R.; Liu, J.; Han, Y., Structure and Morphology Control in Thin Films of Conjugated Polymers for an Improved Charge Transport. *Polymers* **2013,** *5* (4), 1272-1324.

44. Kim, D. H.; Han, J. T.; Park, Y. D.; Jang, Y.; Cho, J. H.; Hwang, M.; Cho, K., Single-Crystal Polythiophene Microwires Grown by Self-Assembly. *Advanced Materials* **2006,** *18* (6), 719-723.

45. Kim, D.; Park, Y.; Jang, Y.; Kim, S.; Cho, K., Solvent Vapor-Induced Nanowire Formation in Poly(3-Hexylthiophene) Thin Films. *Macromolecular Rapid Communications* **2005,** *26* (10), 834-839.

46. Oh, J.; Shin, M.; Lee, T.; Jang, W.; Min, Y.; Myoung, J.; Baik, H.; Jeong, U., Self-Seeded Growth of Poly(3-Hexylthiophene) (P3ht) Nanofibrils by a Cycle of Cooling and Heating in Solutions. *Macromolecules* **2012,** *45* (18), 7504-7513.

47. Brinkmann, M.; Chandezon, F.; Pansu, R.; Julien-Rabant, C., Epitaxial Growth of Highly Oriented Fibers of Semiconducting Polymers with a Shish-Kebab-Like Superstructure. *Advanced Functional Materials* **2009,** *19* (17), 2759-2766.

48. Malik, S.; Jana, T.; Nandi, A., Thermoreversible Gelation of Regioregular Poly(3-Hexylthiophene) in Xylene. *Macromolecules* **2001,** *34*, 275-81.

49. Zhang, G.; McBride, M.; Persson, N.; Lee, S.; Dunn, T. J.; Toney, M. F.; Yuan, Z.; Kwon, Y.-H.; Chu, P.-H.; Risteen, B.; Reichmanis, E., Versatile Interpenetrating Polymer Network Approach to Robust Stretchable Electronic Devices. *Chemistry of Materials* **2017,** *29* (18), 7645-7652.

50. Chu, P. H.; Kleinhenz, N.; Persson, N.; McBride, M.; Hernandez, J.; Fu, B.; Zhang, G.; Reichmanis, E., Toward Precision Control of Nanofiber Orientation in Conjugated Polymer Thin Films: Impact on Charge Transport. *Chemistry of Materials* **2016,** *28* (24), 9099-9109.

51. Lan, Y.-K.; Huang, C.-I., Charge Mobility and Transport Behavior in the Ordered and Disordered States of the Regioregular Poly(3-Hexylthiophene). *The Journal of Physical Chemistry B* **2009,** *113* (44), 14555-14564.

52. Zhang, R.; Li, B.; Lovu, M.; Jeffries-EL, M.; Sauve, G.; Cooper, J.; Jia, S.; Tristram-Nagle, S.; Smilgies, D.; Lambeth, D.; McCulloch, R.; Kowalewski, T., Nanostructure Dependence of Field-Effect Mobility in Regioregular Poly(3-Hexylthiophene) Thin Film Effect Transistors. *Journal of American Chemical Society* **2006,** *128*, 3480-1.

53. Kline, R.; McGehee, M.; Kadnikova, E.; Liu, J.; Frechet, J.; Toney, M. F., Dependence of Regioregular Poly(3-Hexylthiophene) Film Morphology and Field-Effect Mobility on Molecular Weight. *Macromolecules* **2005,** *38* (8), 3312-3319.

54. Aiyar, A. R.; Hong, J. I.; Izumi, J.; Choi, D.; Kleinhenz, N.; Reichmanis, E., Ultrasound-Induced Ordering in Poly(3-Hexylthiophene): Role of Molecular and Process Parameters on Morphology and Charge Transport. *ACS Appl Mater Interfaces* **2013,** *5* (7), 2368-77.

55. Wang, G.; Persson, N.; Chu, P. H.; Kleinhenz, N.; Fu, B.; Chang, M.; Deb, N.; Mao, Y.; Wang, H.; Grover, M.; Reichmanis, E., Microfluidic Crystal Engineering of Π-Conjugated Polymers. *ACS Nano* **2015,** *9* (8), 8220-8230.

56. Chang, M.; Choi, D.; Egap, E., Macroscopic Alignment of One-Dimensional Conjugated Polymer Nanocrystallites for High-Mobility Organic Field-Effect Transistors. *ACS Appl Mater Interfaces* **2016,** *8* (21), 13484-91.

57. Zen, A.; Pfaum, J.; Hirschmann, S.; Zhuang, W.; Jaiser, F.; Asawapirom, U.; Rabe, J.; Scherf, U.; Neher, D., Effect of Molecular Weight and Annealing of Poly(3-Hexylthiophene)S on the Performance or Organic Field-Effect Transistors. *Advanced Functional Materials* **2004,** *14*, 757-764.

58. Park, Y.; Lee, H.; Choi, Y.; Kwak, D.; Cho, J.; Lee, S.; Cho, K., Solubility-Induced Ordered Polythiophene Precursors for High-Performance Organic Thin-Film Transistors. *Advanced Functional Materials* **2009,** *19* (8), 1200-1206.

59. Lee, Y.; Oh, J. Y.; Son, S. Y.; Park, T.; Jeong, U., Effects of Regioregularity and Molecular Weight on the Growth of Polythiophene Nanofibrils and Mixes of Short and

Long Nanofibrils to Enhance the Hole Transport. *ACS Appl Mater Interfaces* **2015,** *7* (50), 27694-702.

60. Kleinhenz, N.; Rosu, C.; Chatterjee, S.; Chang, M.; Nayani, K.; Xue, Z.; Kim, E.; Middlebrooks, J.; Russo, P.; Park, J.; Srinivasarao, M.; Reichmanis, E., Liquid Crystalline Poly(3-Hexylthiophene) Solutions Revisited: Role of Time-Dependent Self-Assembly. *Chemistry of Materials* **2015,** *27* (7), 2687-2694.

61. Chang, M. C., D.; Yu, B.; Reichmanis, E. , Solvent Based Hydrogen Bonding: Impact on Poly(3-Hexylthiophene) Nanoscale Morphology and Charge Transport Characteristics. *ACS Nano* **2013,** *7* (6), 5402-5413.

62. Zhao, K.; Xue, L.; Liu, J.; Gao, X.; Wu, S.; Han, Y.; Geng, Y., A New Method to Improve Poly(3-Hexyl Thiophene) (P3ht) Crystalline Behavior: Decreasing Chains Entanglement to Promote Order-Disorder Transformation in Solution. *Langmuir* **2010,** *26* (1), 471-7.

63. Zhao, K.; Khan, H.; Li, R.; Su, Y.; Amassian, A., Entanglement of Conjugated Polymer Chains Influences Molecular Self-Assembly and Carrier Transport. *Advanced Functional Materials* **2013,** *23* (48), 6024-6035.

64. Choi, D.; Chang, M.; Reichmanis, E., Controlled Assembly of Poly(3-Hexylthiophene): Managing the Disorder to Order Transition on the Nano- through Meso-Scales. *Advanced Functional Materials* **2015,** *25* (6), 920-927.

65. Xue, X.; Chandler, G.; Zhang, X.; Kline, R. J.; Fei, Z.; Heeney, M.; Diemer, P. J.; Jurchescu, O. D.; O'Connor, B. T., Oriented Liquid Crystalline Polymer Semiconductor Films with Large Ordered Domains. *ACS Appl Mater Interfaces* **2015,** *7* (48), 26726-26734.

66. Chang, M.; Lee, J.; Kleinhenz, N.; Fu, B.; Reichmanis, E., Photoinduced Anisotropic Supramolecular Assembly and Enhanced Charge Transport of Poly(3-Hexylthiophene) Thin Films. *Advanced Functional Materials* **2014,** *24* (28), 4457-4465.

67. Chang, M.; Lee, J.; Chu, P. H.; Choi, D.; Park, B.; Reichmanis, E., Anisotropic Assembly of Conjugated Polymer Nanocrystallites for Enhanced Charge Transport. *ACS Appl Mater Interfaces* **2014,** *6* (23), 21541-9.

68. Chang, M.; Choi, D.; Wang, G.; Kleinhenz, N.; Persson, N.; Park, B.; Reichmanis, E., Photoinduced Anisotropic Assembly of Conjugated Polymers in Insulating Polymer Blends. *ACS Appl Mater Interfaces* **2015,** *7* (25), 14095-103.

69. Kleinhenz, N.; Persson, N.; Xue, Z.; Chu, P. H.; Wang, G.; Yuan, Z.; McBride, M.; Choi, D.; Grover, M.; Reichmanis, E., Ordering of Poly(3-Hexylthiophene) in Solutions and Films: Effects of Fiber Length and Grain Boundaries on Anisotropy and Mobility. *Chemistry of Materials* **2016,** *28* (11), 3905-3913.

70. Persson, N. E.; Rafshoon, J.; Naghshpour, K.; Fast, T.; Chu, P. H.; McBride, M.; Risteen, B.; Grover, M.; Reichmanis, E., High-Throughput Image Analysis of Fibrillar Materials: A Case Study on Polymer Nanofiber Packing, Alignment, and Defects in Organic Field Effect Transistors. *ACS Appl Mater Interfaces* **2017,** *9* (41), 36090-36102.

71. Clark, J.; Chang, J.; Spano, F.; Friend, R.; Silva, C., Determining Exciton Bandwidth and Film Microstructure in Polythiophene Films Using Linear Absorption Spectroscopy. *Applied Physics Letters* **2009,** *94* (16), 163306.

72. Clark, J.; Silva, C.; Friend, R. H.; Spano, F. C., Role of Intermolecular Coupling in the Photophysics of Disordered Organic Semiconductors: Aggregate Emission in Regioregular Polythiophene. *Phys Rev Lett* **2007,** *98* (20), 206406.

73. Panzer, F.; Sommer, M.; Bässler, H.; Thelakkat, M.; Köhler, A., Spectroscopic Signature of Two Distinct H-Aggregate Species in Poly(3-Hexylthiophene). *Macromolecules* **2015,** *48* (5), 1543-1553.

74. Pingel, P.; Zen, A.; Abellón, R. D.; Grozema, F. C.; Siebbeles, L. D. A.; Neher, D., Temperature-Resolved Local and Macroscopic Charge Carrier Transport in Thin P3ht Layers. *Advanced Functional Materials* **2010,** *20* (14), 2286-2295.

75. Turner, S. T.; Pingel, P.; Steyrleuthner, R.; Crossland, E. J. W.; Ludwigs, S.; Neher, D., Quantitative Analysis of Bulk Heterojunction Films Using Linear Absorption Spectroscopy and Solar Cell Performance. *Advanced Functional Materials* **2011,** *21* (24), 4640-4652.

76. Spano, F. C., Modeling Disorder in Polymer Aggregates: The Optical Spectroscopy of Regioregular Poly(3-Hexylthiophene) Thin Films. *J Chem Phys* **2005,** *122* (23), 234701.

77. Spano, F. C., The Spectral Signatures of Frenkel Polarons in H- and J-Aggregates. *Accounts of Chemical Research* **2010,** *43* (3), 429-439.

78. Spano, F. C.; Silva, C., H- and J-Aggregate Behavior in Polymeric Semiconductors. *Annu Rev Phys Chem* **2014,** *65*, 477-500.

79. Rivnay, J.; Mannsfeld, S. C.; Miller, C. E.; Salleo, A.; Toney, M. F., Quantitative Determination of Organic Semiconductor Microstructure from the Molecular to Device Scale. *Chem Rev* **2012,** *112* (10), 5488-5519.

80. Salleo, A., Charge Transport in Polymeric Transistors. *Materials Today* **2007,** *10* (3), 38-45.

81. Coropceanu, V. C., J.; Silva Filho, D.; Olivier, Y.; Silbey, R. Bredas, J. , Charge Transport in Organic Semiconductors. *Chem. Rev.* **2007,** *107* (4), 926-952.

82. Persson, N. E.; Chu, P. H.; McBride, M.; Grover, M.; Reichmanis, E., Nucleation, Growth, and Alignment of Poly(3-Hexylthiophene) Nanofibers for High-Performance Ofets. *Acc Chem Res* **2017,** *50* (4), 932-942.

83. Vakhshouri, K.; Smith, B. H.; Chan, E. P.; Wang, C.; Salleo, A.; Wang, C.; Hexemer, A.; Gomez, E. D., Signatures of Intracrystallite and Intercrystallite Limitations of Charge Transport in Polythiophenes. *Macromolecules* **2016,** *49* (19), 7359-7369.

84. Kline, R.; McGehee, M.; Kadnikova, E.; Liu, J.; Frechet, J., Controlling the Field-Effect Mobility of Regioregular Polythiophene by Changing the Molecular Weight. *Advanced Materials* **2003,** *15* (18), 1519-1522.

85. Zen, A.; Saphiannikova, M.; Neher, D.; Grenzer, J.; Grigorian, S.; Pietsch, U.; Asawapirom, U.; Janietz, S.; Scherf, U.; Lieberwirth, I.; Wegner, G., Effect of Molecular Weight on the Structure and Crystallinity of Poly(3-Hexylthiophene). *Macromolecules* **2006,** *39* (6), 2162-2171.

86. Koch, F. P. V.; Rivnay, J.; Foster, S.; Müller, C.; Downing, J. M.; Buchaca-Domingo, E.; Westacott, P.; Yu, L.; Yuan, M.; Baklar, M.; Fei, Z.; Luscombe, C.; McLachlan, M. A.; Heeney, M.; Rumbles, G.; Silva, C.; Salleo, A.; Nelson, J.; Smith, P.; Stingelin, N., The Impact of Molecular Weight on Microstructure and Charge Transport in Semicrystalline Polymer Semiconductors–Poly(3-Hexylthiophene), a Model Study. *Progress in Polymer Science* **2013,** *38* (12), 1978-1989.

87. Wu, D.; Kaplan, M.; Ro, H. W.; Engmann, S.; Fischer, D. A.; DeLongchamp, D. M.; Richter, L. J.; Gann, E.; Thomsen, L.; McNeill, C. R.; Zhang, X., Blade Coating Aligned, High-Performance, Semiconducting-Polymer Transistors. *Chemistry of Materials* **2018,** *30* (6), 1924-1936.

88. Xu, W.; Li, L.; Tang, H.; Li, H.; Zhao, X.; Yang, X., Solvent-Induced Crystallization of Poly(3-Dodecylthiophene): Morphology and Kinetics. *J Phys Chem B* **2011,** *115* (20), 6412-6420.

89. Okamoto, K.; Luscombe, C. K., Controlled Polymerizations for the Synthesis of Semiconducting Conjugated Polymers. *Polymer Chemistry* **2011,** *2* (11), 2424-2434.

90. Ma, W.; Kim, J. Y.; Lee, K.; Heeger, A. J., Effect of the Molecular Weight of Poly(3-Hexylthiophene) on the Morphology and Performance of Polymer Bulk Heterojunction Solar Cells. *Macromolecular Rapid Communications* **2007,** *28* (17), 1776-1780.

91. Koppe, M.; Brabec, C. J.; Heiml, S.; Schausberger, A.; Duffy, W.; Heeney, M.; McCulloch, I., Influence of Molecular Weight Distribution on the Gelation of P3ht and Its Impact on the Photovoltaic Performance. *Macromolecules* **2009,** *42* (13), 4661-4666.

92. Himmelberger, S.; Vandewal, K.; Fei, Z.; Heeney, M.; Salleo, A., Role of Molecular Weight Distribution on Charge Transport in Semiconducting Polymers. *Macromolecules* **2014,** *47* (20), 7151-7157.

93. Sirringhaus, H.; Tessler, N.; Friend, R. H., Integrated Optoelectronic Devices Based on Conjugated Polymers. *Science* **1998,** *280*, 1741-1744.

94. Wu, P.-T.; Bull, T.; Kim, F. S.; Luscombe, C. K.; Jenekhe, S. A., Organometallic Donor-Acceptor Conjugated Polymer Semiconductors: Tunable Optical, Electrochemical, Charge Transport, and Photovoltaic Properties. *Macromolecules* **209,** *42*, 671-681.

95. Liu, C.-Y.; Chen, S.-A., Charge Mobility and Charge Traps in Conjugated Polymers. *Macromolecular Rapid Communications* **2007,** *28* (17), 1743-1760.

96. Lu, G.; Blakesley, J.; Himmelberger, S.; Pingel, P.; Frisch, J.; Lieberwirth, I.; Salzmann, I.; Oehzelt, M.; Di Pietro, R.; Salleo, A.; Koch, N.; Neher, D., Moderate Doping Leads to High Performance of Semiconductor/Insulator Polymer Blend Transistors. *Nat Commun* **2013,** *4*, 1588.

97. Kozlov, O. V.; Zapunidi, S. A., Reversible Oxygen Doping of Conjugated Polymer and Its Dedoping Studied by Mott–Schottky Analysis. *Synthetic Metals* **2013,** *169*, 48-54.

98. Mattis, B. A.; Chang, P. C.; Subramanian, V., Performance Recovery and Optimization of Poly(3-Hexylthiophene) Transistors by Thermal Cycling. *Synthetic Metals* **2006,** *156* (18-20), 1241-1248.

99. Liao, H.-H.; Yang, C.-M.; Liu, C.-C.; Horng, S.-F.; Meng, H.-F.; Shy, J.-T., Dynamics and Reversibility of Oxygen Doping and De-Doping for Conjugated Polymer. *Journal of Applied Physics* **2008,** *103* (10), 104506.

100. Jacobs, I. E.; Moule, A. J., Controlling Molecular Doping in Organic Semiconductors. *Adv Mater* **2017,** *29* (42), 1703063.

101. Giraudet, L.; Simonetti, O., Threshold Voltage and Turn-on Voltage in Organic Transistors: Sensitivity to Contact Parasitics. *Organic Electronics* **2011,** *12* (1), 219-225.

102. Mathijssen, S. G. J.; Cölle, M.; Gomes, H.; Smits, E. C. P.; de Boer, B.; McCulloch, I.; Bobbert, P. A.; de Leeuw, D. M., Dynamics of Threshold Voltage Shifts in Organic and Amorphous Silicon Field-Effect Transistors. *Advanced Materials* **2007,** *19* (19), 2785-2789.

103. Paquin, F.; Yamagata, H.; Hestand, N. J.; Sakowicz, M.; Bérubé, N.; Côté, M.; Reynolds, L. X.; Haque, S. A.; Stingelin, N.; Spano, F. C.; Silva, C., Two-Dimensional Spatial Coherence of Excitons in Semicrystalline Polymeric Semiconductors: Effect of Molecular Weight. *Physical Review B* **2013,** *88* (15), 155202.

104. Brown, P. J.; Thomas, D. S.; Köhler, A.; Wilson, J. S.; Kim, J.-S.; Ramsdale, C. M.; Sirringhaus, H.; Friend, R. H., Effect of Interchain Interactions on the Absorption and Emission of Poly(3-Hexylthiophene). *Physical Review B* **2003,** *67* (6), 064203.

105. Persson, N. Analysis of Fibrillar Structures for the Engineering of Polymeric Transistors. Georgia Institute of Technology, 2017.

106. Jordens, S.; Isa, L.; Usov, I.; Mezzenga, R., Non-Equilibrium Nature of Two-Dimensional Isotropic and Nematic Coexistence in Amyloid Fibrils at Liquid Interfaces. *Nat Commun* **2013,** *4*, 1917.

107. Murphy, J. N.; Harris, K. D.; Buriak, J. M., Automated Defect and Correlation Length Analysis of Block Copolymer Thin Film Nanopatterns. *PLoS One* **2015,** *10* (7), e0133088.

108. Persson, N.; McBride, M.; Grover, M.; Reichmanis, E., Automated Analysis of Orientational Order in Images of Fibrillar Materials. *Chemistry of Materials* **2016,** *29* (1), 3-14.

109. Wang, G.; Huang, W.; Eastham, N. D.; Fabiano, S.; Manley, E. F.; Zengg, L.; Wang, B.; Zhang, X.; Chend, Z.; Lib, R.; Chang, R. P. H.; Chen, L. X.; Bedzyk, M. J.; Melkonyan, F. S.; Facchetti, A.; Marks, T. J., Aggregation Control in Natural Brush-Printed Conjugated Polymer Films and Implications for Enhancing Charge Transport. *Proceedings of the National Academy of Sciences* **2017,** *114* (47), E10066–E10073.

110. Flory, P. J., Thermodynamics of Polymer Solutions. *Journal of Chemical Physics* **1942,** *10*, 51-61.

111. Flory, P. J., *Principles of Polymer Chemistry*. Cornell University, Ithaca, NY, 1953.

112. Dixon, A. G.; Visvanathan, R.; Clark, N. A.; Stingelin, N.; Kopidakis, N.; Shaheen, S. E., Molecular Weight Dependence of Carrier Mobility and Recombination Rate in Neat P3ht Films. *Journal of Polymer Science Part B: Polymer Physics* **2018,** *56* (1), 31-35.

113. Chang, J.; Clark, J.; Zhao, N.; Sirringhaus, H.; Breiby, D.; Andreasen, J.; Nielsen, M.; Giles, M.; Heeney, M.; McCulloch, I., Molecular-Weight Dependence of Interchain Polaron Delocalization and Exciton Bandwidth in High-Mobility Conjugated Polymers. *Physical Review B* **2006,** *74* (11), 115318-115329.

114. Wang, S.; Fabiano, S.; Himmelberger, S.; Puzinas, S.; Crispin, X.; Salleo, A.; Berggren, M., Experimental Evidence That Short-Range Intermolecular Aggregation Is Sufficient for Efficient Charge Transport in Conjugated Polymers. *Proc Natl Acad Sci U S A* **2015,** *112* (34), 10599-10604.

115. Samitsu, S.; Shimomura, T.; Heike, S.; Hashizume, T.; Ito, K., Effective Production of Poly(3-Alkylthiophene) Nanofibers by Means of Whisker Method Using Anisole Solvent: Structural, Optical, and Electrical Properties. *Macromolecules* **2008,** *41*, 8000-8010.

116. Samitsu, S.; Shimomura, T.; Ito, K., Nanofiber Preparation by Whisker Method Using Solvent-Soluble Conducting Polymers. *Thin Solid Films* **2008,** *516* (9), 2478-2486.

117. Diao, Y.; Shaw, L.; Bao, Z.; Mannsfeld, S. C. B., Morphology Control Strategies for Solution-Processed Organic Semiconductor Thin Films. *Energy Environ. Sci.* **2014,** *7* (7), 2145-2159.

118. Lee, M. J.; Gupta, D.; Zhao, N.; Heeney, M.; McCulloch, I.; Sirringhaus, H., Anisotropy of Charge Transport in a Uniaxially Aligned and Chain-Extended, High-Mobility, Conjugated Polymer Semiconductor. *Advanced Functional Materials* **2011,** *21* (5), 932-940.

119. Dörling, B.; Vohra, V.; Dao, T. T.; Garriga, M.; Murata, H.; Campoy-Quiles, M., Uniaxial Macroscopic Alignment of Conjugated Polymer Systems by Directional Crystallization During Blade Coating. *J. Mater. Chem. C* **2014,** *2* (17), 3303-3310.

120. Shin, J.; Hong, T. R.; Lee, T. W.; Kim, A.; Kim, Y. H.; Cho, M. J.; Choi, D. H., Template-Guided Solution-Shearing Method for Enhanced Charge Carrier Mobility in Diketopyrrolopyrrole-Based Polymer Field-Effect Transistors. *Adv Mater* **2014,** *26* (34), 6031-5.

121. Diao, Y.; Tee, B. C.; Giri, G.; Xu, J.; Kim, D. H.; Becerril, H. A.; Stoltenberg, R. M.; Lee, T. H.; Xue, G.; Mannsfeld, S. C.; Bao, Z., Solution Coating of Large-Area Organic Semiconductor Thin Films with Aligned Single-Crystalline Domains. *Nat Mater* **2013,** *12* (7), 665-71.

122. Zhang, L.; Zhou, W.; Shi, J.; Hu, T.; Hu, X.; Zhang, Y.; Chen, Y., Poly(3-Butylthiophene) Nanowires Inducing Crystallization of Poly(3-Hexylthiophene) for Enhanced Photovoltaic Performance. *Journal of Materials Chemistry C* **2015,** *3* (4), 809-819.

123. Kim, N.-K.; Jang, S.-Y.; Pace, G.; Caironi, M.; Park, W.-T.; Khim, D.; Kim, J.; Kim, D.-Y.; Noh, Y.-Y., High-Performance Organic Field-Effect Transistors with Directionally Aligned Conjugated Polymer Film Deposited from Pre-Aggregated Solution. *Chemistry of Materials* **2015,** *27* (24), 8345-8353.

124. Nahid, M. M.; Welford, A.; Gann, E.; Thomsen, L.; Sharma, K. P.; McNeill, C. R., Nature and Extent of Solution Aggregation Determines the Performance of P(Ndi2od-T2) Thin-Film Transistors. *Advanced Electronic Materials* **2018,** *4* (4), 1700559.

125. Heuvel, R.; Colberts, F. J. M.; Li, J.; Wienk, M. M.; Janssen, R. A. J., The Effect of Side-Chain Substitution on the Aggregation and Photovoltaic Performance of Diketopyrrolopyrrole-Alt-Dicarboxylic Ester Bithiophene Polymers. *Journal of Materials Chemistry A* **2018,** *6* (42), 20904-20915.

126. McBride, M.; Persson, N.; Keane, D.; Bacardi, G.; Reichmanis, E.; Grover, M. A., A Polymer Blend Approach for Creation of Effective Conjugated Polymer Charge Transport Pathways. *ACS Appl Mater Interfaces* **2018,** *10* (42), 36464-36474.

127. Cheng, S. Z. D.; Wunderlich, B., Modification of the Avrami Treatment of Crystallization to Account for Nuclues and Interface. *Macromolecules* **1988,** *21*, 3327-3328.

128. Datta, J.; Nandi, A. K., Cocrystallization Mechanism of Vinylidene Fluoride-Tetrafluoroethylene Copolymers with Different Copolymer Composition. *Macrom. Chem. Phys.* **1998,** *199*, 2583-2599.

129. Spano, F. C., Absorption in Regio-Regular Poly(3-Hexyl)Thiophene Thin Films: Fermi Resonances, Interband Coupling and Disorder. *Chemical Physics* **2006,** *325* (1), 22-35.

130. Minemawari, H.; Yamada, T.; Matsui, H.; Tsutsumi, J.; Haas, S.; Chiba, R.; Kumai, R.; Hasegawa, T., Inkjet Printing of Single-Crystal Films. *Nature* **2011,** *475* (7356), 364-7.

131. Lim, K. C.; Heeger, A. J., Spectroscopic and Light Scattering Studies of the Conformational (Rod-to-Coil) Transition of Poly(Diacetylene) in Solution. *The Journal of Chemical Physics* **1985,** *82* (1), 522-530.

132. Kalidindi, S. R.; De Graef, M., Materials Data Science: Current Status and Future Outlook. *Annual Review of Materials Research* **2015,** *45* (1), 171-193.

133. Citrine Informatics. http://www.citrination.com.

134. Calphad (Computer Coupling of Phase Diagrams and Thermochemistry). http://www.calphad.org.

135. The Materials Project. http://www.materialsproject.org.

136. Open Quantum Materials Database. http://oqmd.org.

137. Nist (National Institute of Standards and Technology) Data Gateway. http://srdata.nist.gov/gateway/gateway?dblist=1.

138. Casciato, M. J.; Vastola, J. T.; Lu, J. C.; Hess, D. W.; Grover, M. A., Initial Experimental Design Methodology Incorporating Expert Conjecture, Prior Data, and Engineering Models for Deposition of Iridium Nanoparticles in Supercritical Carbon Dioxide. *Industrial & Engineering Chemistry Research* **2013,** *52* (28), 9645-9653.

139. Kim, E.; Huang, K.; Saunders, A.; McCallum, A.; Ceder, G.; Olivetti, E., Materials Synthesis Insights from Scientific Literature Via Text Extraction and Machine Learning. *Chemistry of Materials* **2017,** *29* (21), 9436-9444.

140. Agrawal, A.; Deshpande, P.; Cecen, A.; Basavarsu, G.; Choudhary, A.; Kalidindi, S., Exploration of Data Science Techniques to Predict Fatigue Strength of Steel from Composition and Processing Parameters. *Integrating Materials and Manufacturing Innovation* **2014,** *3* (8), 1-19.

141. Matnavi Nims Materials Database. http://mits.nims.go.jp/index_en.html.

142. Ren, F.; Ward, L.; Williams, T.; Laws, K. J.; Wolverton, C.; Hattrick-Simpers, J.; Mehta, A., Accelerated Discovery of Metallic Glasses through Iteration of Machine Learning and High-Throughput Experiments. *Science Advances* **2018,** *4* (4), 1-11.

143. AbuOmar, O.; Nouranian, S.; King, R.; Bouvard, J. L.; Toghiani, H.; Lacy, T. E.; Pittman, C. U., Data Mining and Knowledge Discovery in Materials Science and Engineering: A Polymer Nanocomposites Case Study. *Advanced Engineering Informatics* **2013,** *27* (4), 615-624.

144. Zhang, S. L.; Zhang, Z. X.; Xin, Z. X.; Pal, K.; Kim, J. K., Prediction of Mechanical Properties of Polypropylene/Waste Ground Rubber Tire Powder Treated by Bitumen Composites Via Uniform Design and Artificial Neural Networks. *Materials & Design* **2010,** *31* (4), 1900-1905.

145. Ling, J.; Hutchinson, M.; Antono, E.; Paradiso, S.; Meredig, B., High-Dimensional Materials and Process Optimization Using Data-Driven Experimental Design with Well-Calibrated Uncertainty Estimates. *Integrating Materials and Manufacturing Innovation* **2017,** *6* (3), 207-217.

146. Park, J.; Howe, J. D.; Sholl, D. S., How Reproducible Are Isotherm Measurements in Metal–Organic Frameworks? *Chemistry of Materials* **2017,** *29* (24), 10487-10495.

147. Persson, N.; McBride, M.; Grover, M.; Reichmanis, E., Silicon Valley Meets the Ivory Tower: Searchable Data Repositories for Experimental Nanomaterials Research. *Current Opinion in Solid State and Materials Science* **2016,** *20* (6), 338-343.

148. Box, G. E.; Wilson, K. B., On the Experimental Attainment of Optimum Conditions. *Journal of the Royal Statistical Society* **1951,** *13* (1), 1-45.

149. Montgomery, D. C., *Design and Analysis of Experiments*. seventh edition ed.; Wiley: New York, 2009.

150. Kim, S.; Kim, H.; Lu, J.-C.; Casciato, M. J.; Grover, M. A.; Hess, D. W.; Lu, R. W.; Wang, X., Layers of Experiments with Adaptive Combined Design. *Naval Research Logistics (NRL)* **2015,** *62* (2), 127-142.

151. Dimitrakopoulos, C. D.; Malenfant, P. R. L., Organic Thin Film Transistors for Large Area Electronics. *Advanced Materials* **2002,** *14* (2), 99-117.

152. Shubhra, Q. T. H.; Alam, A.; Quaiyyum, M. A., Mechanical Properties of Polypropylene Composites. *Journal of Thermoplastic Composite Materials* **2011,** *26* (3), 362-391.

153. Ahmed, S.; Jones, F. R., A Review of Particulate Reinforcement Theories for Polymer Composites. *Journal of Materials Science* **1990,** *25*, 49933-4942.

154. Paul, D. R.; Robeson, L. M., Polymer Nanotechnology: Nanocomposites. *Polymer* **2008,** *49* (15), 3187-3204.

155. Samuels, R. J., Polymer Structure: The Key to Process-Property Control. *Polymer Engineering and Science* **1985,** *25* (14), 864-874.

156. Premalal, H.; Ismail, H.; Baharin, A., Comparison of the Mechanical Properties of Rice Husk Powder Filled Polypropylene Composites with Talc Filled Polypropylene Composites. *Polymer Testing* **2002,** *21* (7), 833-839.

157. Pukanszky, B.; Belina, K.; Rockenbauer, A.; Maurer, R. H. J., Effect of Nucleation, Filler Anisotropy and Orientation on the Properties of Pp Composities. *Composites* **1993,** *3*, 205-214.

158. Arias, A. C.; MacKenziew, J. D.; McCulloch, I.; Rivnay, J.; Salleo, A., Materials and Applications for Large Area Electronics: Solution-Based

Approaches. *Chemical Reviews* **2010,** *110* (1), 3-24.

159. Bronstein, H. A.; Luscombe, C. K., Externally Initiated Regioregular P3ht with Controlled Molecular Weight and Narrow Polydispersity. *Journal of American Chemical Society* **2009,** *131*, 12894-12895.

160. Choi, D.; Chu, P.-H.; McBride, M.; Reichmanis, E., Best Practices for Reporting Organic Field Effect Transistor Device Performance. *Chemistry of Materials* **2015,** *27* (12), 4167-4168.

161. Raccuglia, P.; Elbert, K. C.; Adler, P. D.; Falk, C.; Wenny, M. B.; Mollo, A.; Zeller, M.; Friedler, S. A.; Schrier, J.; Norquist, A. J., Machine-Learning-Assisted Materials Discovery Using Failed Experiments. *Nature* **2016,** *533* (7601), 73-6.

162. Roesing, M.; Howell, J.; Boucher, D., Solubility Characteristics of Poly(3-Hexylthiophene). *Journal of Polymer Science Part B: Polymer Physics* **2017**.

163. Verilhac, J.; LeBlevennec, G.; Djurado, D.; Rieutord, F.; Chouiki, M.; Travers, J.; Pron, A., Effect of Macromolecular Parameters and Processing Conditions on Supramolecular Organisation, Morphology and Electrical Transport Properties in Thin Layers of Regioregular Poly(3-Hexylthiophene). *Synthetic Metals* **2006,** *156* (11-13), 815-823.

164. Joshi, S.; Grigorian, S.; Pietsch, U.; Pingel, P.; Zen, A.; Neher, D.; Scherf, U., Thickness Dependence of the Crystalline Structure and Hole Mobility in Thin Films of Low Molecular Weight Poly(3-Hexylthiophene). *Macromolecules* **2008,** *41*, 6800-8.

165. Na, J. Y.; Kang, B.; Sin, D. H.; Cho, K.; Park, Y. D., Understanding Solidification of Polythiophene Thin Films During Spin-Coating: Effects of Spin-Coating Time and Processing Additives. *Sci Rep* **2015,** *5*, 13288.

166. Bermner, T.; Rudin, A., Melt Flow Index Values and Molecular Weight Distributions of Commercial Thermoplastics. *Journal of Applied Polymer Science* **1990,** *41*, 1617-1627.

167. Gafur, M. A.; Nasrin, R.; Mina, M. F.; Bhuiyan, M. A. H.; Tamba, Y.; Asano, T., Structures and Properties of the Compression-Molded Istactic-Polypropylene/Talc Composites: Effect of Cooling and Rolling. *Polymer Degradation and Stability* **2010,** *95* (9), 1818-1825.

168. Verpoort, P. C.; MacDonald, P.; Conduit, G. J., Materials Data Validation and Imputation with an Artificial Neural Network. *Computational Materials Science* **2018,** *147*, 176-185.

169. Nelson, P. R. C. Treatment of Missing Measurements in Pca and Pls Models. McMaster University, Hamilton, Ontario, Canada, 2002.

170. Nelson, P. R. C.; Taylor, P. A.; MacGregor, J. F., Missing Data Methods in Pca and Pls: Score Calculations with Incomplete Observations. *Chemometrics and Intelligent Laboratory Systems* **1996,** *35*, 45-65.

171. Folch-Fortuny, A.; Arteaga, F.; Ferrer, A., Pca Model Building with Missing Data: New Proposals and a Comparative Study. *Chemometrics and Intelligent Laboratory Systems* **2015,** *146*, 77-88.

172. Berman, H. M.; Westbrook, J.; Feng, Z.; Gilliland, G.; Bhat, T. N.; Weissig, H.; Shindyalov, I. N.; Bourne., P. E. The Protein Data Bank. https://www.rcsb.org/.

173. Pande, V. S.; Beauchamp, K.; Bowman, G. R., Everything You Wanted to Know About Markov State Models but Were Afraid to Ask. *Methods* **2010,** *52* (1), 99-105.